UNIVERSITY OF OKLAHOMA

GRADUATE COLLEGE

LABORATORY CHARACTERIZATION OF RESERVOIR STIMULATION AND HEAT EXTRACTION WITH APPLICATION TO EGS

A DISSERTATION

SUBMITTED TO THE GRADUATE FACULTY

in partial fulfillment of the requirements for the

Degree of

DOCTOR OF PHILOSOPHY

By

LIANBO HU
Norman, Oklahoma
2019

Downloaded from SHAREOK. Persistent Handle URL: https://hdl.handle.net/11244/322839

LABORATORY CHARACTERIZATION OF RESERVOIR STIMULATION AND HEAT EXTRACTION WITH APPLICATION TO EGS

A DISSERTATION APPROVED FOR THE
MEWBOURNE SCHOOL OF PETROLEUM AND GEOLOGICAL ENGINEERING

BY THE COMMITTEE CONSISTING OF

Dr. Ahmad Ghassemi, Chair

Dr. Matthew J. Pranter

Dr. Jean-Claude Roegiers

Dr. Xingru Wu

Dr. Mashhad Fahes

© Copyright by LIANBO HU 2019
All Rights Reserved.

In dedication to my wife Chunling Li and our daughter Yvonne Li Hu and my family.

Acknowledgements

I would like to express my sincere gratitude to my advisor, Dr. Ahmad Ghassemi, for this advice, guidance, trust and nonstop support throughout my PhD study at the University of Oklahoma. Dr. Ghassemi broaden my horizon in geomechanics by providing me the opportunity to work on this challenging task about lab-scale simulation of enhanced geothermal system; discussing with me on the test design and interpreting the result. Without his trust and support, the completion of this dissertation would never happen.

I would like to thank my committee members: Dr. Matthew J. Pranter, Dr. Jean-Claude Roegiers, Dr. Xingru Wu and Dr. Mashhad Fahes at the University of Oklahoma for their guiding my work. For example, I always learned a lot from the discussion with Dr. Wu about tracer analysis. I would also like to thank Dr. John Pritchett, Dr. Sabodh Garg, Dr. Tsuneo Ishido, and Mr. G. Michael Shook for their advice, comments on the test design and result interpretation.

I greatly appreciate the precious help and encouragement from our group members, Dr. Yawei Li, Dr. Kai Huang, Dr. Qian Gao, Dr. Qinglu Cheng, Dr. Varahanaresh Sesetty, Dr. Dharmendra Kumar, Dr. Xuejun Zhou and Lei Han, Weiqi Yu, Jiman Liu, Zhe Ye, Jianrong Lu, Rohit Bahshi, Alex Vachaparampil, Kyle Bolyard, Bey Westcott, Maulin Gogri and more. They make my Ph.D. study a great experience. Special thanks should be given to out lab manger, Steve Dwyer, who helped me a lot on my work in the lab.

Finally, I would like to thank my wife Chunling Li, my parents, Qinghua Hu and Xuanzhen He, my parents-in-law Shanghui Li, Chunrong Xu and my brothers, for their unconditional endless love and support. Though not being able to stay with them for most of the past years,

their support is always the most important driving forces for my study and life. I appreciate the happiness my daughter Yvonne bringing to my life.

Table of Contents

Acknowledgements v

Table of Contents vii

List of Tables x

List of Figures xi

Abstract xvii

1. Introduction 1

    1.1 Literature Review 1

    1.2 Motivation and Objectives 11

    1.3 Dissertation Outlines 12

2. Lab-Scale EGS Test System 14

    2.1 Overview of the Test System 14

    2.2 Polyaxial Loading Frame 15

    2.3 Sample Preparation 17

    2.4 Acoustic Emission and Self-potential Survey 20

    2.5 Circulation System and Heating System 21

    2.6 Tracer test system 24

    2.7 Sample Characterization 25

    2.8 Test Procedure 29

3. Characterization of Laboratory-Scale Hydraulic Fracturing 31

    3.1 Controlled Fracture Propagation 31

    3.2 Breakdown, Acoustic emissions 32

        3.2.1 Stimulation under Low In-situ Stress Condition 32

3.2.2 Stimulation under Higher In-situ Stress Condition 34
3.3 Injectivity of the Rock Matrix and the Induced Fracture 43
3.4 Hydraulic Fracture Geometry and Its Surface Characterization 45
3.5 Thin Section and SEM Observation of the Fracture 49
3.6 Summary and Conclusions 50
4. Self-Potential Response in Lab-scale EGS Simulation 52
4.1 Electrokinetic Phenomena 52
4.2 Influence of Saturation Condition and Different Boundary Conditions 53
4.3 Influence of Temperature on SP Response 59
4.4 Influence of Fluid Concentration on SP Response 63
4.5 Results from a Test on a Rock with Zero-porosity 65
4.6 Summary and Conclusions 66
5. Heat Production from Lab-scale EGS 68
5.1 Case I: Heat Extraction form a Hydraulic Fracture Intersecting a Wellbore and Constrained in the Block 68
5.2 Case II: Heat Extraction form a Hydraulic Fracture Intersecting a Wellbore and the Block Boundary 74
5.3 Case III: Heat Extraction from a Hydraulic Fracture Connected with Two Wells 77
5.4 Case IV: Heart Extraction from a Hydraulic Fracture in Gabbro Intersecting Four Wells 80
5.5 Comparison of the test data with Gringarten solution 83
5.6 Summary and Conclusions 87
6. Lab-scale Tracer Test in Enhanced Geothermal System 92

6.1 Calculation of the Tracer Concentration and Methodology Verification 92
6.2 Velocity of the Tracer Fluid in the Fracture.....96
6.3 Determination of Swept Volume with the Method of Moments.....96
6.4 Flow Geometry Revealed by the Tracer Response 98
6.5 Test results under different fracture geometries and rocks materials 100
6.5.1 Case I: multi-production wells intersected by the induced fracture.....100
6.5.2 Case II: Only one production well intersected by the induced fracture.....104
6.5.3 Case III: Test Result with Raven Noir Gabbro 107
6.6 Conclusions and Discussion.....110
7. Slippage of a Natural Fracture Resulting from an Approaching Hydraulic Fracture113
7.1 Test setup and Test Procedures 113
7.2 Calculation of the slippage on the natural fracture 116
7.3 Test Results 118
7.3.1 Case I: Test Result with PMMA 118
7.3.2 Test result with Shale Core: Thistle 121
7.3.3 Test result with Shale Core: Janis 125
7.3.4 Test result with Sierra White granite 129
7.4 Summery and Conclusion 133
8. Summary and Conclusion 135
Biography.....141

List of Tables

Table 2.1. Mechanical properties of the tested rocks.....26

Table 2.2. Mineralogy of the tested rocks.....27

Table 2.3. Lab-scale EGS simulation test procedures. 30

Table 3.1. Surface parameters for Sierra White granite and Raven Noir gabbro 48

Table 4.1. Phenomena involved in self-potential method.....52

Table 5.1. The properties for water and granite and the test conditions 86

Table 5.2. Important data for all the test cases.....87

Table 6.1. The results of the feasibility test of the proposed method to measure the conductivity of small volumes of the produced fluid 94

Table 6.2. Fluid velocity obtain fracture tracer tests.....111

Table 7.1 Basic rock properties and loading condition of the tested shale sample.....118

List of Figures

Figure 2-1. Partially (left) and fully (right) assembled frame 16

Figure 2-2. A typical flat-jack calibration result with flatjack thickness maintaining at 25.4 mm 17

Figure 2-3. Top view (left) and longitudinal sectional view (right) of the wells and sensors 19

Figure 2-4. An example picture of a slab cutting from a tested sample.....20

Figure 2-5. The schematic diagram of the circulation test setup 22

Figure 2-6. An example of temperature history in wells during heating process 23

Figure 2-7. The strain-stress curve for Sierra White granite and Raven Noir gabbro with confining pressure of 34.5 MPa. 26

Figure 2-8. The density and viscosity of water under different temperature with standard atmosphere pressure. 28

Figure 2-9. The viscosity, conductivity and density of NaCl solution with different concentration. 29

Figure 3-1. The reconstructed induced fracture geometry from a Raven Noir gabbro block. The fracture was mainly induced during reservoir stimulation, and there is no parent fracture extension during the following tests (Hu et al., 2018b) 32

Figure 3-2. The recording data from hydraulic fracturing test with low stress level.....33

Figure 3-3. The pressure history in wells at low stress level fracturing test. Red rectangles in the right-hand figure denote locations of AE events.....34

Figure 3-4. The recording data for test with higher stress level.....36

Figure 3-5. The pressure history in injection and production wells.....37

Figure 3-6. Acoustic emission analysis during fracturing test 40
Figure 3-7. Acoustic emission analysis during SCF injection test.....41
Figure 3-8. AE cloud and the reconstructed 3D fracture geometry. 42
Figure 3-9. The distribution of location error in Z direction for events within the real fracture area 42
Figure 3-10. injectivity before (left) and after fracturing (right) 44
Figure 3-11. Fracture on slabs at the center (top) and at Well No.2 (bottom) from Sierra White granite block test. 46
Figure 3-12. Fracture surface profiles obtained from laser scanning (Sierra White granite) 47
Figure 3-13. Fracture surface profiles obtained from laser scanning (Raven Noir gabbro) 47
Figure 3-14. Thin section (left) and SEM (right) observation (Sierra White granite) 50
Figure 3-15. Thin section (left) and SEM (right) observation (Raven Noir gabbro).....50
Figure 4-1. Recorded data during hydraulic fracturing of SWG block for time interval: 0-1100s (red arrows indicate the application of backflow operation and the red ellipses highlight the abnormal SP response in Well No.3 due to fracture intersection).....55
Figure 4-2. Recorded data during hydraulic fracturing of SWG block for time interval: 1100-2000 s (red ellipses mark the abnormal SP response due to fracture intersection: Well No.2 and No.3 were intersected by the induced hydraulic fracture).....56
Figure 4-3. Injection pressure and pressure in production wells during hydraulic fracturing (the circles correspond to the selected representative points used to investigate the coupling coefficient evolution). 56

Figure 4-4. Evolution of the streaming potential coefficient for different directions during hydraulic fracturing (red arrows indicate the application of backflow operation).....58
Figure 4-5. Streaming potential signals during circulation test. 61
Figure 4-6. Injection rate and temperature history during circulation test.....63
Figure 4-7. Influence of temperature on SP with Cc1 from Well No.1. 63
Figure 4-8. Streaming potential signals for different intervals during tracer test. 65
Figure 4-9. Streaming potential signals during fracturing of a RNG block. 66
Figure 5-1. Case I results: Injection data and the recorded AE (a), production rate (b), heat extraction rate (c), the reconstructed fracture geometry (d). 70
Figure 5-2. Temperature at the wellbore bottom (left) and on the rock surfaces (right) for Case I. The coordinates refer to the center of the bottom face of the block with positive x- , y-, and z-directions pointing to the north, west, and up, respectively. The units for coordinate are in mm.....72
Figure 5-3. Case II results: injection data and the recorded AE (a), production rate (b), heat extraction rate during circulation (c), and the reconstructed fracture geometry (d). 75
Figure 5-4. Temperature at the bottom of the wells (left) and on the rock surfaces (right) (Case II).....77
Figure 5-5. Case III results: Injection data and the recorded AE(a), production rate (b) and heat extraction rate (c), and the reconstructed fracture geometry (d). 78
Figure 5-6. Temperature at the bottom of the wells (left) and on the rock surfaces (right) for Case III. 79
Figure 5-7. Case IV results: Injection information and the recorded AE(a), production rate (b) and heating extraction rate (c), and the reconstructed fracture geometry (d). 81

Figure 5-8. Temperature at the bottom of the wells (left) and on the rock surfaces (right) for Case IV. 83
Figure 5-9. The injection rate, injection temperature, production temperature and the temperature and the rock boundaries. 85
Figure 5-10. Comparison between the Gringarten's solution and the test result. 86
Figure 5-11. Top view of the fracture geometry for the tests discussed above. The color indicates the height variation of the fracture surface and the dark red circle indicates the possible induced fracture front after reservoir stimulation. 89
Figure 6-1. The true and calculated conductivity of the tracer fluid and the corresponding errors. 95
Figure 6-2. The error of the calculated conduction for different standard fluid with different weight. 95
Figure 6-3. Example for the F-Φ curves with different degrees of flow geometry heterogeneity. 100
Figure 6-4. Flow rate of the injected and produced fluid and the injection pressure (Case I). 103
Figure 6-5. Concentration of the injected and produced fluid (left) and the corresponding F-Φ curves (right) (Case I). 103
Figure 6-6. Fracture on slab surface (left) and reconstructed fracture (right) (Case I). 104
Figure 6-7. Flow rate of the injected and produced fluid and the injection pressure (Case II). 106
Figure 6-8. Concentration of the tracer and produced fluid (left) and the corresponding F-Φ curves (right) (Case II). 106

Figure 6-9. Fracture on slabs at the center (top) and at Well No.2 (bottom) (Case II). 107
Figure 6-10. Flow rate of the injected and produced fluid and the injection pressure (case III). 109
Figure 6-11. Concentration of the tracer fluid and produced fluid (Case III). 109
Figure 6-12. Fracture trace on slab at the center (Case III). 109
Figure 7-1. Schematic of the sample layout (left) and a prepared sample ready to be tested (right).....115
Figure 7-2. The coordinate system on the sample surface and the coordinated of the ends of the strain gauge before and after slippage. 117
Figure 7-3. Recorded data during the test: AE activity jump and displacement jump was observed (PMMA). 120
Figure 7-4. Recorded data near the pressure breakdown (PMMA). 120
Figure 7-5. Top view and side view of the test sample with hydraulically induced fracture visible. 121
Figure 7-6. Recorded data during the test: AE activity jump and displacement jump was observed (Thistle).....123
Figure 7-7. Recorded data near the pressure breakdown (Thistle). 124
Figure 7-8. Observation of the fracture trace on the cylinder surface (Thistle). 125
Figure 7-9. Recorded data during the test: stress drop, AE activity jump and displacement jump was observed (Janis shale). 127
Figure 7-10. Recorded data near the pressure breakdown (Janis shale). 127

Figure 7-11. The location of the AE events with time evolution: the later occurrence of the near natural fracture event after the fracturing indicates the slippage of the natural fracture (Janis shale).....128
Figure 7-12. Observation of the fracture trace on the cylinder surface: the red dash line shows the hydraulic fracture trace; it turns as it approaches the natural fracture (Janis).....129
Figure 7-13. Recorded data during the test: AE activity jump and displacement jump was observed (Granite).....131
Figure 7-14. Recorded data near the pressure breakdown (Granite). 131
Figure 7-15. Recorded data near the pressure breakdown (Granite). 132
Figure 7-16. The fracture trace marked with red dash lines on the cylinder surface and natural fracture (Granite).....133

Abstract

Enhanced or engineered geothermal systems (EGS) could enable extraction of significant geothermal energy from hot relatively dry rock reservoirs. However, issues related to reservoir creation in different type of rocks and stress conditions, reservoir monitoring during reservoir creation and consequent production, better knowledge of the fluid/heat flow in the induced fracture, field management and optimization need be addressed before successful commercial development. As an effort to help solve these essential questions, a novel lab-scale EGS test system was developed to perform EGS simulation experiments on rock blocks under high pore pressure/elevated temperature and representative in-situ stress regimes while simultaneously recording Acoustic Emission (AE), self-potential (SP), temperature/pressure and tracers to characterize the reservoir creation, heating mining and flow characteristics of the system. The tests were performed on the 330 mm × 330 mm ×330 mm cubic igneous rock blocks. Two kinds of igneous rocks with different texture and permeability were tested with one injection hole and four producers (five-spot pattern). The great potential of EGS was demonstrated by the fact that about 50 watts of power was obtained by fluid flowing through the induced fracture with length of 8.9 cm and rock temperature less than 80^{o}C.

Analysis of the test results sheds light on the use of acoustic emission for better understanding of hydraulic fracturing. Also, self-potential analysis indicates SP response was mainly controlled by electrokinetic coupling and the impact of thermoelectric coupling on recorded SP is negligible as demonstrated in some field observations and modeling while the fluid concentration (salinity) has a great influence on the SP response compared with temperature gradient when the concentration contrast between the injection fluid and the

pore fluid is large due to the streaming potential coefficient reduction by the high concentration liquid. The heat circulation test shows that it is the effective fracture area instead of the total fracture area that controls the heat mining in EGS and thus the distance between injection/production wells or the location of the producer(s) and flow path tortuosity need be optimized to increase the effective heat exchange area in reservoir stimulation practice and the heat mining should be operated in a proper way to avoid well competition when multiple producers are connected to the same injection well by natural/man-made fractures. Excessive fracture propagation and high injection pressure was avoided during circulation tests by increasing the injection rate step by step. The cooling effect of the rock matrix i.e., increased fracture conductivity and lowering of the injection pressure is clearly manifested in the circulation experiments.

As the first lab-scale tracer test on EGS, the obtained result was promising. The existing of two linear tracer tail was observed in Sierra White granite test and tracer result does show a good correlation between hydraulic conductivity and the tracer concentration response. The impact of rock texture was observed. What's more, the test result could provide some useful guide for future lab-scale tracer test deign. Low permeability rock is recommended for tracer test to minimize leakage of tracer fluid into the rock matrix and also improve the fluid recovery. Low injection rate will increase the tracer time the in the fracture while proper tracer candidate with low-concentration detectability is required.

Since the in-situ permeability of most of the dry hot rocks is not high enough to support the water injection with sufficient rate, reservoir stimulation by hydraulic fracture is usually applied. Considering the comment presence of natural fractures in the underground rocks, it is of importance to analyze the interaction between the hydraulic fracture and natural

fracture. Analog experiments were conducted to investigate the interaction between a natural fracture and a hydraulic fracture with focus on slippage on the natural fracture or a bedding plane discontinuity due to an approaching hydraulic fracture. The tests were conducted on 101.6 mm diameter cylinder samples with a horizontal wellbore. The test materials included PMMA, shales, and Sierra White granite. Injection pressure, deviator stress, acoustic emission and the sample deformation are monitored during the test. In all the reported tests, the displacement calculated from the measured strain across the joint clearly shows a jump subsequent to pressure breakdown, and is accompanied by increased AE activity and decreased deviator stress. The displacement jump (slippage) across the joint with decreased deviatoric stress and AE activities on the joint from show that the hydraulic fracture caused slip of the saw-cut fractures even before reaching them. Analysis of the data clearly shows the occurrence of slippage on the joint in response to an approaching hydraulic fracture. The slippage due to the increased pore pressure on the natural fracture was also observed. Before the induced fracture reached the natural fracture, different degree of slippage (0.085mm ~ 0.11 mm) was obtained from these tests with various amount of deviator stress drop (0.14 MPa~ 0.6 MPa). Expectedly, the degree of shear slip varies with natural fracture dip, and friction angle and the differential stress. It is also observed that the pore pressure increase on the natural fracture by the encroaching hydraulic fracturing triggered larger slip on the natural fracture.

1. Introduction

1.1 Literature Review

Geothermal energy is considered as a promising option for future clean and sustainable energy supply. Currently, the utilization of geothermal energy is mainly from low and medium temperature sources (Anderson and Rezaie, 2019) and a few sites of high temperature with favorable conditions such as adequate permeability and fluids (Ghassemi, 2012). However, most of geothermal energy is stored in formations deficient in water and/or permeability. The production of geothermal energy from these reservoirs can be achieved by water circulation after reservoir stimulation to obtain engineered fracture networks consisting of man-made and preexisting fractures (joints, faults). This is often referred to as enhanced or engineered geothermal systems (EGS) (Ghassemi, 2012). Certain technical barriers need to be removed for large scale utilization of this resources (Tester et al., 2006; Ghassemi, 2012). Particularly, questions related to reservoir creation in different rock types and stress conditions, reservoir monitoring during reservoir creation and consequent production, better knowledge of the fluid/heat flow in the fractures, field management and optimization need be addressed. Laboratory scale studies present a good opportunity to help resolve some of the pending challenges along with recent field-scale efforts such as the COLLAB and FORGE projects. In lab-scale tests, the uncertainly of the test system and the test condition could be well-controlled; response of the test system could be monitored with multiple measurements at a low cost; and the direct access to the test object is available.

The permeable zones for an EGS must be created via stimulation by hydraulic fracturing. The process used to date has been somewhat different from conventional hydraulic fracturing. The objective is to design the injection process to cause shear slip and possibly

secondary fracture propagation (Willis-Richards et al., 1996; Jung, 2013; Ye and Ghassemi, 2017 & 2018; Kamali and Ghassemi, 2017). Multiple fracturing of an inclined or horizontal well can also be envisioned. This scenario has received attention (e.g., Xia et al., 2017; Kumar and Ghassemi, 2015) in view of the success of shale fracturing. To study the potential of such an approach for EGS, we performed block-scale tests in the laboratory to investigate its heat/fluid flow properties with multiple measurements.

Numerous lab-scale hydraulic fracturing studies have been conducted in the last few decades. However, most studies were carried out under ambient temperature (see Ong, 1994; Zeng and Roegiers, 2002) using cement blocks (Zhu et al., 2015), sandstone blocks, and shale (Li et al., 2018) with a single well for petroleum applications. Ghassemi and Suarez-Rivera (2012) reported tests on large blocks of shale to better understand the impact of rock fabric on fracture geometry. Craig et al. (2014) have conducted block experiments using acrylic specimens loaded in uniaxial compression and studied the role of thermal stress. But these tests did not use actual rocks and did not study the fracture area, volume, width and heat exchange surface. Solberg et al., (1980) investigated the hydraulic fracturing of small cylindrical granite samples under temperature of 25 ^{o}C and 200 ^{o}C. It is found that tensile fracture was prone to occur at rapid fluid injection rates while slow injection rates and elevated differential stress levels tended to result in shear fracture. Ishida et al., (2004 and 2012) conducted fracturing tests on granite blocks with different types of fluids (water, Oil, supercritical and liquid CO2) and it is observed that viscous oil tended to generate thick and planar cracks with few branches while thin and wavelike cracks with many secondary branches were obtained with water. Zhou et al., (2018) studied the thermal shock during hydraulic fracturing with temperature range of 20–400 °C and it was found that the initiation

pressure of hydraulic fracturing decreases with rising temperature especially with temperature higher than 200 ^{o}C. Watanabe et al., (2017) conducted hydraulic fracturing experiments under high temperature of 200–450°C to explore the possibility and characteristics of hydraulic fracturing by water and the resulting permeability enhancement in high-temperature ductile granitic samples. It was found that the pattern of the induced fracture and the break down pressure was depended on the sample temperature. Later, experiments with high temperature ($\geqslant$400 ^{o}C) was carried out on block samples (100 $\times$ 100 $\times$ 100 mm) to investigate the formation of so-called cloud-fracture network in the granite body (Watanabe et al., 2019). Recently, Frash et al. (2015) performed a series of lab-scale EGS stimulation tests with Colorado Rose Red Granite blocks. In his tests, acoustic emission during the stimulation phase was used for selecting the location of the production well(s). These studies did not use real time AE or pressure monitoring to control fracture propagation and no attempts were made to characterize the resulting fracture such as the fluid/heat flow properties.

The stimulation of a rock mass is often accompanied by multiple microseismic events (micro-earthquakes, or MEQs) which are responsible for detectable acoustic emissions (AE). These microseismic events are believed to be associated with rock failure and creation of new fluid pathways. According to current thinking, the microseismic signals contain information about the sources of energy that can be used to understand the hydraulic fracturing process (e.g., Foulger et al., 2004; Warpinski et al., 1996) and the properties of the reservoir that has been created. Detection and interpretation of microseismic events is useful for estimating the stimulated zone, fracture growth, and geometry of the geological structures and the in-situ stress state (Warpinski et al., 2001; Pine and Batchelor, 1984).

Although progress has been made in quantitative and qualitative analysis of reservoir stimulation using MEQs (e.g. Shapiro et al. 2002), several key questions remain unresolved in the analysis of microseismicity, namely the variation of seismic activity with injection rate, delayed microseismicity, the relation of the stimulated zone to the injected volume and its rate, the connectivity of fractures hosting microseismic events and the resulting reservoir permeability.

The self-potential method is a passive geophysical technique that monitors the spontaneous voltage in the earth both spatially and temporally. SP is uniquely suited for application in hydrogeologic investigations because it is the only geophysical tool that responds directly to flowing fluids in earth materials (Pritchett and Ishido, 2005; Moore and Glaser, 2007a). It is also a rapid and inexpensive approach for characterizing subsurface fluid flow since no sophisticated acquisition equipment or excitation tools are need (Nyquist and Corry, 2002). The early motivation for self-potential research in geophysics was its possible use for predicting earthquakes and mapping underground fluid flow. Therefore, extensive SP research has been carried out about anomalous SP during compression of saturated rock or fault rupture (Jouniaux and Pozzi, 1995; Lorne et al., 1999b; Yoshida, 2001; Eccles et al., 2005; Fitterman, 1978; Miyakoshi, 1986; Fenoglio et al., 1995; Varotsos et al., 1999; Triantis et al., 2012; Mizutani et al. 1976; Corwin and Morrison, 1977; Gokhberg et al., 1982; Lockner et al., 1983; Jouniaux and Pozzi, 1995; Jouniaux and Ishido, 2012), and SP surveys to characterize underground fluid flow (Butler et al., 1990; Trique et al., 2002; Fagerlund and Heinson, 2003; Revil et al., 2005; Graham et al, 2018). Later, the applications of the SP method were extended to monitoring contaminant transport (e.g. Naudet et al., 2004; Naudet and Revil, 2005; Maineult et al., 2006 a, b), mapping subsurface liquid CO_2

movement (Moore et al., 2004; Hoversten and Gasperikova, 2004; Ishido et al., 2011) and hydraulic fracturing monitoring and mapping (Pritchett and Ishido, 2005; Moore and Glaser, 2007). Revil et al. (2015) conducted lab-scale tests to explore the application of SP monitoring to locate fluid leakages from wells with good results.

Ishido and Pritchett (1999) used modeling to demonstrate that electrokinetic coupling could account for most of the production-induced changes in SP in geothermal fields. Additional numerical modeling of SP generation undertaken in geothermal and hydrological studies has been carried out (Sill, 1983; Wurmstich and Morgan, 1994; Sheffer and Oldenburg, 2007; Minsley et al., 2007; Jardani et al., 2008). Marquis et al. (2002) monitored the surface SP variation at the Soultz Hot Dry Rock site (France) during a stimulation experiment. Potential variation with a maximum amplitude of 5 mV was observed and this anomalous potential was interpreted to be related to the electrokinetic effect. Darnet et al. (2004) and Maineult et al (2006a, b) analyzed the relative contribution of electrokinetic, electrochemical and electrothermal potentials to the SP anomalies observed on the Soultz-sous-Foreˆts geothermal reservoir during cold freshwater injection and found that the electrochemical contribution is almost negligible. Ahmed et al. (2019) carried out experimental and numerical modeling to investigate the self-potential in dams and detected a self-potential anomaly with an amplitude of about −9 mV. Other field examples for SP monitoring can also be found in the literature (Anderson and Johnson, 1976; Corwin et al., 1981; Fitterman and Corwin, 1982; Finizola et al., 2002; Yasukawa et al., 2005; Garg et al., 2007; Giulia et al., 2016; Ishido et al. 2018). Moore and Glaser (2005, 2006, 2007) conducted laboratory tests to investigate the self-potential during hydraulic fracturing in granite. The test results showed excellent correlation between the pressure drop (between the injection well and the

cylindrical rock sample surface) and SP, suggesting that the SP response is created primarily by electrokinetic coupling and that a surface SP survey may provide geometrical information about an impending or recent hydraulic fracture. However, the influence of electrochemical diffusion potential and thermoelectric potential was not included. Also, their tests did not consider different electric boundary conditions.

The role of thermo-hydromechanical coupling during heat extraction from rocks has been the subject of many investigations (Kohl et al., 1995a; Cheng et al., 2001; Ghassemi et al. 2007; Ghassemi et al., 2008; Zhou et al., 2009; Ghassemi and Zhou, 2011; Rawal and Ghassemi, 2014; Tarasovs and Ghassemi, 2014; Safari and Ghassemi, 2015; Ghassemi and Tao, 2016; Cheng et al., 2019). These and most other studies have utilized the lubrication equation for flow modeling and assumed thermal equilibrium between the water and the rock. Issues such as the effect of small-scale roughness, large-scale aperture variations and nonlinearity at high Reynolds number (Zimmerman, 2012) have been considered in a few studies (Kohl et al., 1995b; Zhao and Tso, 1993). The heat transfer is of importance in geothermal reservoirs, since the product of an EGS reservoir is mainly extracted by the water flowing through the fractures. A series of tests on heat transfer by water flow in rock joint (fracture) has shown that (Zhao and Tso, 1993; Zhao and Brown, 1992) for a fixed joint aperture the heat transfer coefficient increases with flow velocity, and that as the fracture aperture increases, the heat transfer coefficient also increase especially at higher temperatures for a given flowrate. Similar to (Kohl et al., 1995b), Bai et al. (2016, 2017) conducted experiments on cylindrical granite specimens with a single fracture, with similar findings. These research studies of fluid flow in fracture with heat transfer were conducted using fracture(s) formed by splitting relatively small rock samples. Larger scale tests have

been conducted on concrete slabs (Ng et al., 2017). Frash et al. (2015) conducted Lab-scale EGS simulation of binary and triple well in large intact granite block using Acoustic Emission (AE) events for drilling guidance. However, the heat extracted from the induced fracture was negligible since the injection rate was small and thus the injected water was heated before reaching the bottom of the injection well. To our knowledge, no heat extraction experiment has been carried out in a hydraulic fracture created in a rock block.

Tracer test has a long history of application in underground practice with preliminary aim to track underground water movement. Marine (1967) employed a tracer test with tritium injection to verify an estimation of the groundwater velocity in fractured crystalline rock at the Savannah River plant. Wagner (1977) diagnosed interwell reservoir heterogeneities with field tracer test. Tester et al. (1982) employed radioisotopic tracer techniques using I^{131} and Br^{82} with downhole gamma logging to characterize quantitatively flow at injection and production points in hydraulically fractured region in granite. Maloszewski and Zuber (1993) demonstrated that the single fracture dispersion model with matrix diffusion could better describe the field tracer tests. Later on, extensive research about tracer technique in geothermal application has been carried out with focuses on the feasibility of different types of tracer (Deeds et al., 1999; Adams, et al., 2001; Rose et al., 2001; Nottebohm et al., 2010; Nottebohm et al., 2012; Serres-Piole et al., 2012; Becker et al., 2013; Ames, 2016; Schaffer et al., 2016; Hawkins, 2017; Aydin et al., 2018; Kong et al., 2018; Kuo et al., 2018; Reimus et al., 2018; Suzuki et al., 2018; Zhang et al., 2015, 2016, 2017), field scale tests (Axelsson et al., 2001; Yeltekin and Akin, 2005; Sanjuan et al., 2006; Hawkins et al., 2015; Leong et al., 2015; Kristjánsson et al., 2016; Akin and Gulgor, 2018; Christensen et al., 2018) and interpretation of tracer data with different methods (Niibori et al., 1995; Shook, 2001; Wu

et al., 2002; Becker and Shapiro, 2003; Axelsson et al., 2005). Wu (2006) developed a tracer selection protocol based on literature review and systematic simulation of tracer injection. Some numerical modeling of tracer tests can be found in literatures (e.g., Pruess, K., 2002; Guo et al., 2016; Tian et al., 2016; Hawkins et al., 2017). Dean et al (2015) conducted a series of laboratory experiments to quantify the cation exchange behavior of Li+ and Cs+ in the Newberry Crater system to facilitate interpretations of the single-well tracer test and thus the test was mainly about the tracer characteristics. In the recent EGS Collab project initiated by DOE Geothermal Technologies Office (GTO), different types of tracer were injected and detected in three flowing wells about 7.5 to 9 meters away from the injection interval. However, most of the test data is still under analysis (Mattson et al., 2019). Despite the extensive research on tracer testing, to our knowledge there are no laboratory scale tracer tests on rock fractures to simulate the tracer response in an EGS system reported in the literature.

As mentioned, hydraulic fracturing is usually employed for the creation of enhanced/engineered geothermal systems (Zimmermann et al., 2010). Since most of the underground rock is fractured to some degree (Lamont and Jessen, 1963), it is of importance to consider the interaction between hydraulically induced fracture and the pre-existing geological discontinuities such as cracks, joints, and faults. Natural fractures (NF) in the oil and gas reservoir or geothermal formation could lead to a complex hydraulic fracture geometry (Nelson et al., 2007) during the stimulation treatment. Therefore, it is always of great interest for researchers to obtain a better understanding of the interaction between hydraulically induced fracture and the natural fractures. Zoback et al (1977) investigated the influence of pre-existing cracks on the orientation of generated fracture under uniaxial

condition. Blanton (1982, 1986) carried out hydraulic fracturing experiments with per-existing fracture in the blocks and found that found that hydraulic fractures tend to cross pre-existing fractures only under high differential stresses and high approaching angles and that in most cases the hydraulic fractures were either diverted or arrested by the preexisting fractures. The test conducted by Warpinski and Teufel (1987) illustrates the complex nature of actual fractures could be created in a naturally fractured formation and provides insight into why the results from a fracture treatment can be less than anticipated. Olson (2012) performed tests to examine the effect of cemented natural fractures on hydraulic fracture (HF) propagation and found that oblique embedded fractures are more likely to divert a fluid-driven hydraulic fracture than those occurring orthogonal to the induced fracture path. Bunger et al (2015) conducted lab-scale test to investigate the HF/NF interactions in which the natural fractures are unbonded machined frictional interfaces. Kim et al (2017) conducted experiments on analogue rock samples (soda-lime glass) with preexisting cracks and layers and compared the result with numerical models. Other experimental effort could be found in literature such as (i.e, Xing et al., 2018; Dehghan et al., 2015; de Pater and Beugelsdijk, 2005). The possible interaction between a HF and a NF can be classified as crossing and arresting (no-crossing) (Blanton, 1982). Criteria to predict whether a HF will cross a pre-existing natural fracture or not have been developed (i.e, Renshaw and Pollard, 1995; Blanton, 1986; Gu and Weng, 2010; Sarmadivaleh and Rasouli, 2013). However, all tests and criteria are about whether the hydraulic fracture will cross the natural fracture or not and how the crossing pattern and the complex fracture pattern due the existing of natural fractures. But there is rare study focusing on the influence of an approaching fracture on the natural fracture before the hydraulic fracture reaching the natural fracture. Before the

intersection of the natural fracture and hydraulic fracture, the induced fracture disturbs the stress distribution in the material including and the leaking off of the fluid from hydraulic fracture into the surrounding rocks will increase pore pressure and both mechanism could active the natural fracture. The pore pressure increase on the natural fracture could cause it to slip due to the decrease of normal stress acting on the natural fracture. The pore-pressure-increase caused slip has got a lot of attention recently since it is more common to occur (Keranen et al., 2014; Guglielmi et al., 2015; Ye and Ghassemi, 2018). However, the mechanical stress induced from the hydraulic fracture could also cause slippage of the natural fracture. Numerical models have been used (Gao and Ghassemi, 2019; Koshelev and Ghassemi, 2003a, b; Dobroskok and Ghassemi 2004) to study the details of mechanical interaction between a hydraulic fracture and a natural discontinuity. The latter showed that the fault inclination and frictional characteristics, as well as the conditions on the fracture surfaces are the most significant factors that influence the fracture trajectories. Whether the fracture is arrested or propagates by a jog at the interface is influenced by its trajectory and whether it is attracted or rejected by the natural fracture (Koshelev and Ghassemi, 2003 a, b). Sesetty and Ghassemi (2012) considered details of NF/HF interactions and flow using the displacement discontinuity method (DDM). It was found that the injection pressure tends to vary with the angle of approach to the natural fractures and the latter's orientation. The pressure tends to decrease as the hydraulic fracture grows in length, until it intersects the natural fracture when it starts to increase during the opening and propagation of the natural fracture. However, the actual mechanical interaction between a hydraulic fracture near a natural fracture or a bedding plane discontinuity has not been experimentally studied, particularly under triaxial stress and hydraulic fracturing conditions. In this work,

experimental investigation is presented to clearly illustrate the deformation and slippage of a natural fracture or bedding plane by an approaching hydraulic fracture, a phenomenon suggested by moment tensor inversion of the field data (Kahn et al., 2017) and previous numerical modeling (Koshelev and Ghassemi, 2003a, b).

1.2 Motivation and Objectives

The goal of this research is to investigate some of the essential issues that provide challenges to the development of geothermal energy in the deep hot formations. To achieve this, a new lab-scale EGS test protocol has been developed and used that allows replication of reservoir creation, production, characterization of the EGS. This work improved the state-of-the-art by allowing the simultaneous monitoring of Acoustic Emission (AE), self-potential (SP), temperature/pressure and tracers during the stimulation and circulation phases. Advanced experimental designs would be developed to assess hydraulic fracture geometry, injectivity measurement, heat extraction, and a tracer test to characterize the EGS system.

In addition, the NF slippage of a natural fracture due to the induced stress of an approaching hydraulic fracture would be investigated with cylindrical samples as an effort to supplement our current understanding of the HF/NF interaction knowledge. Different materials including PMMA, shales and granite were tested to demonstrate the repeatability of the observed phenomenon. The experimental analysis helps better explain some of the field observations during hydraulic fracturing operation and contribute to better design practices.

1.3 Dissertation Outlines

The necessity and importance of the lab-scale investigation of the enhanced/engineered geothermal system is disused and a literature review is presented in Chapter 1. Motivation and specific objects of this research are also discussed in this chapter.

Chapter 2 first provides an overview of the lab-scale EGS test system with detailed information about the major subsystems. Test setup such as sample preparation and characterization and test procedure are also included.

Chapter 3 focuses on the acoustic emission monitoring of the reservoir creation phase of an EGS i.e., hydraulic fracturing and then characterization of the induced fracture including injectivity, fracture geometry, surface profile, thin section and SEM observation are discussed.

Chapter 4 described the self-potential response in the lab-scale EGS simulation which investigates the influence of different parameters and test conditions (temperature, fluid concentration, rock porosity, saturation condition) and the rock boundary conditions on the SP results.

Chapter 5 presents the results from different scenarios of lab-scale heat mining experiments. Test results and findings from four cases are analyzed to obtain a better understanding of the heat/fluid flow process through the induced fracture.

Chapter 6 provides the results of tracer tests. The method to calculate the tracer concentration from test data was first given and verified with standard fluids. Method of Moment and F-

Φ curves are also used qualitatively and quantitatively to interpret the test result from three cases.

Chapter 7 provides the experimental work on the HF/NF interaction study. Test setup and procedures is discussed and the calculation of the slippage on the natural fracture from the recorded data is given with some results from four cases on different materials.

Finally, in chapter 8, a summary and conclusions of the study are described and the major findings of this work are outlined.

2. Lab-Scale EGS Test System

2.1 Overview of the Test System

To simulate the EGS creation, production and characterization, a novel lab-scale EGS test system including several integrated subsystems was developed. The main subsystems include: a polyaxial loading frame, hydraulic fracturing and circulation system, Acoustic emission (AE) monitoring and analysis system, Self-potential (SP) acquisition systems, pressure/temperature acquisition system, and tracer systems. The core of the newly developed system is the polyaxial frame which has the capacity to accept and load a cubical rock sample with three independently controlled principal stresses. It can be heated up to a uniform temperature near 100^{o}C with water inside the frame. Another unique feature of the frame is the feasibility of having pore pressure as high as 10 MPa in the sample. Sensors are used on the block surfaces, within cavities, and in the wellbores to characterize and locate acoustic emissions caused by the stimulation, and to monitor local changes in fluid pressure, temperature, and SP. The test system allows us to replicate aspects of the EGS hydraulic fracturing treatment and heat production in the field. The reservoir stimulation (hydraulic fracturing) is usually conducted without fluid in the frame to minimize the noise level for better acoustic emission monitoring. After the mini-EGS is created, cold water is injected and simultaneously collected from nearby miniature production wells to characterize the fluid/heat flow in the induced hydraulic fracture. Following circulation test, a tracer test is usually carried out to simulate field scale tracer application. The tested block sample is sliced to scan the hydraulic fracture profile and to reconstruct the fracture geometry in 3D. In the next subsections, detail information of the main subsystems will be provided.

2.2 Polyaxial Loading Frame

To provide independently controlled principle stress condition on the block sample with elevated temperature and pore pressure condition, a new polyaxial loading system was designed and manufactured. The polyaxial cell consists of a cylindrical loading rig and bottom and top lids that were made of high strength steel. The loading cell has a cavity with dimensions of 520.7 mm (20.5 inch) by 520.7 mm (20.5 inch) by 482.6 mm (19.0 inch), which makes large block test up to 457 mm (18.0 inch) cubic possible. All the steel components of the polyaxial frame was coated with a special coating to prevent rusting under contact with water and other corrosive fluids. Flat-jacks are used to apply controlled stresses on the block sample with different magnitudes of overburden stress, σ_v, maximum horizontal stress σ_H, and minimum horizontal stress σ_h up to 70 MPa. The loading frame can be sealed with high pore pressure in the rock (around 10 MPa) and be heated up to near 100 ^{o}C by circulating hot water between the frame and the heat resource and it has the potential to work with high temperature of 200^{o}C.

Figure 2-1 (left) illustrates the partially assembled polyaxial frame, showing the bottom lid, the rock block to be tested, steel spacers, and the bottom flat-jack. The fully assembled frame is shown in Figure 2-1 (right). Foam insulation (red) and a Faraday cage jacket (the black cover shown) are placed around the frame to minimize the heat loss during circulation and electrical noise, respectively.



Figure 2-1. Partially (left) and fully (right) assembled frame

Five flat-jacks (four on the sides and one on the bottom) are used to apply the principal stresses. Before use, each flat-jack must be calibrated to obtain the relationship between the pressure inside the jack and the force generated. During calibration, the bottom-top distance (thickness) of the flat-jack is maintained at 25.4 mm (1.0 inch) and then oil is injected into the flat-jack to create a high pressure inside. After the pressure is stable with zero injection rate, the force needed to maintain the flat-jack thickness constant is recorded. Repeating this for different pressures, one can obtain the pressure and force curve. Figure 2-2 shows an example of the calibration data, and there is a very good linear relationship between the pressure in the flat-jack and the generated force.

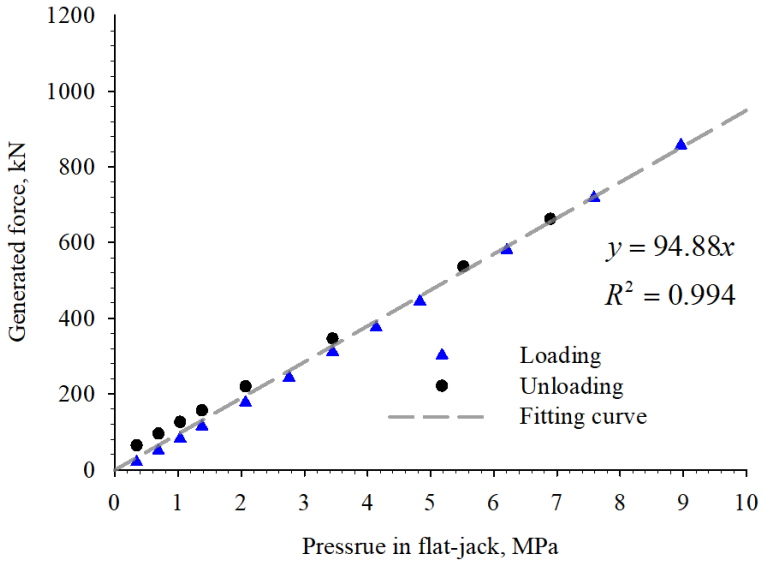


Figure 2-2. A typical flat-jack calibration result with flatjack thickness maintaining at 25.4 mm

2.3 Sample Preparation

Though the loading frame can accept block sample with different sizes, the tested samples up to now were 330-mm cubical blocks with one injection well and four production wells drilled from the top surface. Figure 2-3 (left) is a top view showing the layout of the wells and sensors on the top surface, and Figure 2-3 (right) is a longitudinal sectional view of the sample showing the interior layout of the wells. The injection well had a depth of 171.5 mm (measured from the top surface) and a diameter of 20.1 mm. The production wells were drilled to a depth of 190.5 mm to facilitate connection by a hydraulic fracture. A circular notch was made in the injection wellbore at a depth of 165.1 mm to facilitate the fracture initiation. High strength epoxy was poured into the hole to seal the annulus between the injection tubing and the wellbore wall with certain length of unsealed open interval. The unsealed open interval in the injection well is shorter than that in the production wells, and

their lengths were different in some tests. However, the open intervals were symmetric about the rock block's middle horizontal plane and the temperature in the wellbores was measured in the middle of the open interval for all tests. Four production wells were drilled 88.9 mm away from the injection hole. The diameter of the production wells is 10.2 mm. Epoxy cylinders with slightly smaller diameters than the wellbore was placed at the open intervals to reduce the open space in the wellbores to minimize the effect of wellbore storage on the tracer test. They also served to minimize the air in the wellbores which could influence the fracture initiation and propagation. The hydraulic tubing did not reach the center of the open interval in the wellbores (it stopped 12.7 mm (0.5 inch) short of the center, and a plastic tube was added its end to reach the center) in order not to interfere with SP measurement during the experiments. A thermistor was placed at the bottom of the wells, 1-2 mm to the side of the plastic conduit, to record the fluid temperature. Thermistors were also placed on the surfaces of the block to monitor the block boundary temperature. There were two thermistors on the top surface with one near the injection tubing and one about 64 mm away from the center of the top surface, while one thermistor was placed in the middle of other block surfaces. Extra thermistors were put in the frame near the water inlet and outlet (water was circulated between the frame and a heating source to increase and maintain the sample boundary temperature) and on the outer surface of the frame for better temperature monitoring (during circulation test). The space between the rock block and the inner surface of the loading frame is occupied by flat-jacks, and PEEK or aluminum/steel plate spacers. Analysis of the test results shows that if SP is the main concern of the test, PEEK plates should be put directly on the rock surface to insulate the sample from surroundings while if constant temperature boundary is more important for the test, aluminum plates should be

used instead. After the sample is placed into the frame and the frame is fully assembled, principal stresses were applied by injecting oil into the flat-jacks to predetermined pressure levels according to the desired stress condition. The vertical stress was set as the minimum principal stress and thus a horizontal fracture was expected to connect with the production wells.

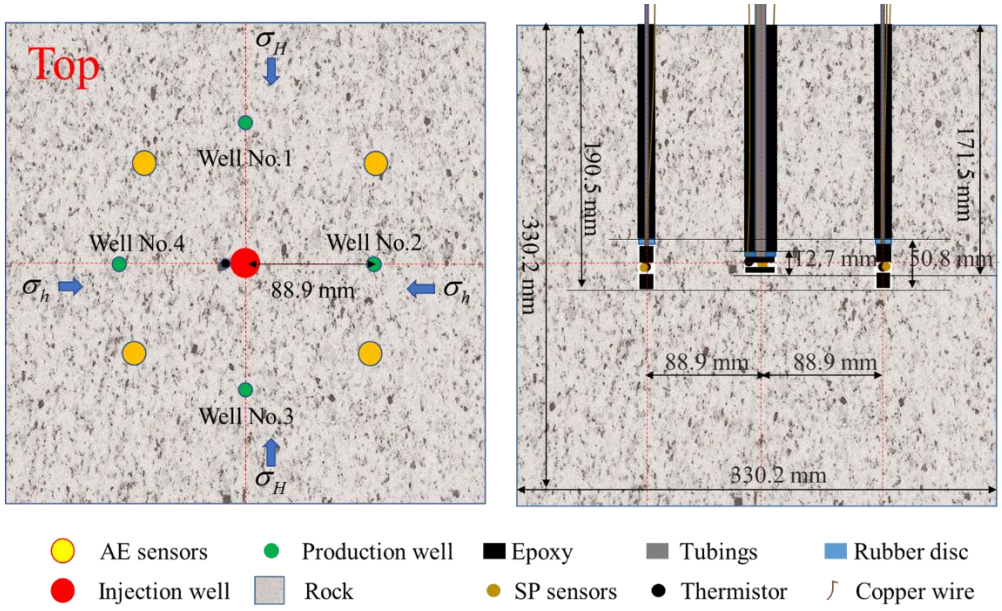


Figure 2-3. Top view (left) and longitudinal sectional view (right) of the wells and sensors

Figure 2-4 is a picture of the slab cutting from a tested sample, showing the layout of the wellbore bottom. The hydraulically induced fracture trace on the cutting surface was marked out with the pencil line, and it clearly shows that the induced fracture initiated from the tip of the notch. Experience from the tested block indicates that a notch (about 2.0 mm depth and 1.5 mm width) with good quality is one of the key factors for obtaining an ideal fracture geometry, especially in our case in which water (low viscosity fluid) was used as the fracturing fluid. Improper notch will result fracture propagating towards to one/some prefer

direction(s). If no notch was applied the fracture usually initiated at the corner of the wellbore bottom where stress concentration occurs. In Figure 2-4, the epoxy cylinders and thermistors in the production well are visible while the injection and production tubing, the thermistor (in the injection well) and SP sensors were cut away from the slicing.

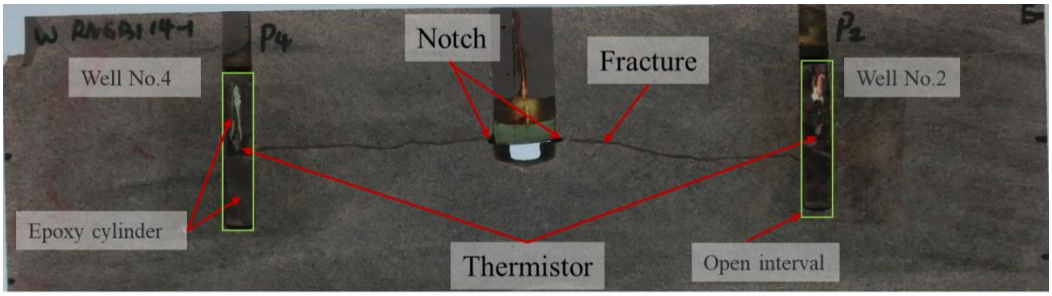


Figure 2-4. An example picture of a slab cutting from a tested sample

2.4 Acoustic Emission and Self-potential Survey

The Acoustic Emission (AE) technique is widely used to detect material failure. However, compared with lab-scale hydraulic fracturing tests reported in the literature, our test environment (temperature, pressure, submerged in water) is very harsh for most commercial AE sensors, so newly designed AE sensor were used for this project. To allow the AE sensors to be reused, 12.7 mm diameter 500 kHz piezoelectric crystals provided by Boston Piezo-Optics Inc. were attached to co-axial wires and the positive side is covered with epoxy. In a block test, twenty AE sensors were attached on all sizes of the block. The AE sensors were placed in shallow holes drilled on the rock surfaces. The bottom of the holes was filled with high strength epoxy to create an even surface for attaching the AE sensors (as shown in Figure 2-4 at the top left corner). To improve the location determination, the AE waveforms were recorded at a high sampling rate of 10 MHz.

As shown in Figure 2-3, SP sensors were placed at the center of the open interval for each well and the one in the injection well serves as the reference electrode. The SP sensors were made by soldering a coated copper cable to a thin circular copper sheet (pure copper was selected as the electrodes because of its low cost, ease of preparation and successful use by other researchers e.g., Moore and Glaser, 2005). The CR1000 provided by Campbell Scientific was used as the SP data logger. It has an input impedance of 20 GΩ, which is high enough compared with the rock's resistance (the resistivity of a saturated Sierra White granite sample with 0.001M NaCl is about 8,000 Ω-m, Moore, 2007; the resistivity of dry granite could be as high as 1MΩ-m, Schön, 2015). The recorded SP is the voltage difference between the measurement points (production wells and block surface) and the reference electrode in the injection well (while the pressure difference is calculated by subtracting the pressure at the measurement point from the injection pressure). Due to this calculation approach, the ratio of voltage difference to pressure difference has an opposite sign to the streaming potential coefficient. This was done for simplifying the visualization of the coupling coefficient variation with pressure drop.

2.5 Circulation System and Heating System

Figure 2-5 shows the schematic diagram of the circulation test setup. Two syringe pumps were used for the cold-water injection. Both pumps were covered with ice bags and then wrapped with white cloth insulating strips to keep the injection water (0.002 mole/Liter Sodium Chloride solution) at a desired low temperature. To achieve continuous cold-water injection, the pumps were operated inter-changeably to allow refilling. The produced water was periodically collected with bottles of known weight to calculate the production rate with

the produced water weight and the collection time. The injection water used to refill the pump was stored in titration flasks in an ice box to be pre-cooled.

The injection tubing connecting the injection pumps to the bottom of the injection wellbore has an inner diameter of 0.81 mm (0.032 inch) to minimize the resident time of the water in the tubing and thus to obtain a lower temperature at the wellbore bottom. Hydraulic tubing with the same dimeter was used for the production wells. Other strategies were employed to help lower the water temperature at the injection well. Firstly, thermal insulation foam and then white cloth strips were wrapped round the injection tubing (the section outside the frame) to reduce the heat transfer from the air to the water inside. Secondly, a section of the injection tubing with length about 3 meters (illustrated with a spring in dash box in Figure 2-5) was submerged in ice water to cool the water before entering the frame. At last, the section of the injection tubing inside the loading frame above the wellhead was covered with rubber cylinders to reduce the heat transfer from the surrounding hot water in the frame.

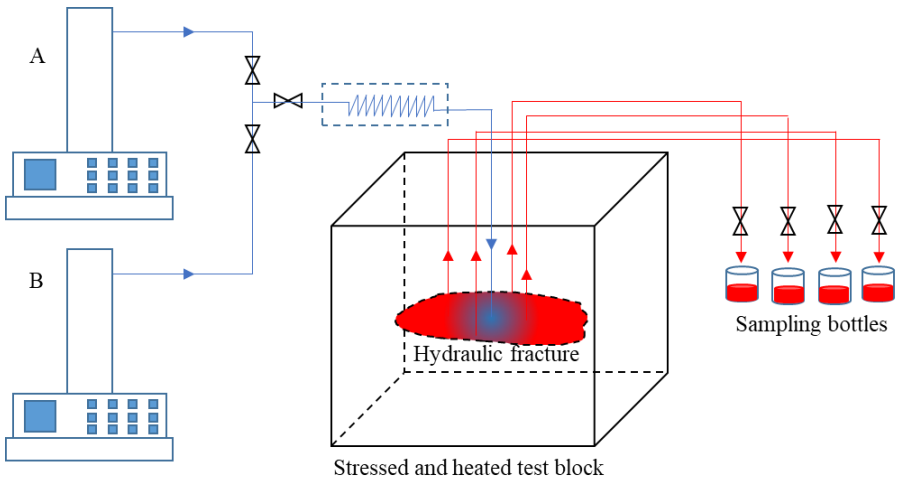


Figure 2-5. The schematic diagram of the circulation test setup

The tested rock (including everything inside the loading frame) was heated up to a uniform level after hydraulic fracturing. To heat up the rock rapidly and to maintain its boundary temperature during circulation, hot water was circulated in the frame to heat exchange with the rock block. A high-power water heater of 30,000 W and a low-power heater of 3,000 W were applied for heating and maintaining the boundary temperature during the circulation test. During circulation, the low-power heater was switched on and off based on the recorded temperature on the rock surface. To minimize the heat loss to the air during heating and circulation test, the loading frame was wrapped with foam insulation and insulating blankets (In Figure 2-1, only the red blanket is visible). Figure 2-6 shows an example of the temperature history during the heating process before circulation starts indicating that the rock sample was heated up to a uniform temperature of 67.0 ºC from room temperature within 17 hours. At the early phase of the heating, both the high-power heater and the low power heater were working and later only low-power heater was on for safety overnight. The heating process usually started in the afternoon and the circulation test conducted the next day.

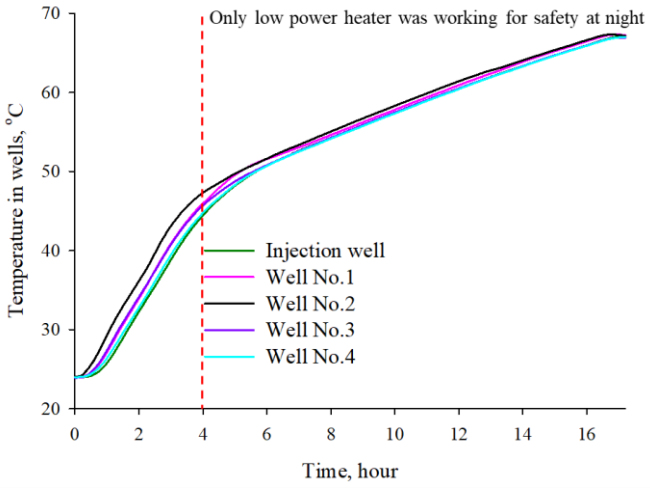


Figure 2-6. An example of temperature history in wells during heating process

2.6 Tracer test system

The simplified schematic diagram of a tracer test setup is similar to what is shown in Figure 2-5. The difference is that the 3-meters injection tubing was removed to have a shorter flow path for the tracer before entering the wellbore bottom. As mentioned before, the tracer test was conducted after the fracturing and circulation tests. In a tracer test, water containing the tracer was injected into the fracture interval via the injection well, and it was collected from the producer(s). Two syringe pumps were used to accomplish the tracer injection. Syringe pump A was used to inject a high concentration (1.0 mole/liter) Sodium Chloride (NaCl) solution into the well while pump B was for sodium chloride (NaCl) solution with low concentration (0.002 mole/liter). The reason of selecting NaCl solution as the tracer is that it is low-cost, no environmental impact, and its relative ease of preparation. In the initial phase of a tracer test, the low concentration NaCl solution was injected into the fracture/matrix system to establish a steady state flow condition. After injecting for some time (usually more than 5 minutes), pump A starts (while pump B is shut) to inject the high concentration solution continually for about 10 minutes. This step replicates a tracer pulse. When the injection of the high concentration tracer pulse completed, the injectate was switch back to the low concentration solution using pump B. During the entire process, the produced fluid was collected periodically. The sampling rate was different for different wells (about forty seconds per sample to ten minutes per sample), since their production rates were different. The weight of the collected fluid for most of the samples was more than 0.2 g to ensure the accuracy of conductivity measurement. The reason of selecting NaCl solution as the tracer is that it is low-cost, no environmental impact, and its relative ease of preparation.

2.7 Sample Characterization

Two types of igneous rocks were tested namely Sierra White granite and Raven Noir gabbro. They were acquired from Cold Spring Company (www.coldspringusa.com). Common triaxial tests were carried out on samples of these rocks to determine the mechanical properties. Figure 2-7 shows an example of the strain-stress curve of these two types of rock with confining pressure of 34.5 MPa. The loading was applied with damage control (refer Li 2017 for more detail information) to obtain the complete failure curve and it is found that Raven Noir gabbro is still featured with brittleness character under high confining pressure and has a much higher elastic modulus. Table 2.1 lists the basic properties. The permeability of Sierra White granite was measured using a 1.27 cm thick disc. Using a 0.69 MPa upstream pressure and 0.34 MPa downstream pressure, the measured permeability from this 2.54 cm diameter disc is about 680nD. Other properties such as bulk conductivity of Sierra White granite can be found in (Moore, 2007). Due to extremely low porosity and permeability of Raven Noir gabbro, these two properties was not measured and the gabbro can be reasonably treated as solid nonporous material. The mineral composition of the rocks was measured using the Powder X-Ray Diffraction (XRD) method and the result shown in Table 2.2 indicates Quartz and Albite dominate the mineral contents of Sierra White granite while Raven Noir gabbro was dominated by Diopside, Phlogopite and Anorthite.

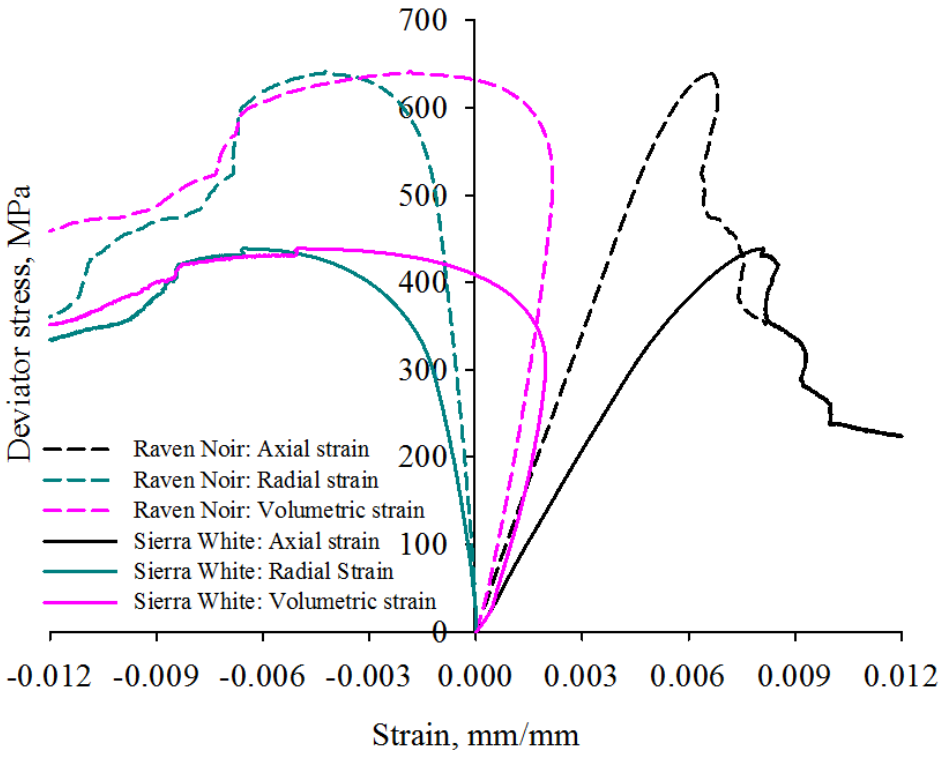


Figure 2-7. The strain-stress curve for Sierra White granite and Raven Noir gabbro with confining pressure of 34.5 MPa.

Table 2.1. Mechanical properties of the tested rocks

Rock type	**Sierra White granite**	**Raven Noir gabbro**
Density, g/cm^3	2.62±0.01	3.09±0.01
Porosity, %	0.8±0.2	-
Permeability, nD	680±200	-
Young's modulus, GPa	68.2±2.6	111.7±2.1
Poisson's ratio	0.27±0.01	0.24±0.03
UCS, MPa	205.7±5.8	300.9±16.8
Cohesion, MPa	38.3±1.4	57.8±4.4
Friction angle, degree	49.1±0.8	48.0±1.1
Tensile strength, MPa	10.68±1.27	16.3±2.0

Table 2.2. Mineralogy of the tested rocks

Sierra White granite		Raven Noir gabbro	
Quartz	43.5%	Diopside	28.47%
Albite	46.2%	Phlogopite	27.82%
Sanidine	4.8%	Anorthite	18.98%
Biotite	2.7%	Cordierite	9.43%
Minor mineral	2.9%	Microcline	8.12%
		Quartz	5.49%
		Albite	1.69%

As stated before, the circulation fluid was 0.002 mole/Liter NaCl solution, i.e., the same as the fluid used for the hydraulic fracturing and tracer test. Consider the concentration of NaCl is very low, its properties are assumed to be same as that of the pure water. Figure 2-8 gives the viscosity and density of pure water at the temperature range under standard atmosphere pressure during this project (data source: https://wiki.anton-paar.com/en/water/). It is observed that the density variation of the fluid less than 3 % within the temperature range between 2^{o}C to 80^{o}C while the viscosity has a much larger variation. In this project, the bottom hole temperature of the injection well under high injection rate (i.e., 25 ml/min) was about 20 ^{o}C and the water temperature at the bottom of the production well was as high as 70^{o}C. Therefore, the viscosity of water decreased about 65 % as the water traveled from the injection well to the production well (Figure 2-8). This viscosity change influences the pressure profile in the facture.

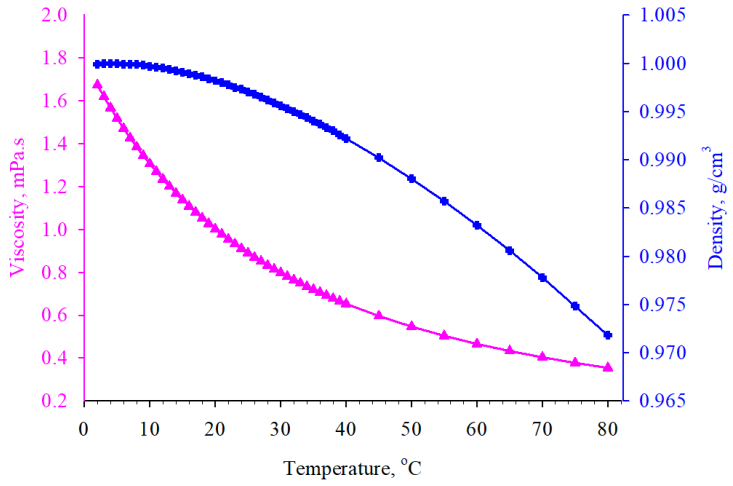


Figure 2-8. The density and viscosity of water under different temperature with standard atmosphere pressure.

Figure 2-9 shows the density, viscosity and conductivity of NaCl solution under different concentration (Zhang and Han, 1996; Foxboro 1999) at room temperature. It can be seen the density and viscosity change very little over a large concentration range and their linear relationship is conducive to simplified analysis. The tracer is also readily distinguishable from the rock minerals that may dissolve during the test. Based on the composition of the tested granite (discussed below), the amount of minerals dissolved into the produced fluid is not significant. The concentration of the produced NaCl solution can also be readily determined from the measured conductivity of the collected fluid, avoiding the need for complicated and expensive laboratory test equipment.

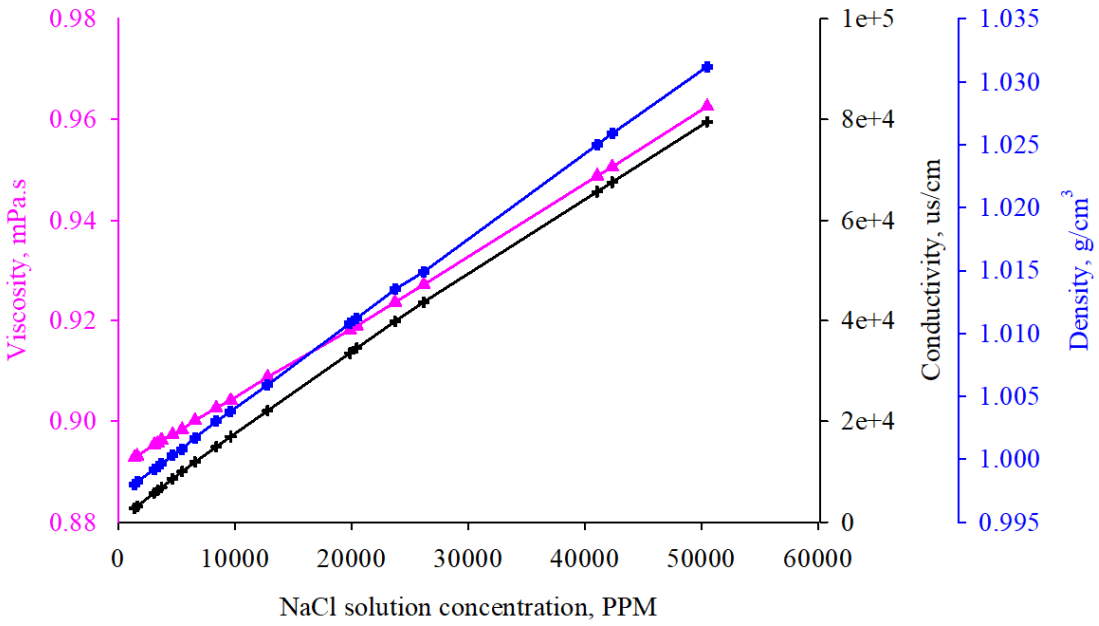


Figure 2-9. The viscosity, conductivity and density of NaCl solution with different concentration.

2.8 Test Procedure

Table 2.3 shows the overall test procedures in detail. The main idea is first establishing the hydraulic connection between the injection and production wells by hydraulic fracturing and then circulating cold-water between the wells to characterize the fluid/heat flow properties of the induced fracture(s) after heating the system up to a uniform temperature. The stimulation was performed at room temperature to eliminate the role of thermal stress for better fracture control and analysis. After a circulation test, tracer test was carried out by injecting a tracer and collecting it via production wells to investigate the fracture volume. After the whole test, the induced fracture was reconstructed in 3D by cutting the sample into slabs and observing the fracture trace on the cut surfaces.

Table 2.3. Lab-scale EGS simulation test procedures.

Step	Action	Recorded information	Days needed
Step 1	Sample preparation, system assembly	Location of sensors, dimensions	10-14
Step 2	Check connection/signal quality, Apply principal stresses (and pore pressure)	-	3
Step 3	Injection index test, hydraulic fracturing	AE, SP, flow rate, pressures	1
Step 4	Heat the rock	Temperature history	2
Step 5	Injection index test, Circulation test	Temperature, AE, pressure flow rate	1
Step 6	Tracer test, Injection index test	Pressure, flow rate, AE tracer concentration	1
Step 7	Disassemble, fracture geometry reconstruction	Real 3D fracture geometry	7
Step 8	Analyze test data	Report result	7

3. Characterization of Laboratory-Scale Hydraulic Fracturing

3.1 Controlled Fracture Propagation

The first key step for a successful test is to control the fracture initiation and propagation, which has not been extensively investigated before. Unlike traditional experimental hydraulic fracturing tests with no restriction on the final fracture extension, the induced fracture in this project was expected to intersect multiple production wells meanwhile to be maintained in the sample block without reaching the surfaces. Since water is commonly applied as the fracturing fluid in EGS and to avoid two phase flow in the subsequent circulation tests, the 0.002 mole/Liter NaCl solution (the NaCl was added for Self-potential survey during the stimulation and consequent circulation test) was selected as fracturing fluid. The injection rate for most of the tests was no higher than 2.0 ml/min while for the near non-porous Raven Noir gabbro the injection rate was 0.5 ml/min. The injection pump was programmed to go into backflow (a flowrate of 100 ml/min) mode or reduce the injection rate when the injection pressure drop between two consecutive data points (recorded every 0.5 second) exceeded a preset value of 0.28 MPa. When injecting to create a hydraulic fracture, the production wells were shut in and the pressures were monitored. If the pressure in a well exceeded 3.45 MPa, the valve for the well was opened to the atmosphere to prevent further propagation. It turns out that the mentioned techniques worked very well. Figure 3-1 is an example where all four production wells were connected by the induced fracture without having the fracture reaching the block surface. It is also found if the production wells were open during fracturing, the induced fracture would have a lower change to reach the rock boundary (Hu et al., 2017b), as also demonstrated by (Frash et al., 2018) with high viscosity fluid (greater than 7,000 cP). Due to the low viscosity of the fluid,

the fracture tends to propagate fast. If the injection was not stopped in time, the fracture would reach the rock boundary within a couple of second.

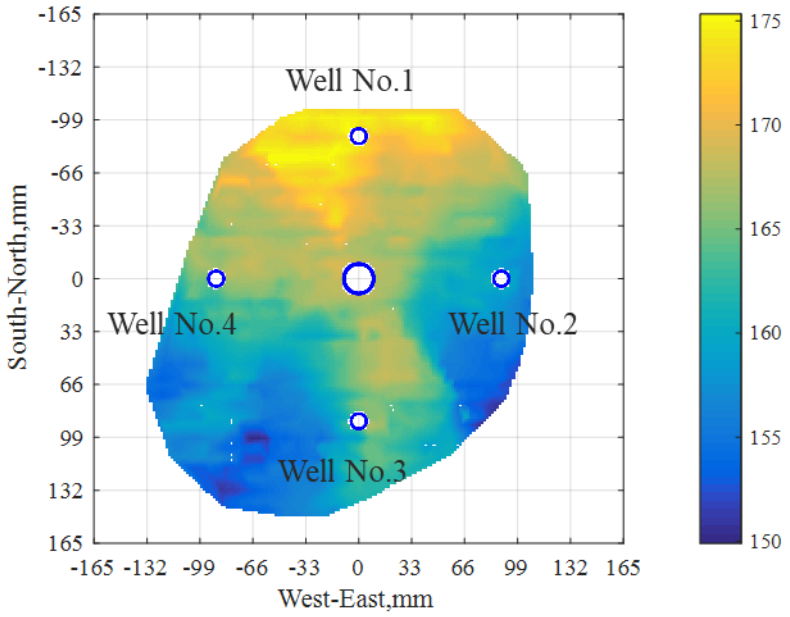


Figure 3-1. The reconstructed induced fracture geometry from a Raven Noir gabbro block. The fracture was mainly induced during reservoir stimulation, and there is no parent fracture extension during the following tests (Hu et al., 2018b)

3.2 Breakdown, Acoustic emissions

3.2.1 Stimulation under Low In-situ Stress Condition

Initially, block tests were conducted at a low stress level and the observed AE activity was found to be very low. For instance, Figure 3-2 shows data recorded during a stimulation test of Sierra White granite block with a low stress level of 3.4 MPa (500 psi) vertical stress, 6.9 MPa (1000 psi) minimum horizontal stress and 10.3 MPa (1500 psi) maximum horizontal stress. The vertical stress was set to be the minimum for a horizontal fracture to have a better chance of connecting with the production wells. The injection rate was initially set to 2.0 ml/min but was reduced to 0.02 ml/min after breakdown using an injection control algorithm.

Ninety seconds later, the injection rate was reset to the initial value and this second injection stage lasted about 52s. It is noticed that during the entire hydraulic fracturing period (including the first and the second injection stage), only about 150 acoustic emission hits were recorded, and only 15 acoustic events were located based on the time difference when these hits were received by the AE sensors at different location on the block surface. This is likely caused by the relatively low energy released during fracture initiation and propagation under low stress levels. Subsequent tests conducted at higher stresses showed significantly more AE.

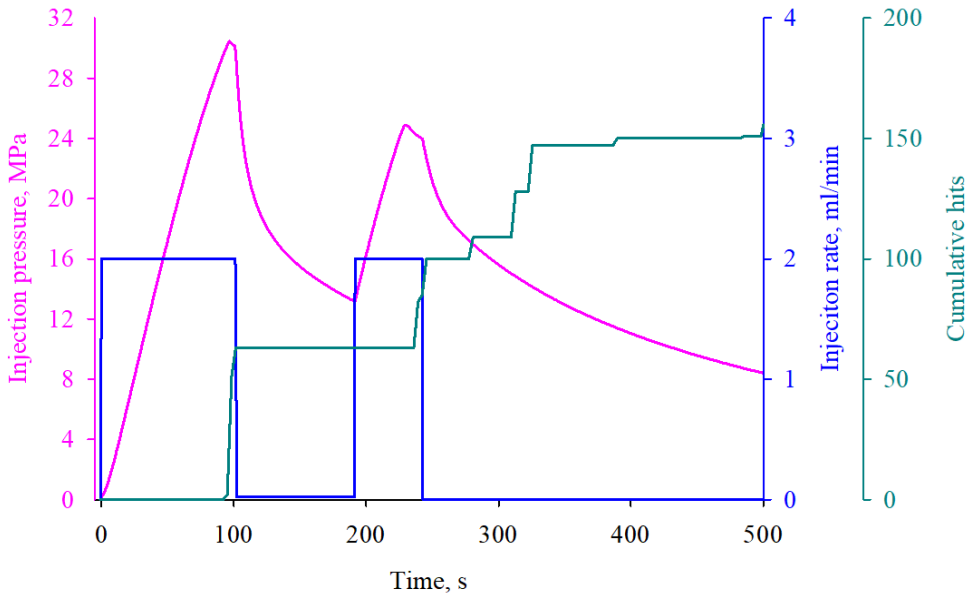


Figure 3-2. The recording data from hydraulic fracturing test with low stress level

During these two injection stage tests (HF and SCF), all production wells were shut-in and the pressure changes in these wells were recorded (Figure 3-3, left). From the pressure record, it is obvious that Well No.1 was intersected by the induced fracture. Also, it can be interpreted that early in the hydraulic fracturing process, the induced fracture propagated

toward Well No.1 for a small distance but it did not intersect it. The pressure in Well No.1 continues to increase to 1.7 MPa even after injection stopped, indicating that the fracture is in its close vicinity. After starting the second period of injection, the fracture became fully connected with Well No 1. Figure 3-3 (right) shows the relative location of the AE events and the wells. Although not many AE events were obtained, their distribution (Figure 3-3, right) provides a very good indication of the fracture propagation direction which agrees very well with the pressure behavior of the production wells.

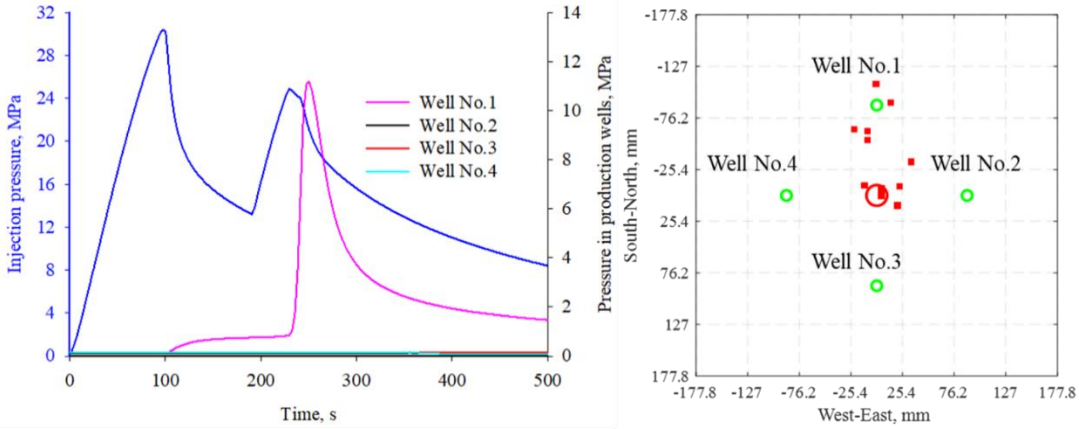


Figure 3-3. The pressure history in wells at low stress level fracturing test. Red rectangles in the right-hand figure denote locations of AE events.

3.2.2 Stimulation under Higher In-situ Stress Condition

After several low in-situ stress tests, we carried out tests with a higher stress level with Sierra White granite blocks to lower the impact of rock texture on the overall fracture geometry (reduce its curving up or down) and to increase the AE levels. The stress in all principal directions was increased by 3.4 MPa (500 psi). As mentioned above, the hydraulic fracturing test was conducted without saturating the whole block. However, about 100 ml 0.002 mole/L NaCl was injected before the fracturing test by maintaining the pressure at the wells at 3.4

MPa (500 psi). Considering that the rock porosity is only about 0.8%, the center part of the block was saturated.

Figure 3-4 provides the data recorded during the hydraulic fracturing phase and the consequent stepped constant flowrate (SCF) test. The initial injection rate was 1.0 ml/min. After about 140s of injection, breakdown occurred at a pressure of 27.4 MPa, and the injection pump was stopped at 14.5 seconds after the pressure breakdown. About two minutes later, injection resumed. The fracture reopening pressure was about 14.8 MPa, indicating a tensile strength of about 12.6 MPa (the difference in the breakdown pressure and the reopening pressure). The calculated tensile strength is about 2.0 MPa higher than the tensile strength of the Sierra White granite from the Brazilian test (10.68 MPa). The wellbore size effect could result in a higher breakdown pressure and thus a higher calculated tensile strength (Haimson and Zhao, 1991). As shown in the figure, most of the AE hits were recorded at breakdown, which indicates that fracture initiation and propagation lasted a very short time. This shows that the fracture initiation phase and the unstable fracture propagation phase are very close to each other. The brittle nature of the rock, use of water which easily penetrates micro-cracks and its low viscosity contribute to the rapid propagation of the fracture. A series of constant step-rate (SCF) injection tests was then carried out after the short-period injection. It is found that a higher injection pressure was needed to establish a higher injection rate, however, the pressure increment required to achieve it was smaller with increasing injection rates indicating further fracture opening. More discussion about the injectivity change during SCF is provided in section 3.3.

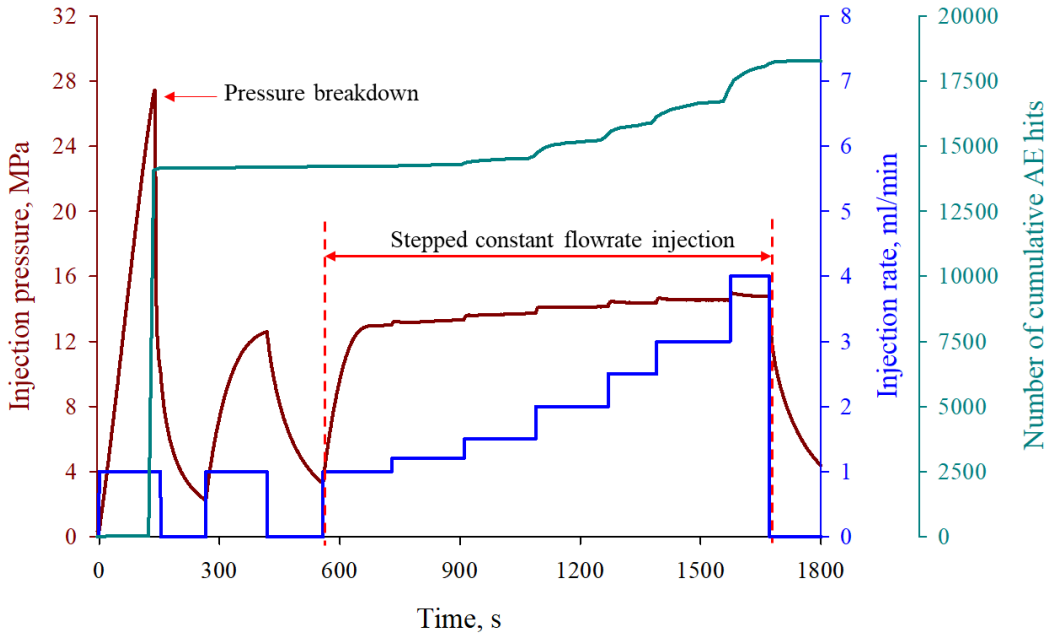


Figure 3-4. The recording data for test with higher stress level

At the beginning of the stimulation test, pressures in all wells were 0.34 MPa (50 psi) and all the production wells were closed. Figure 3-5 shows the pressure history in all the wells. Pressure in Well No.1 started to increase dramatically right after breakdown indicating that the fracture intersected Well No.1 during the first injection interval. The pressure in Well No.2 increased gradually initially. Meanwhile, Well No.3 and No.4 did not experience any noticeable pressure changes. When the pressure in Well No.1 and Well No.2 exceeded 2.1 MPa, the valves were opened to prevent further fracture extension in those wells or their close vicinity. From the pressure record, both wells have a good hydraulic connection with the injection well. However, the pressure trends in these wells indicate that Well No.1 has a much better hydraulic connection than that of Well No.2. After the test, we found that the induced fracture intersected Well No.1 and missed Well No.2 bypassing it (15.2 mm) below its bottom.

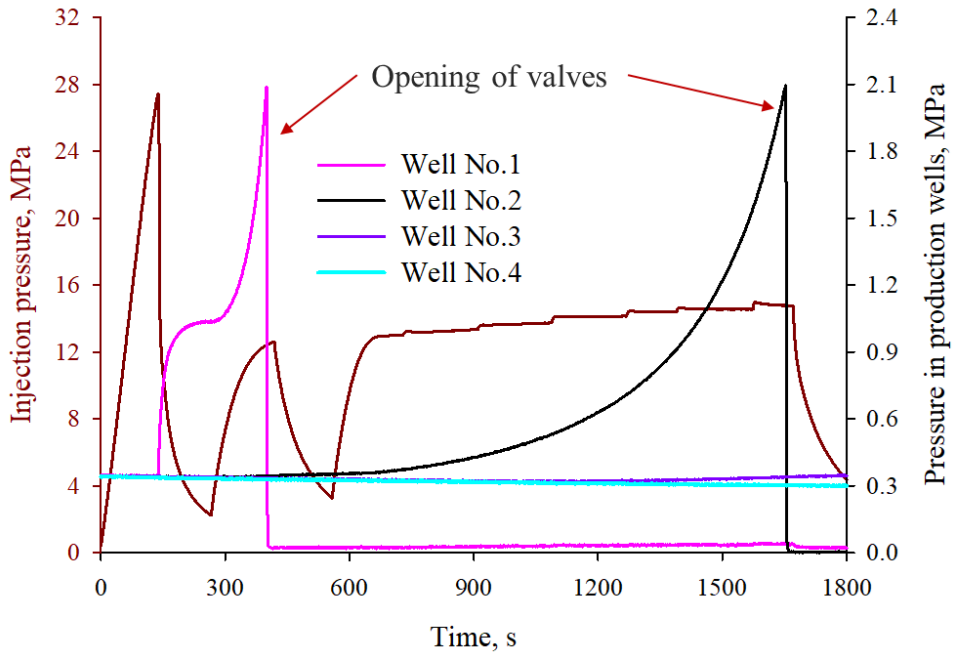


Figure 3-5. The pressure history in injection and production wells

The recorded waveform of the acoustic emission hits was analyzed with the AIC (Akaike Information Criterion) method (Akaike 1974) to pick the arrival time of the AE hits. This technique yields more accurate arrival times than the commonly-used fixed threshold method (Stoeckhert et al. 2015). The locations of the AE events were calculated based on the arrival time at multiple sensors by minimizing the time differences of the measured and theoretical arrival times. At least four sensors are needed to determine the AE location. For failure mechanism analysis using Moment tensor, at least six sensors are needed (Grosse and Ohstu, 2008). Therefore, the events which were detected by at least six sensors are analyzed. Nelder-Mead Downhill-Simplex algorithm was applied due to its fast and stable result (Stoeckhert et al. 2015).

The failure mechanism of the events was analyzed using the average polarity method (Zang et al., 1998). The polarity of an event is defined as the average polarity of all the first P-wave polarities following:

$$pol = \frac{1}{N}\sum_{i=1}^{N}\text{sign}(A_i) \tag{3.1}$$

where A_i is the first motion of the P-wave (i.e., the amplitude. in the field, it is the first point of the displacement when a MEQ is detected. Up is positive and down is negative.) received by the i*th* channel and N is the number of channels that received the event. For an event with *pol*-value of $-1 \le pol \le -0.25$, the event is classified as a tensile failure (T-type), *pol*-value of $-0.25 \le pol \le 0.25$ indicates a shear/mixed mode events (S-type) and a compressional event (C-type) is designated when $0.25 \le pol \le 1$. Average polarity method is a quick approach to determine the failure mechanism of an AE event compared with Moment tensor method. However, it cannot separate the shear and mixed model failure events.

The event locations and failure mechanisms were analyzed and the results are projected onto different block planes as shown Figure 3-6 and Figure 3-7. The unfilled large green/red circles and rectangles represent the open intervals of the wells. The color of the symbols indicates the time of the AE events, and the shape of the symbols shows the failure mechanism. Squares represent tensile failure (T-type), circles are for compressional failure (C-type) corresponding to implosion failure events, and diamonds stand for shear/mixed mode events (S-type). In Figure 3-6, one can follow the fracture propagation process by looking at the color time evolution of the AE events (dark blue for early stage and near the injection well and yellow for late stage near the edges). It only took the fracture about 1.4 seconds to reach the rock surface. Due to the very low viscosity of the fracturing fluid, it can

penetrate weak boundaries and micro-cracks in the mineral. During the fracturing phase, about 47% of the events were determined to be shear/mixed mode failure events, 28% percent were tensile failure events and 25% compressional failure events. It is somewhat unexpected that the number of shear/mixed model failure events exceeds that of tensile failure events. This could result from the fact that the induced fracture mainly cut through the grain boundaries, so that sliding would be more likely to occur (as is demonstrated with thin section and SEM observation discussed below). Since the induced fracture is not smooth, this local sliding and opening on the fracture surface will result in shear/mixed model events. Similar behavior was observed in Fredeburg Slate where the induced fracture propagated within a cleavage plane in the slate (Stoeckhert et al., 2015).

Figure 3-7 shows the location and failure mechanisms of the AE events during the SCF test. It is very interesting to observe that the events during the SCF test period are located where the fracture already exists. This observation indicates that the AE events during this stage were mainly caused by the width adjustment of the fracture which was due to the higher injection rate. There is no obvious trend for when the AE events happened, and they most likely occurred randomly on the existing fracture and off its plane. During the SCF test, more compressional failure events are observed and the percentage of tensile failure and shear/mixed mode failure is smaller. Since the induced fracture has a very small aperture, crushing, breaking, and sliding would happen during fracture opening. The test result shows that compared with the hydraulic fracturing phase, more crushing of the contact points on the fracture surface were observed during the SCF.

It can be seen from the AE event cloud that the fracture mainly propagated to the east and northeast direction and that that it is inclined having a lower elevation on the east side

causing it to miss Well No.2. It is found that that the AE cloud has a very good agreement with the 3D reconstructed fracture geometry shown in a later figure below.

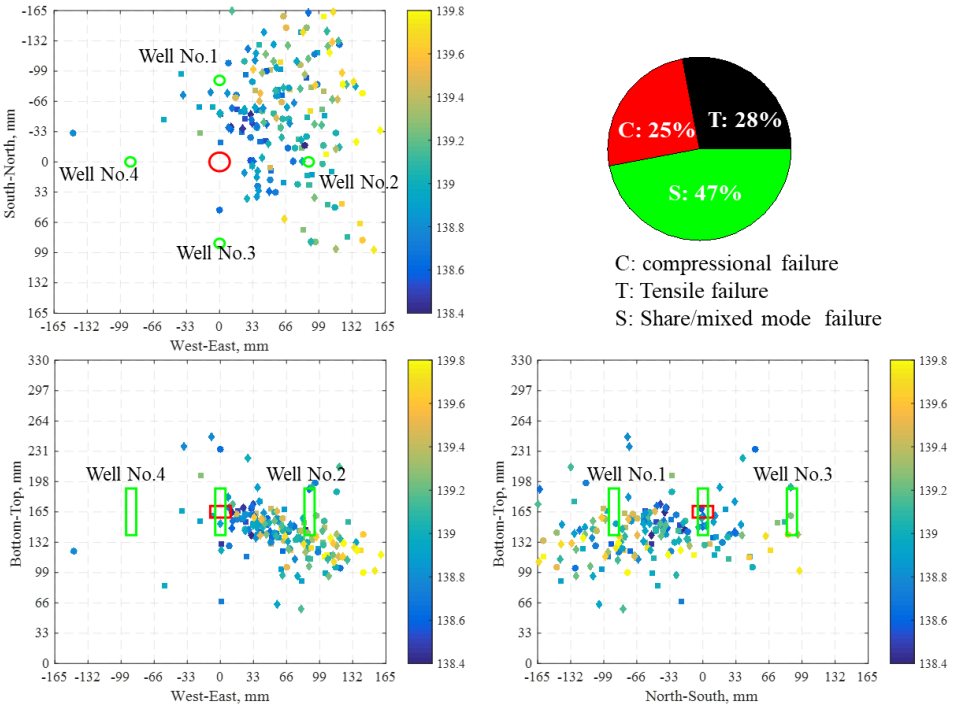


Figure 3-6. Acoustic emission analysis during fracturing test

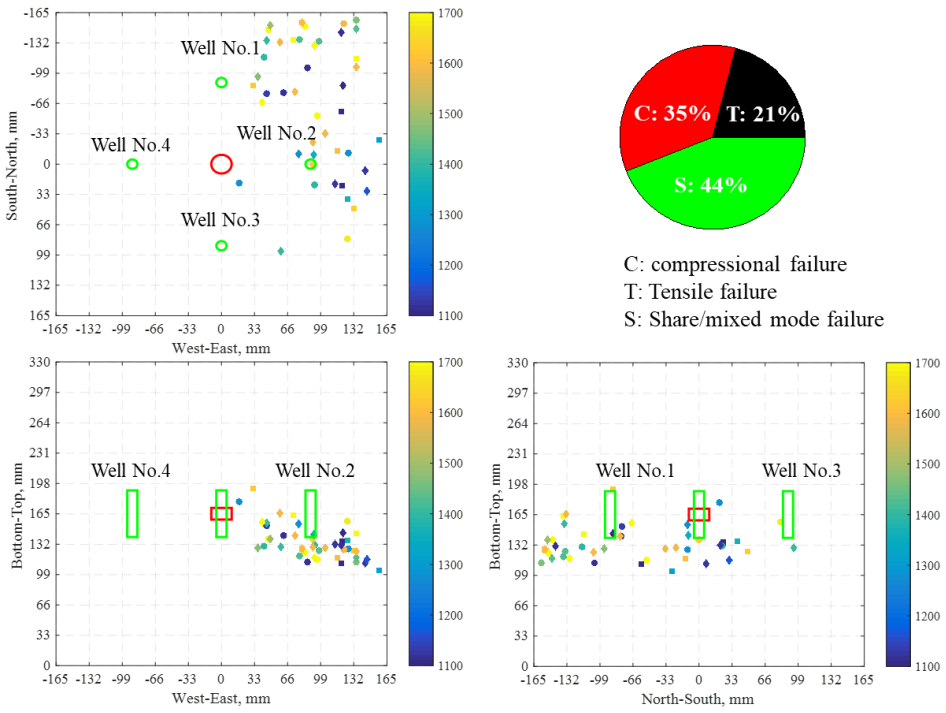


Figure 3-7. Acoustic emission analysis during SCF injection test

The located AE events and the reconstructed fracture geometry (the method to get the reconstructed fracture geometry will be discussed latter) is illustrated with a color map in Figure 3-8. The open intervals in the wells are represented with the blue cylinders in the figure. The color indicates the elevation of the fracture surface and the AE events z-coordinate (from both hydraulic fracturing test and SCF test). The AE cloud shape has a good agreement with the overall fracture geometry. The distribution of the location error of the AE events whose top-down projection are within the fracture area is shown in Figure 3-9. It is obvious that most of the located AEs are within 12.7 mm (0.5 inch) from the real fracture in Z direction. The reconstructed fracture shows that the induced fracture tilts to the East side and touches the North surface. The fracture area calculated with the fracture geometry is about 344.7 cm^2. The fracture inclination and unsymmetrical geometry is likely

the result of the rock heterogeneity and low viscosity of the fracturing fluid as well as asymmetric notch geometry.

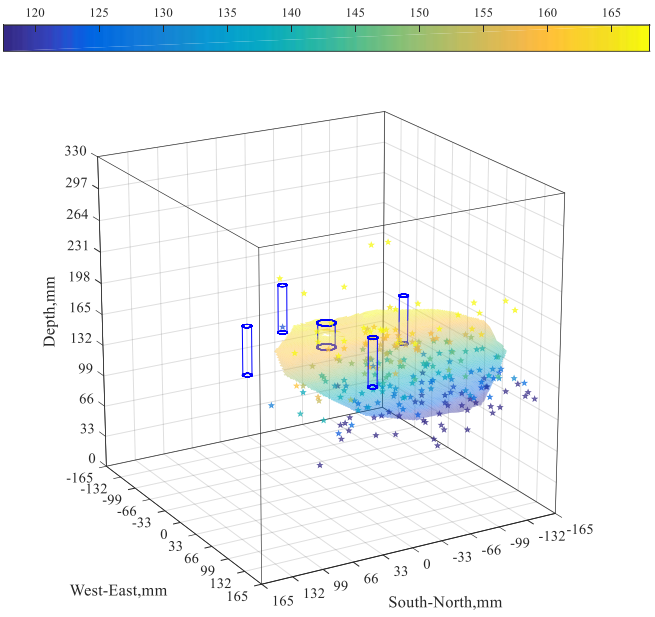


Figure 3-8. AE cloud and the reconstructed 3D fracture geometry.

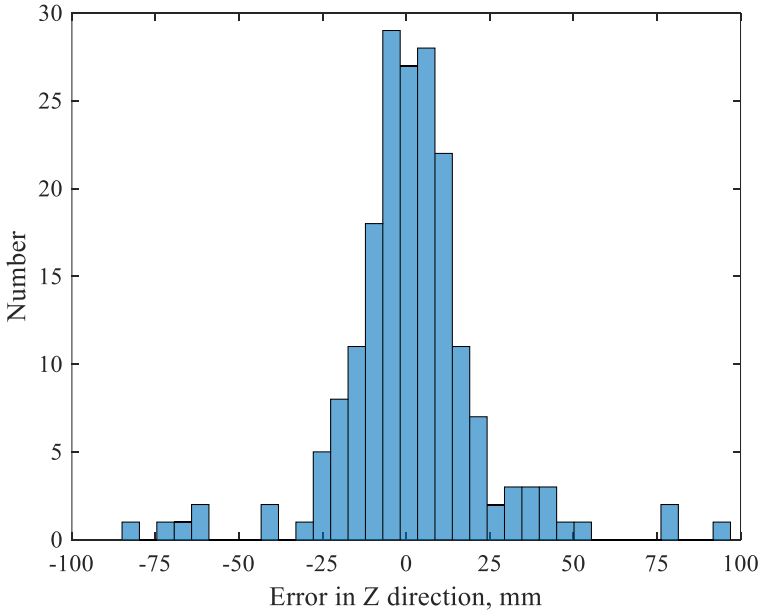


Figure 3-9. The distribution of location error in Z direction for events within the real fracture area

3.3 Injectivity of the Rock Matrix and the Induced Fracture

Before the fracturing test and with the inner part of the rock sample saturated, a stepped constant pressure test was conducted to investigate the injectivity of the rock matrix with the same stresses as the fracturing test (i.e. 6.9 MPa (1000psi) vertical stress, 10.3 MPa (1500 psi) minimum horizontal stress and 13.8 MPa (2000 psi) maximum horizontal stress). Figure 3-10 (left) shows the injection rate vs. injection pressure before hydraulic fracturing. The linear proportional relationship between the injection pressure and the injection rate demonstrates that no additional micro-cracks were generated and thus the rock has a constant permeability. Considering that the open interval of the injection well is much smaller than the test block, spherical flow is assumed. Then, under steady flow, the permeability of the rock matrix can be estimated with the following equation (Bear, 2013):

$$k = \frac{Q_r \mu \left(1/R_w - 1/R_e \right)}{4\pi \left(P_e - P_w \right)} \tag{3.2}$$

where k is the rock permeability, μ is the fluid viscosity, Q_r is volumetric flow rate, R_w and R_e are the equivalent radius of the injection interval and the rock block, respectively, P_e and P_w are the pressure at the boundary and the injection well and in our case P_e is zero. With the constant pressure and injection rate data (Figure 3-10, left side), the rock matrix permeability is estimated to be 494nD, which is very close to the value measured from a short disc sample.

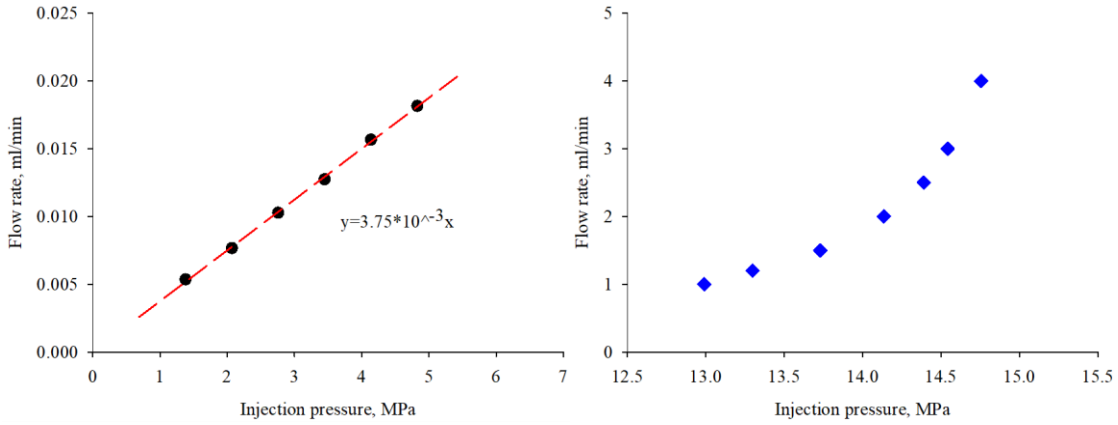


Figure 3-10. injectivity before (left) and after fracturing (right)

Figure 3-10 (right) provides injection rate vs. injection pressure during the SCF test after fracturing. Apparently, after stimulation, the injectivity of the granite block increased dramatically. It is interesting that the injection rate increased dramatically with small increment of the injection pressure (decreasing effective stress on the fracture). Under injection pressure of 14.75 MPa, the intact rock would have an injection rate of 0.05534 ml/min (the permeability is assumed to be same as measured) while the stimulated block has a much higher injection rate of 4 ml/min. The fluid impedance of the block dramatically decreased from 266.5 MPa/(ml/min) to 3.7 MPa/(ml/min). This could be explained by the fact that the normal stress has a much higher impact on the fracture aperture when the normal stress is small (Willis - Richards, Watanabe et al. 1996, Gao and Ghassemi, 2016; Cheng and Ghassemi, 2019), i.e., the hydraulic fracture acts as a "joint" during reopening with a non-linear stress-opening profile (Rutqvist and Stephansson, 2003, Rutqvist, et al, 2002; Goodman, 1976). Another possible explanation is the fracture did not just simply open along the direction perpendicular to the local fracture surface, and that a certain amount of sliding also occurred to result in a higher fracture opening. It is likely that there was no large fracture

propagation during the SCF test since no pressure drop was observed. However, some AE activities were recorded which may be explained by fracture opening as supported by the AE location analysis discussed above. It can be seen from Figure 3-4 that at the later stages of the SCF injection test, more AE events were detected compared to the early stages due to larger fracture opening.

3.4 Hydraulic Fracture Geometry and Its Surface Characterization

After the test, the granite block was cut into thin slabs and then a special florescent penetrant was applied to highlight the fracture trace on the cut surfaces. Based on all the fracture traces in the cut slabs, the 3D fracture geometry was reconstructed. Figure 3-11 (top) shows one of the slabs which cuts through the injection well, and Well No.1 and No.3 (the acoustic emission analysis from this block was discussed in Section 3.2.2). From this picture, it is clear that the induced fracture intersects Well No.1, while it is about 48.3 mm away from Well No.3. Figure 3-11 (bottom) is the slab with Well No.2 visible, as can be seen the induced fracture did not intersect the well but passed underneath it, which is also indicated by our AE analysis (Figure 3-6 or 3-7).

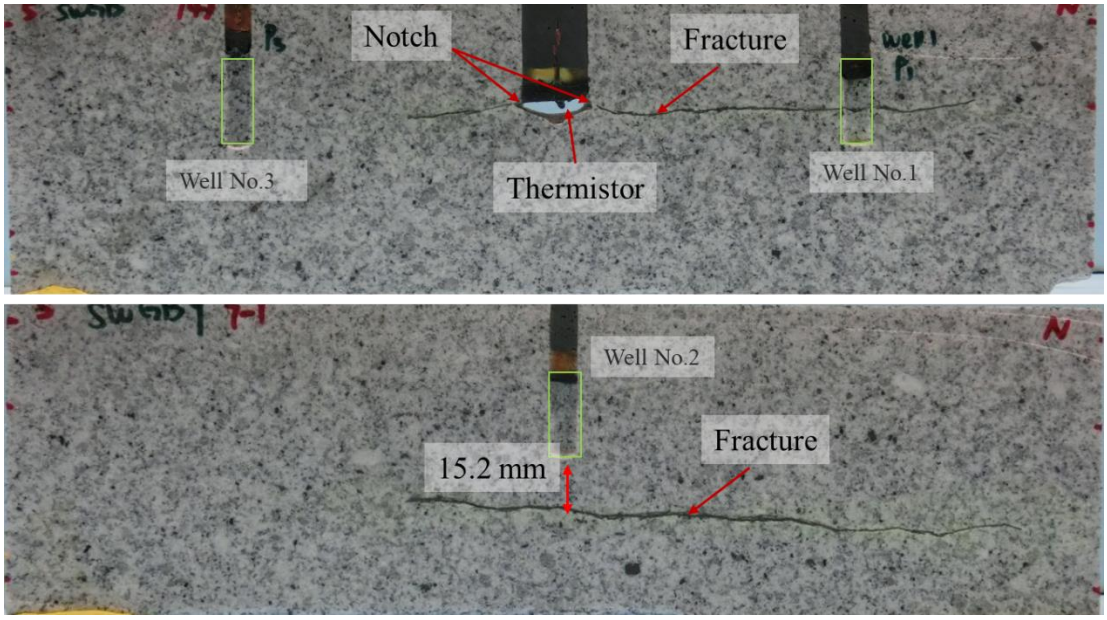


Figure 3-11. Fracture on slabs at the center (top) and at Well No.2 (bottom) from Sierra White granite block test.

The fracture surface characterization is very important to flow and heat transport through the fracture. The hydraulically induced fractures of the tested bocks were observed under different scales. The fracture surface profile was quantified with a laser scanner. The top two color maps (Figure 3-12) are the two typical fracture surface profiles from test block of Sierra White granite block, and it can be seen that the induced fracture has a rough surface. For comparison, the surface profile from a Brazilian test on a 25.4mm diameter Sierra White granite sample is also shown in Figure 3-12 (bottom). The Brazilian test induced and the hydraulically induced fractures have similar surface properties since they both are tensile fractures. As compression, the fracture surface profile obtained from Raven Noir gabbro is presented in Figure 3-13, in which figures (1) - (3) show the fracture profiles from the hydraulic fracturing while figure (4) shows the fracture profile induced by Brazilian test.

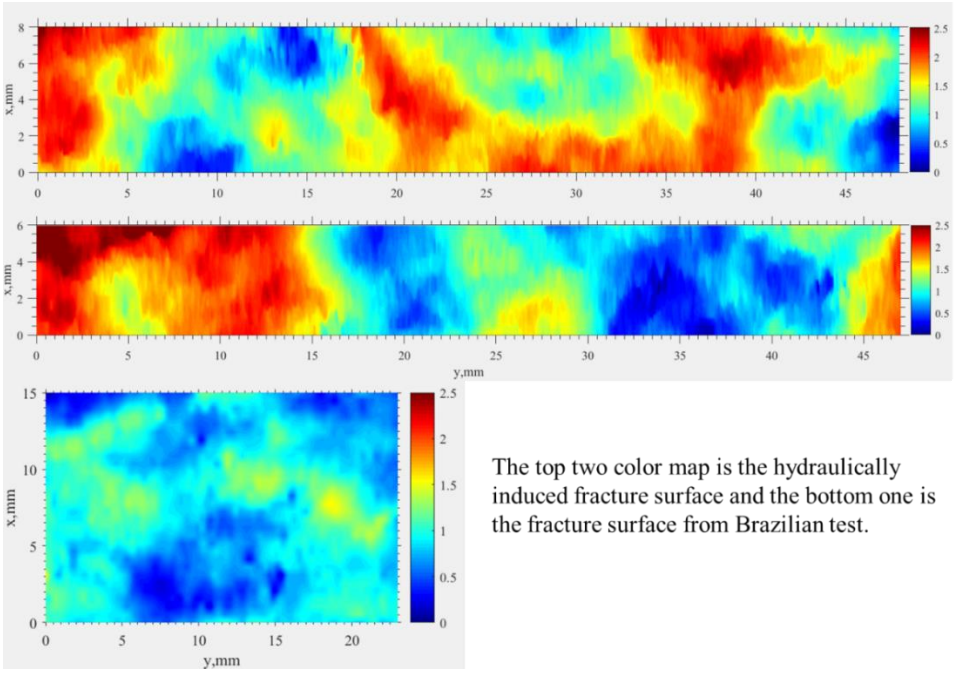


Figure 3-12. Fracture surface profiles obtained from laser scanning (Sierra White granite)

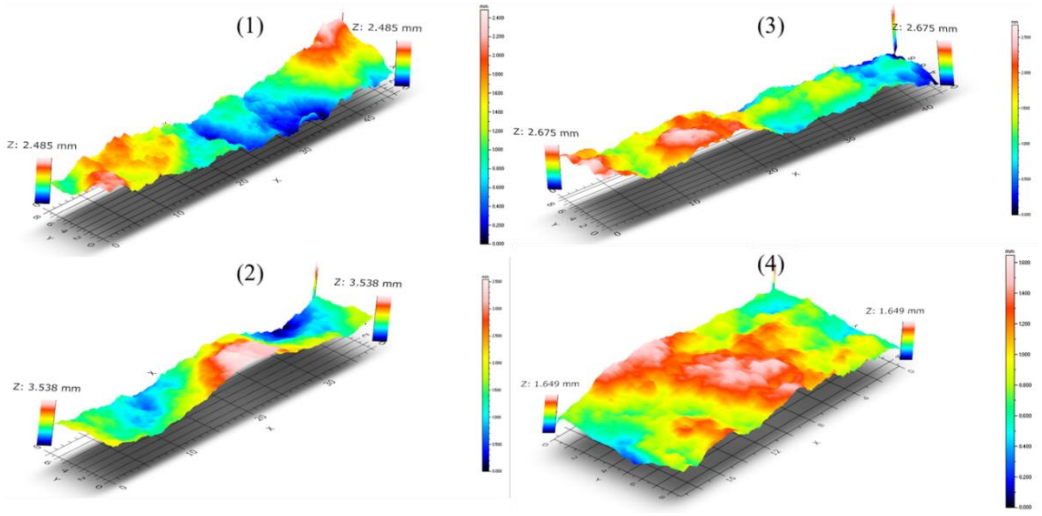


Figure 3-13. Fracture surface profiles obtained from laser scanning (Raven Noir gabbro)

The data from 3D scanning were used to estimate the surface roughness parameter, Z_2, using the first-derivative root-mean-square: (Tse and Cruden, 1979; Yu and Vayssade, 1991).:

$$Z_2 = \left(\frac{1}{(N-1)(\Delta s)^2} \sum_{i=1}^{N-1} (y_{i+1} - y_i)^2 \right)^{1/2} \tag{3.3a}$$

where $y, \Delta s, and\ N$ are the surface profile vector, spatial sampling interval, and number of data points, respectively. There are different correlations between Z_2 and the joint roughness coefficient (JRC) (Yu and Vayssade 1991; Alameda-Hernández et al. 2014) and they provide similar result. In this work, the following equation was applied to obtain the JRC from Z_2 with the sampling interval of 0.5mm (i.e., $\Delta s = 0.5mm$):

$$JRC = 61.79 * Z_2 - 3.47 \tag{3.3b}$$

The tortuosity is a parameter that defines the geometric complexity of a flow path. It will influence the fluid flow through the fracture. In the oil industry, tortuosity is the ratio of the length of a streamline between two points to the straight-line distance between those points. The tortuosity of the hydraulically induced fracture and Brazilian test induced fracture was also calculated and compared. Based on the digitalized fracture surface profile, the Z_2, JRC and the tortuosity of these two kinds of fracture profile were analyzed and are shown in Table 3.1.

Table 3.1. Surface parameters for Sierra White granite and Raven Noir gabbro

Rock	Fracture	Z_2	JRC	Tortuosity
Sierra White granite	Hydraulically induced	0.266	12.98	1.10
	Brazilian test induced	0.187	8.08	1.03
Raven Noir gabbro	Hydraulically induced	0.237	11.16	1.05
	Brazilian test induced	0.195	8.60	1.05

3.5 Thin Section and SEM Observation of the Fracture

Thin sections were prepared to obtain a closer view of the fracture path and its relationship with the rock texture. Figure 3-14 (left) is a thin section of Sierra White granite with a hydraulically induced fracture visible. The dark parts on the images are Quartz and the light parts are Albite. Some broken Quartz crystals are also visible on the images. The fracture mostly follows the weak boundary between the Quartz and Albite grains and at time cuts across the Albite grains. In some cases, branching (one fracture splits to two) and bridging (when a fracture is connected in a way that is not visible in the thin section) was observed in microscale; a similar observation was discussed by Gonzalez (1994). Whether the fracture will cross rock grains or propagate along the grain boundaries depends on the strength of the grains and the boundaries. SEM observation provides an even a closer observation of the fracture and the fracture width. One SEM image of the fracture is shown in Figure 3-14 (right), from which we also notice that the fracture mainly follows the grain boundaries and sometimes cuts the weaker grains along cleavage (see the one on the northeast corner of the picture). The fracture width measured from the SEM observation is about 17 μm.

As comparison the thin section and SEM observation of the hydraulically induced fracture from Raven is shown in Figure 3-15. It shows that fracture induced in Raven Noir crosses the mineral grains. It indicates that the grain boundary in Raven Noir gabbro has similar strength as the grains. As a result, the induced fracture from Raven Noir should has a smaller tortuosity on the micro-scale compared with the fracture in Sierra White granite. It is also found the fracture width was smaller in the Raven Noir gabbro with average value around 7.6 μm.

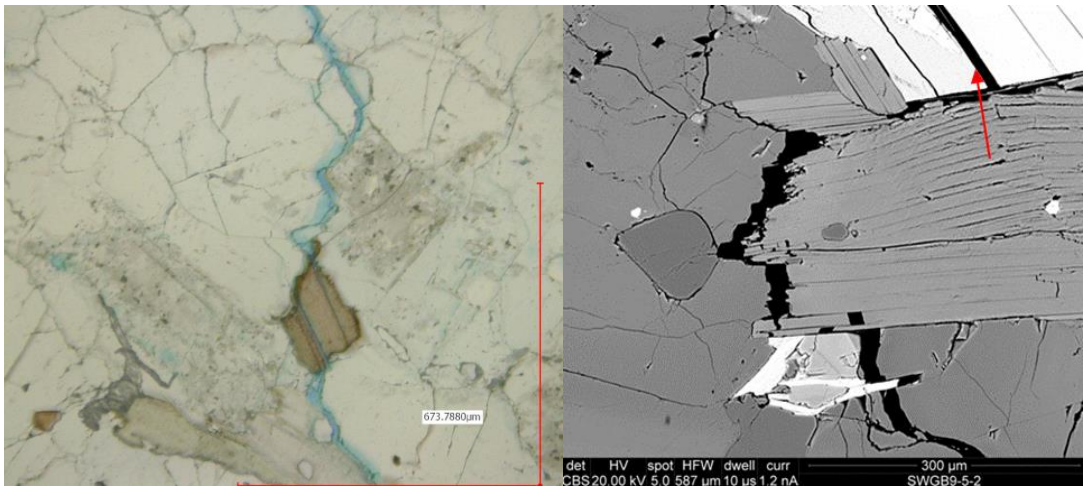


Figure 3-14. Thin section (left) and SEM (right) observation (Sierra White granite)

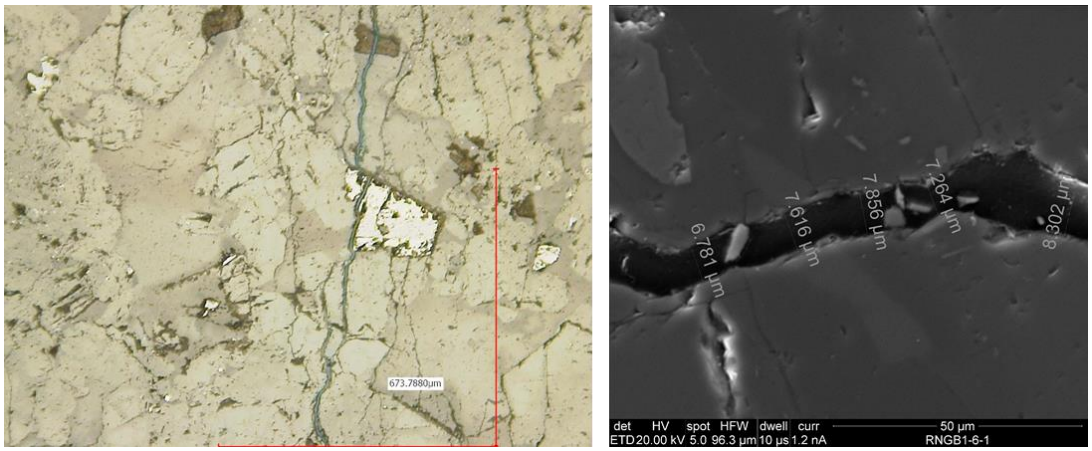


Figure 3-15. Thin section (left) and SEM (right) observation (Raven Noir gabbro)

3.6 Summary and Conclusions

A series of advanced lab-scale tests was carried out to investigate reservoir stimulation for enhanced or engineered geothermal systems (EGS). In this Chapter, the focus is the acoustic emission during reservoir stimulation and fracture characterization. The AE cloud and its evolution reflects the fracture propagation path as also ascertained by observation well pressure monitoring. The hydraulically induced fracture propagates very fast particularly

since low viscosity water was used as the fracturing fluid. Analysis of focal mechanisms indicates that the percentage of compressional failure events was 10 percent more in the SCF test than in the hydraulic fracturing test. Also, the percentage of tensile failure and shear failure decreases during the SCF test compared with the hydraulic fracturing phase due to the reopening of the fracture. This is because during the SCF test, the fracture aperture was changing based on the injection rate and so relatively more crushing occurs during this stage. The flow impedance of the intact block improved about 72 times after simulation. The reconstructed 3D real fracture shows a good agreement with the AE monitoring result, which proves the feasibility of MEQ (field scale of acoustic emission) application in EGS. Fracture surface profile was obtained with laser scanning, and its analysis shows that the hydraulically induced fracture has a rough surface with a joint roughness coefficient (JRC) of 12.98 and tortuosity of 1.10, both of which are similar to the fracture from the Brazilian test. The thin section and SEM observation shows that the fracture follows the weak boundary between the Quartz and Albite grains. For Raven Noir gabbro, the thin section and SEM shows that the that induced fracture crosses the mineral grains and smaller fracture width was obtained, the thin section observation indicates that the fracture in Raven Noir gabbro should has smaller tortuosity and JRC value, which agrees with the fracture laser scan profile: the induced fracture has a rough surface with JRC of 11.16 and tortuosity of 1.05.

4. Self-Potential Response in Lab-scale EGS Simulation

4.1 Electrokinetic Phenomena

There are several coupled electrical phenomena that are potentially involved in SP method, and Table 4.1 lists the commonly accepted ones (Mitchell, 1976; Corwin and Hoover, 1979; Moore, 2007a). In these coupled phenomena, a primary process drives a secondary electrical current. For example, water flow under a pressure gradient generates an electrical current via electrokinetic coupling. In this work, we not only investigate the electrokinetic coupling in a geothermal system but also discuss the influence of other two mechanisms (electrochemical coupling and thermoelectric coupling) on the total potential using experimental data.

Table 4.1. Phenomena involved in self-potential method

Primary driving gradient	Secondary current	Coupling mechanism	Coupled process name
Fluid pressure	Electrical	Electrokinetic	Streaming potential
Ion concentration	Electrical	Electrochemical	Diffusion potential
Temperature gradient	Electrical	Thermoelectric	Ludwig-Soret effect

The electrokinetic phenomenon arises from the existence of an electric double layer at the solid/liquid interface. The commonly accepted double layer model is the Stern model (Ishido and Mizutani, 1981; Morgan et al., 1989). It consists of a layer of ions adsorbed on the surface of the solid phase and a diffuse mobile layer extending into the liquid phase. When at rest (static conditions), the double layer as a whole is electrically neutral, while under a pressure gradient, the non-fixed charges move away from the solid surface with the pore fluid resulting in a charge imbalance and thus an electric field. Detailed information about

the Stern model and electrokinetic phenomena can be found in (Ishido and Mizutani, 1981; Morgan et al., 1989, Moore et al., 2007a).

In the absence of external current sources and under steady state equilibrium conditions, the governing equations for the linear transport of fluid and current in porous medium lead to the Helmoltz- Smoluchowski equation (Dukhin and Deriaguine, 1974):

$$Cc = \frac{\Delta\varphi}{\Delta p} = \frac{\varepsilon\zeta}{\eta\sigma_f}\frac{F}{F_o} \tag{4.1}$$

where $Cc, \varphi, p, \varepsilon, \zeta, \eta, F, F_o \text{ and } \sigma_f$ are streaming potential coefficient, electric potential, fluid pressure, absolute dielectric constant of the fluid, zeta potential (defined as the potential at the slip plane on which shearing occurs within the fluid), dynamic fluid viscosity, formation factor for the current sample conditions, formation factor with a very high fluid conductivity when surface conduction is absent, and fluid conductivity, respectively.

SP measurements during hydraulic fracturing and circulation phases were carried out under different boundary conditions. Different test conditions reflect attempts to fine-tune the testing procedure and to provide the best data for various phases of the experiments. In this section, the SP results under different conditions will be provided and discussed. The test conditions related to SP measurement will be described for each individual test in this section.

4.2 Influence of Saturation Condition and Different Boundary Conditions

The tests were carried out on 33.0 cm cubic rock blocks with wellbore layout descried in Section 2, with a 5.1 cm and 12.7 cm open interval in the injection and production wells. Ideally, a test should be performed on a fully saturated and electrically insulated block. A

1.27 cm thick square non-conductive PEEK plate of length of 31.75 cm was placed directly on each side of the rock block to insulate it from the surrounding cell/frame components. The hydraulic fracturing test was conducted without fluid in the loading frame under stress conditions of 3.45 MPa vertical stress, 6.89 MPa minimum horizontal stress and 10.34 MPa maximum horizontal stress. The inner part of the block was saturated by maintaining the pressure in the injection and production wells at 1.72 MPa and 0.69MPa, respectively over forty hours. During this period, about 186 ml 0.002 mole/L NaCl was injected before the stimulation. It is reasonable to assume that the inner part of the rock was fully saturated since the total pore volume of the block is about 288 ml (calculated from its porosity).

The injection pressure, flowrate, and the SP response during the stimulation test are shown in Figure 4-1 for different wells. The data are split in two intervals and shown in Figure 4-1 (for 0-1100s and Figure 4-2 for 1100-2000s). The hydraulic fracturing phase was conducted to ensure that the induced fracture remains within the rock block. NaCl solution (0.002 mole/L) was injected at a constant rate of 2.0 ml/min. The injection pump was programmed to go into backflow (a flowrate of 100 ml/min) mode or to reduce the injection rate when the injection pressure drop between two consecutive data points (recorded every 0.5 second) exceeded a preset value of 0.28 MPa. During the backflow operation, the flowrate is negative and the injection pressure immediately drops to a negative value. The data from this period of backflow is excluded from the plots in Figure 4-1. During the first, second and forth injection cycles, the pump did backflow (marked by red arrows in the Figure 4-1) and it stopped pumping during the third cycle when the pressure drop exceeded 0.28 MPa. After each backflow operation, the pressure in the injection well was increased from a negative value back to 0.14 MPa before further injection (in Figure 4-1, data from these operations is

not plotted). At the beginning of the fracturing test, all production wells were closed and kept at 0.14 MPa. When injecting to create a hydraulic fracture, the wells were shut in and the pressures were monitored. If the pressure in a well exceeded 3.45 MPa, the valve for the well was opened to the atmosphere. The pressure history of all the wells is shown in Figure 4-3 and the pressure behavior in the production wells indicates that Well No.2 and Well No.3 were intersected by the hydraulic fracture after the third injection cycle.

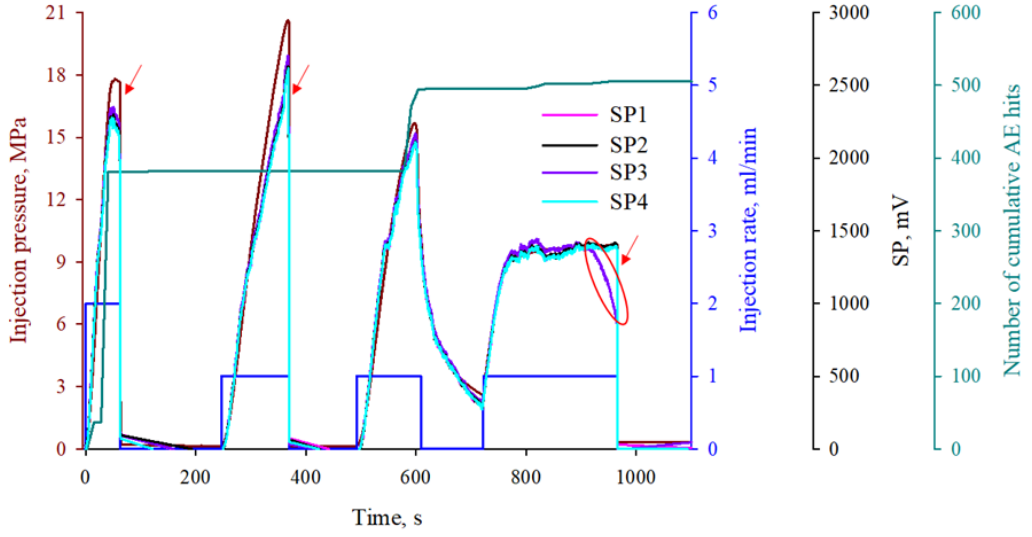


Figure 4-1. Recorded data during hydraulic fracturing of SWG block for time interval: 0-1100s (red arrows indicate the application of backflow operation and the red ellipses highlight the abnormal SP response in Well No.3 due to fracture intersection).

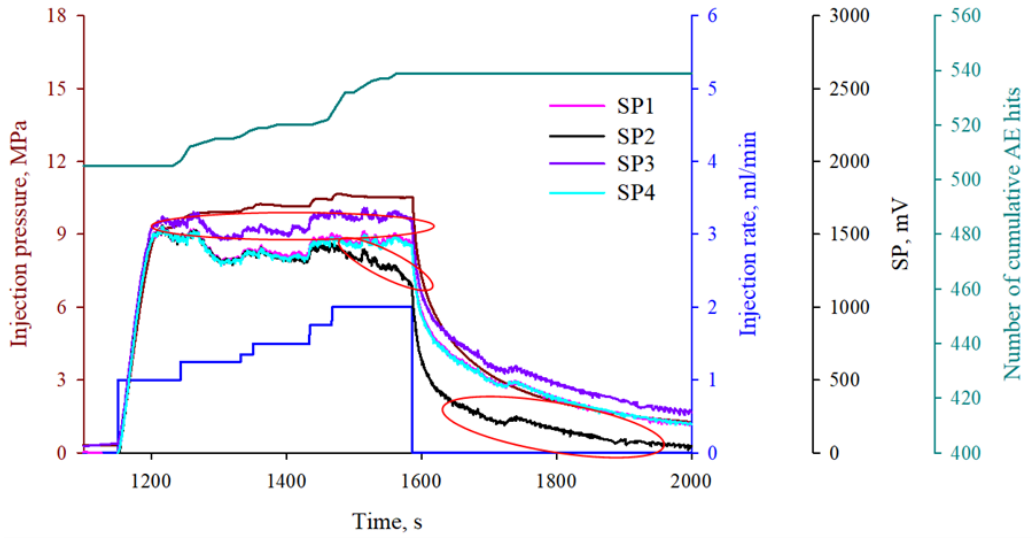


Figure 4-2. Recorded data during hydraulic fracturing of SWG block for time interval: 1100-2000 s (red ellipses mark the abnormal SP response due to fracture intersection: Well No.2 and No.3 were intersected by the induced hydraulic fracture).

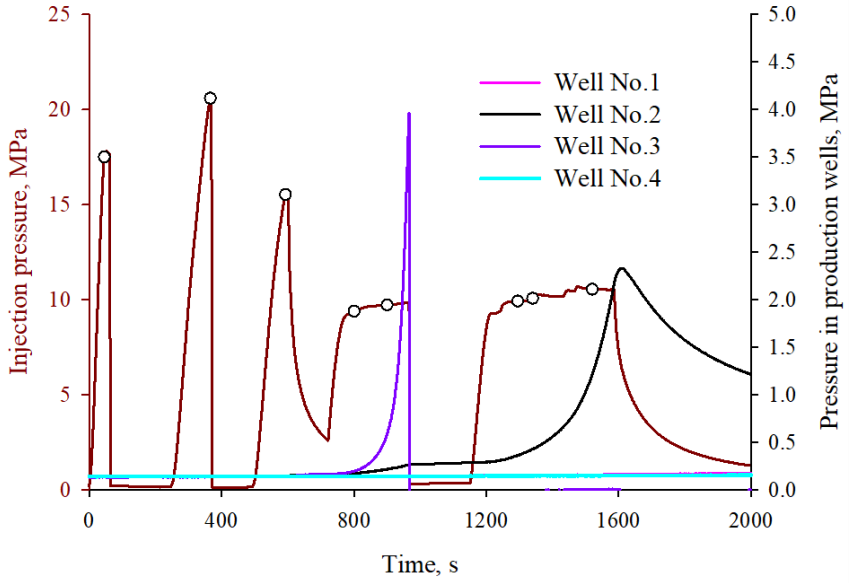


Figure 4-3. Injection pressure and pressure in production wells during hydraulic fracturing (the circles correspond to the selected representative points used to investigate the coupling coefficient evolution).

The SP response (Figure 4-1 and Figure 4-2) indicates that Well No.2 and Well No.3 were intersected by the induced fracture. There is an apparent difference in the SP response of different production wells during the last period of injection. SP1 and SP4 overlap each

other, however, SP3 is higher. This is because the magnitude of effective streaming potential coefficient from the injection well to Well No.3 is higher due to the presence of the hydraulic fracture (note that Well No.3 valve is open and the pressure in Well No.1 and Well No.4 is close to 0 MPa, so the pressure difference was almost the same in these three wells). In Well No.2, the pressure increased due to the hydraulic fracture, so the SP2 is the lowest even through the coupling coefficient increased in this direction.

The evolution of the coupling coefficient during the test with injection rate and AE hits is plotted in Figure 4-4 with several representative points shown in Figure 4-3 on the pressure curve. The magnitude of effective streaming potential coefficient for all the measured directions experienced an increase (9.7% for Well No.1; 10.56% for Well No.2; 17.73% for Well No.3; 8.98% for Well No.4) at the end of the test compared to the first points. Moreover, the increments correlate with the hydraulic connection in these directions very well: the induced fracture intersects Well No.2 and No.3. Well No.3 has a steeper pressure increase trend meaning a better hydraulic connection with the injection well. This increase of effective streaming potential coefficient is due to the increased permeability at higher pore pressure in response to dilatancy (microcracks) and creation of new fractures and increase in the created fracture aperture (Moore et al, 2007a; Ishido and Mizutani, 1981). There are two obvious decreases of the coupling coefficient in all measured directions and they all occur after the backflow operation. This is due to the air bubbles generated during the backflow process.

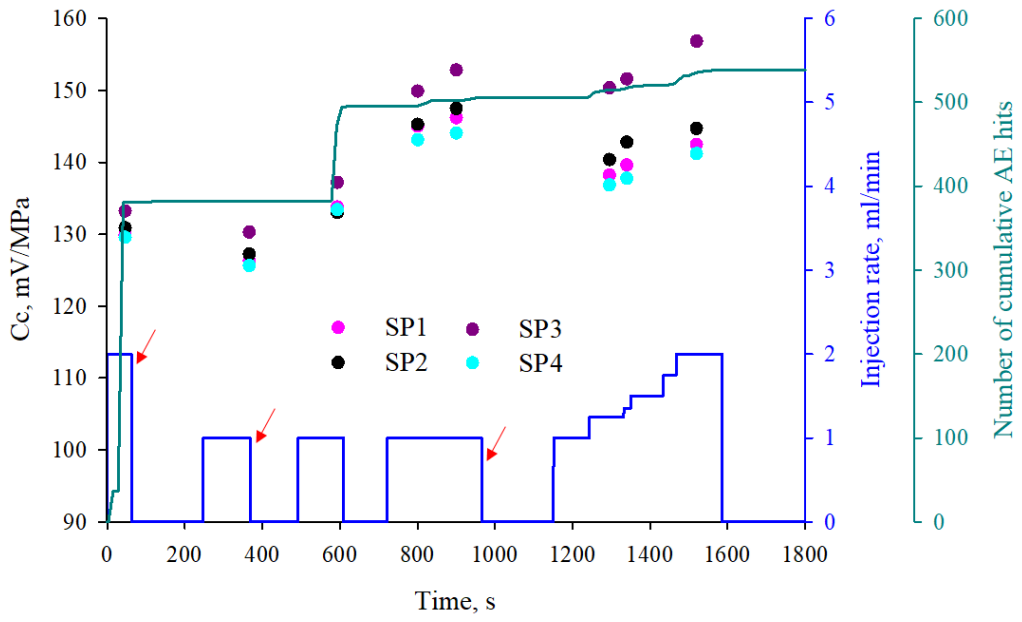


Figure 4-4. Evolution of the streaming potential coefficient for different directions during hydraulic fracturing (red arrows indicate the application of backflow operation).

The streaming potential coefficient at a pressure less than 2.0 MPa obtained by Moore is -200 mV/MPa for the same type of rock with 0.001 Mole/L NaCl solution. The value obtained from this test (the average value from four measured directions prior to the end of the first injection cycle in Figure 4-4) is -130.5 mV/MPa. The difference can be the result of different fluid concentrations, matrix saturations, and the rock heterogeneity causing different blocks to have different textural characteristics. Moreover, it is found that the amount of NaCl solution injected to saturate the inner part of the block before fracturing impacts the calculated coupling coefficient. In one test (discussed in Hu et al, 2017a), the fluid injected before fracturing is about 20ml and the coupling coefficient is -76.9 mV/MPa before fracturing and -143.6 mV/MPa after fracturing. When the rock saturation is lower, under the same pressure gradient, there is less movable fluid resulting in a lower SP response and thus

a smaller coupling coefficient. The electrical boundary conditions also influence the recorded SP response.

In contrast to dry tests (no fluid in the loading frame), a couple of hydraulic fracturing tests were conducted with saturated blocks (see Hu et al., 2016 for more details) and with fluid in the loading frame. The SP sensors were put on the block surfaces while the reference sensor was placed in the injection well. Before the test, the rock sample was saturated with 0.002mol/L NaCl solution. When hydraulic fracturing test was conducted in saturated rock blocks with a pore pressure of 2.1 MPa, the frame was full of 0.002 mol/L NaCl solution. To lower the electrical noise for better acoustic emission monitoring, the frame was electrically grounded to earth. The recorded SP response had a much smaller amplitude and the calculated coupling coefficient was only -13.1 mV/MPa at a low injection pressure. However, an increase of coupling coefficient after fracturing was observed in all tests despite variable test conditions.

4.3 Influence of Temperature on SP Response

Influence of the temperature gradient on the SP response was investigated by examining the SP response during circulation tests, where cold water was injected into the center well and produced from the production wells. The cool injected water generated a temperature gradient in the initially uniformly heated block especially around the induced fracture. Here an example of SP response during circulation is shown in Figure 4-5. After the fracturing stage was completed, the granite block was heated to a uniform temperature of 69^{o}C with 0.002mole/L NaCl solution inside the loading frame. Then, cold 0.002 mole/L NaCl solution

was injected into the injection well. To prevent further fracture propagation during circulation, the injection rate was increased step by step while monitoring AE. During the whole period of the circulation test, the production wells were fully open to maximize the fluid production. At the beginning, the injection pressure increased to a peak value of about 20.7 MPa with an injection rate of 2 ml/min. The high pressure and the subsequent pressure drop indicate possible partial healing of the hydraulic fracture during the heating process (under stress). Subsequently, the pressure continued to decrease even while increasing the injection rate. This can be attributed to the cooling effect of the matrix around the fracture and possibly localized fracture propagation. At the end of the circulation phase, the injection rate was 25 ml/min and the injection pressure was about 6.34 MPa. During the entire circulation test (about 2 hours and 15 minutes), less than 80 AE hits were recorded, and no pressure drops were detected, indicating no apparent fracture propagation. The small oscillations in the injection pressure profile were due to switching between injection pumps. Apparently after the injection pressure peak, the value of Cc increased due to the fracture opening; and also the SP in Well No.3 and No.4 was higher since the induced fracture intersected these two wells.

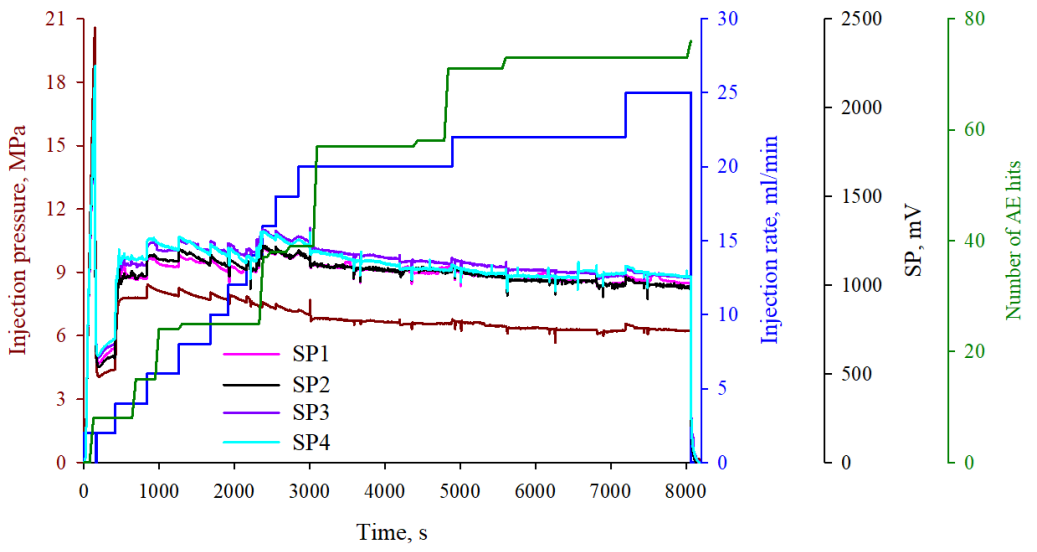


Figure 4-5. Streaming potential signals during circulation test.

To investigate the influence of temperature, we consider the change of Cc during the circulation history. Figure 4-6 shows the temperature in the wells and the injection rate information during the circulation test. The temperature at the bottom of the injection well decreased with continued injection and at higher injection rates, while the temperature change in the production wells was very small before t=1400s (there are two reasons for this: when the injection rate was low, the injected water was heated up to the block temperature before it reached the bottom of the injection well, and the cooling front had not yet reached the production wells). After a long time of circulation (about 2 hours and 15 minutes), the well temperatures were: injection well: 16.9^{o}C; Well No.1: 64.6^{o}C; Well No.2: 64.2^{o}C; Well No.3: 45.3^{o}C; Well No.4: 59.0^{o}C. Focusing on the apparent Cc between the injection well and Well No.1 (since it has the maximum temperature gradient), the Cc is calculated using the injection pressure and the recorded SP in Well No.1 at different times (all the investigated points were marked with circles in Figure 4-6). The calculated Cc, the temperature at the

injection well, the number of recorded AE, and the injection rate are plotted in Figure 4-7. It is found that the Cc is not influenced by the temperature gradient between the injection well and Well No.1 since Cc remains relatively constant for different temperature gradients. We notice that there is a step jump in Cc and this is due to the slight fracture propagation which is also indicated by the jump in the number of AE hits. It also needs to be clarified that the increase in the recorded AE does not necessarily mean fracture propagation it also could result from the opening of existing fracture.

The temperature impact on the recorded SP could be considered through the thermoelectric effect (the third coupling mechanism listed in Table 1). Due to the differential thermal diffusion of ions in the pore fluid and of electrons and donor ions in the rock matrix, a potential is created under temperature gradient. Similar to the electrokinetic phenomena, there is a linear relationship between the temperature difference and the potential deference with the coefficient known as thermoelectric coupling coefficient (Onsager, 1931; Darnet et al., 2004). Unlike the streaming potential coefficient, thermoelectric coupling coefficient is usually much smaller. The measured value of the thermoelectric coupling coefficient reported in the literature is in the range of 0.02-1.5 mV/^{o}C (Fitterman and Corwin, 1982; Leinov et al., 2010) and it depends on the salinity of the pore fluid. Leinov et al., 2010 reported the coupling coefficient range from 0.370 mV/^{o}C at extremely low salinity (1×10^{-4} M), to 0.055 mV/^{o}C at high salinity (1 M) for intact sandstone samples saturated with NaCl brine. The small thermoelectric coupling coefficient, especially for a high salinity fluid, could explain why the temperature gradient has negligible impact on the overall recorded potential.

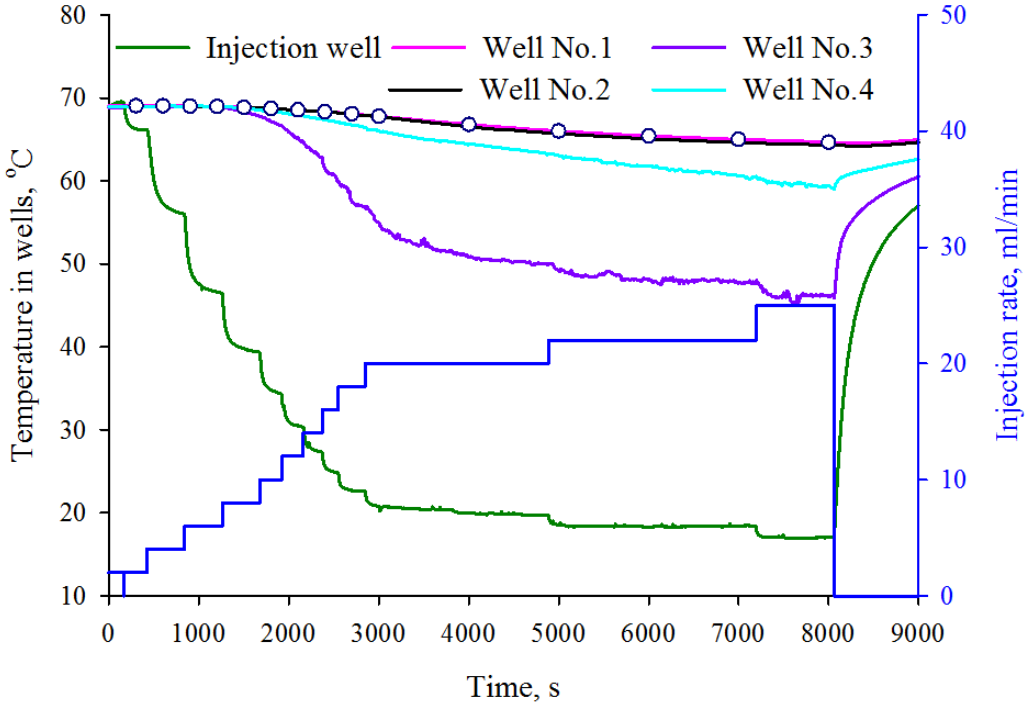


Figure 4-6. Injection rate and temperature history during circulation test.

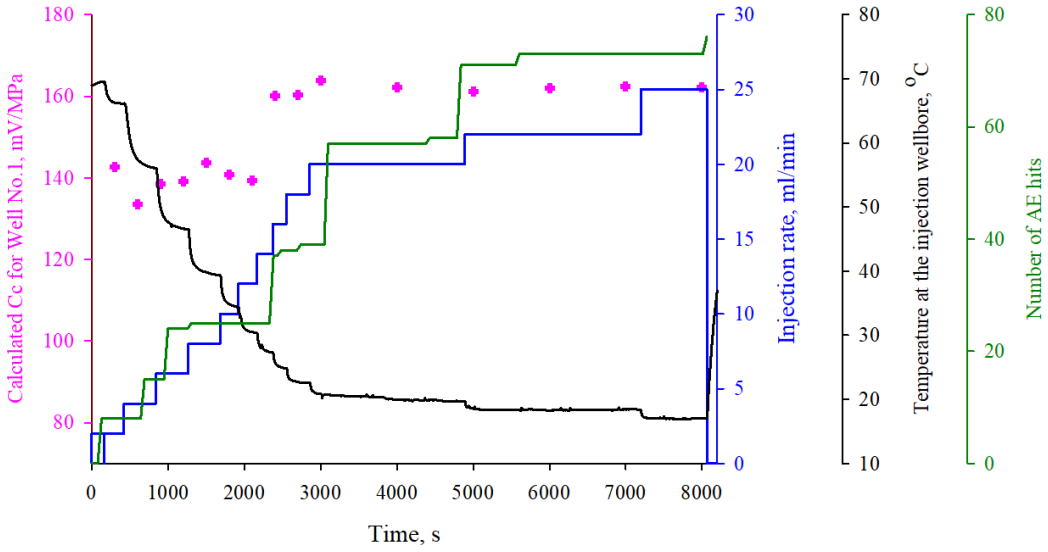


Figure 4-7. Influence of temperature on SP with Cc1 from Well No.1.

4.4 Influence of Fluid Concentration on SP Response

Influence of the fluid concentration gradient on the SP response was investigated by examining the SP response during the tracer tests. The tracer test consisted of two injection

phases as shown in Figure 4-8: during Phase #1, the injected solution was 1 mole/L NaCl (around 500 times higher than pore fluid) and in Phase #2 the injected solution was 0.002 mole/L NaCl. The injection rate was 1 ml/min. The SP response is different than what was observed during stimulation: the SP mimicked the injection pressure behavior only during the early injection phase (this is because the initial fluid in the pipe and wellbore bottom was 0.002 mole/L NaCl solution, i.e., the same as in the pores). After the high concentration fluid reached the bottom of the injection well and flowed into the fracture, a high concentration gradient developed between the injection well and production wells. As a result, the SP due to electrokinetic coupling was modified by the SP due to the electrochemical coupling and more important reduced coupling coefficient by the high concentration fluid (Ishido and Pritchett, 2011; Jouniaux and Ishido, 2012) causing a large SP drop seen in Figure 4-8. (Ishido and Pritchett, 2011) analyzed the effect of diffusion potential (the second mechanism listed in Table.1) on the SP in geothermal areas and concluded that the diffusion potential would not play an important role in the production-induced SP anomalies. For example, the diffusion potential for NaCl solution at room temperature could be estimated as: $\Delta\varphi \approx 12.3 \times \log(C_2/C_1)\, mV$ with salinity of C_2 and C_1 at the two measurement points. In our case, the diffusion potential is about 33mV which is minor compared to the streaming potential. Observed salt concentration influence in our case can be explained by salt concentration dependency of Cc. For example, (Jouniaux and Ishido, 2012) reported a regression relationship between the streaming potential coefficient and the fluid conductivity as: $Cc \approx -1.2 \times 10^{-8} \sigma_f^{-1}$. Later, when the fluid concentration difference was flushed out by the low concentration NaCl solution, the SP response was dominated by the pressure gradient and it more closely followed the injection pressure profile. This test result shows

that the fluid concentration (salinity) will have a great influence on the SP response if the difference is large. In this block test, only Well No.4 was intersected by the induced fracture, so the amount of high concentration NaCl solution penetrated into the fracture was not the same in every direction resulting in different SP response in different directions (SP4 shows a rapid decrease at the early stage).

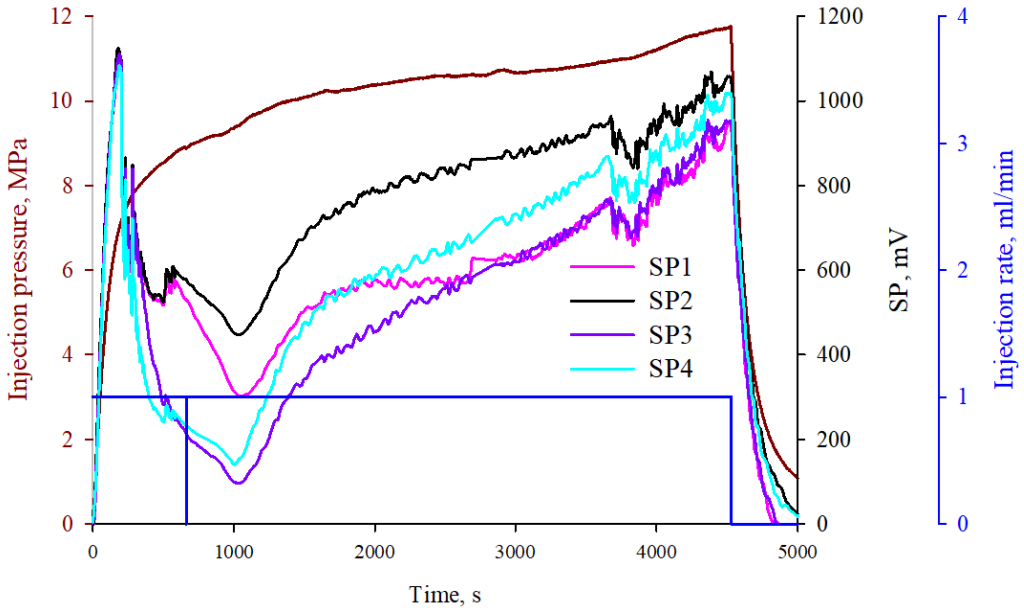


Figure 4-8. Streaming potential signals for different intervals during tracer test.

4.5 Results from a Test on a Rock with Zero-porosity

All the tests discussed above were conducted on Sierra White granite (SWG) blocks. Same tests were also conducted on Raven Noir black gabbro (RNG). As shown in Table 2.2, Raven Noir gabbro is almost non-porous, so it is very difficult to saturate. The pressure in the injection well was kept at 3.45 MPa for over 18 hours, and only about 0.4 ml 0.002 mole/L NaCl could be injected before the fracturing phase. The hydraulic fracturing test was conducted at room temperature and the initial injection rate was 0.5 ml/min with 6.89 MPa

vertical stress, 10.34 MPa minimum horizontal stress and 13.79 MPa maximum horizontal stress.

Figure 4-9 shows the recorded data from the fracturing test. Due to the unsaturated inner part of the block, the SP response in this case is different compared with that from obtained from Sierra White granite blocks (refer to Hu, et al 2018b for more details). The amplitude of the SP and the streaming potential coefficient are both much smaller. However, at breakdown, a sudden SP increase in all production wells was observed, which could indicate that all production wells were intersected by the induced hydraulic fracture.

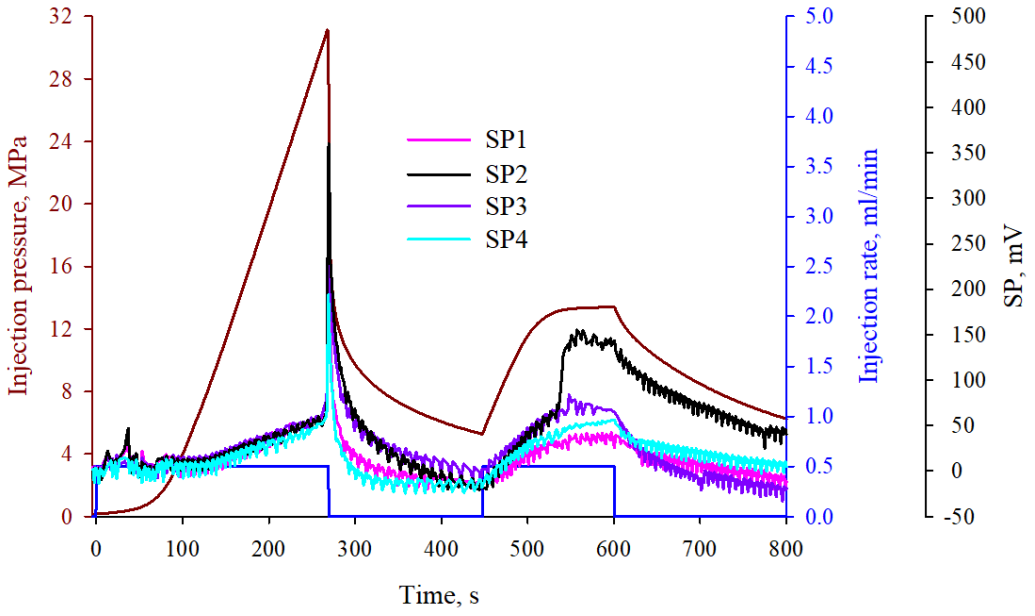


Figure 4-9. Streaming potential signals during fracturing of a RNG block.

4.6 Summary and Conclusions

Self-Potential (SP) response in lab-scale EGS tests was recorded and analyzed. Excellent correlation between the pressure drop and the recorded SP during fracturing and circulating

phases indicates that the SP response was mainly controlled by electrokinetic coupling. The liquid saturation influences the recorded SP response so that rock at a lower saturation would yield a smaller apparent coupling coefficient as there is less movable fluid under pressure. Under ideal test conditions, the measured streaming potential coefficient is -130.5 mV/MPa for an intact Sierra White granite block saturated with 0.002 Mole/L NaCl. The obtained value in this research is similar to that reported by Moore (-200 mV/MPa) for the same rock using a 0.001 Mole/L NaCl solution. Our results indicate thermoelectric coupling to have a negligible impact on the SP. This observation is in agreement with field records and numerical modeling by other investigators. The reason is the relatively small thermoelectric coupling coefficient under field salinity conditions. Unlike the temperature gradient, fluid concentration (salinity) has a great influence on the SP response when the concentration contrast between the injection fluid and the pore fluid is large. However, it should be emphasized that the considerable impact of the liquid concentration difference is not due to the diffusion potential resulting from the salinity gradient. Instead, it is due to the streaming potential coefficient reduction by the high concentration liquid. The experimental data show that the main direction of liquid flow could be identified using the SP response. With an SP array, the fluid flow in an EGS reservoir could be mapped during both the fracturing and production stages. However, sufficient liquid saturation and rock porosity are needed to obtain a strong signal.

5. Heat Production from Lab-scale EGS

Due to the heterogeneity of the rock and the initial notch used to lower the breakdown pressure, the induced hydraulic fracture in Sierra White granite (SWG) did not propagate uniformly in every direction. As a result, not all the production wells were intersected by the hydraulic fracture in the case of the SWG. On the other hand, in the more homogeneous Raven Noir gabbro (RNG), all production wells were connected by the induced fracture during stimulation. Therefore, circulation tests with different number of the production well connected were obtained in this project, which in turn provides us with the opportunity to investigate heating mining under different scenarios. In this section, four different cases will be discussed. The first three cases were conducted with Sierra White granite, and the fourth case was carried out on a block of Raven Noir gabbro. In all circulation tests, the production well valves were open to maximize the production and to avoid fracture further propagation. Other strategies employed to lower the risk of uncontrollable fracture propagation include stepwise increase of the injection rate and acoustic emission monitoring. The highest injection rate achieved during circulation tests was 25 ml/min.

5.1 Case I: Heat Extraction form a Hydraulic Fracture Intersecting a Wellbore and Constrained in the Block

In this case, the induced fracture only intersected Well No.4 upon stimulation (as shown in Figure 5-1(d)). The fractured block was heated up to a uniform temperature of 63.6oC under a stress condition of 3.45MPa (vertical stress), 6.89 MPa (minimum horizontal stress) and 10.34 MPa (maximum horizontal stress). Figure 5-1(a) shows the injection pressure, injection rate, and the recorded AE hits. As mentioned before, to avoid uncontrolled fracture propagation to the block surfaces, the injection rate was slowly increased. The initial

injection rate was 1.5ml/min, reaching 25.0 ml/min in the last stage. It can be seen that from Figure 5-1(a) that at the onset, the injection pressure is high, and it decreases to a constant level at the end of the test. The initially high injection pressure is observed for two cycles of (low rate) injection. The subsequent pressure decrease is likely the result of fracture opening in response to thermal stress (Ghassemi et al., 2008; Ghassemi and Zhou, 2011; Rawal and Ghassemi, 2014; Ghassemi and Zhang, 2006) as well as changes in the water viscosity (Ghassemi and Tao, 2016). As shown in the figure, most of the AE hits occurred when the injection rate was increased. The total number of the recorded AE hits is about 60. However, the increased accumulative AE hits did not necessarily indicate the fracture propagation and could be the result of fracture aperture enhancement and adjustment (a very small aperture with a rough surface can experience crushing, breaking, and sliding during fracture opening). Acoustic emission activity due to the fracture aperture adjustment was also observed and by other researchers (Hampton, 2018) and in our step constant rate test right after hydraulic fracturing (Hu et al., 2019a).

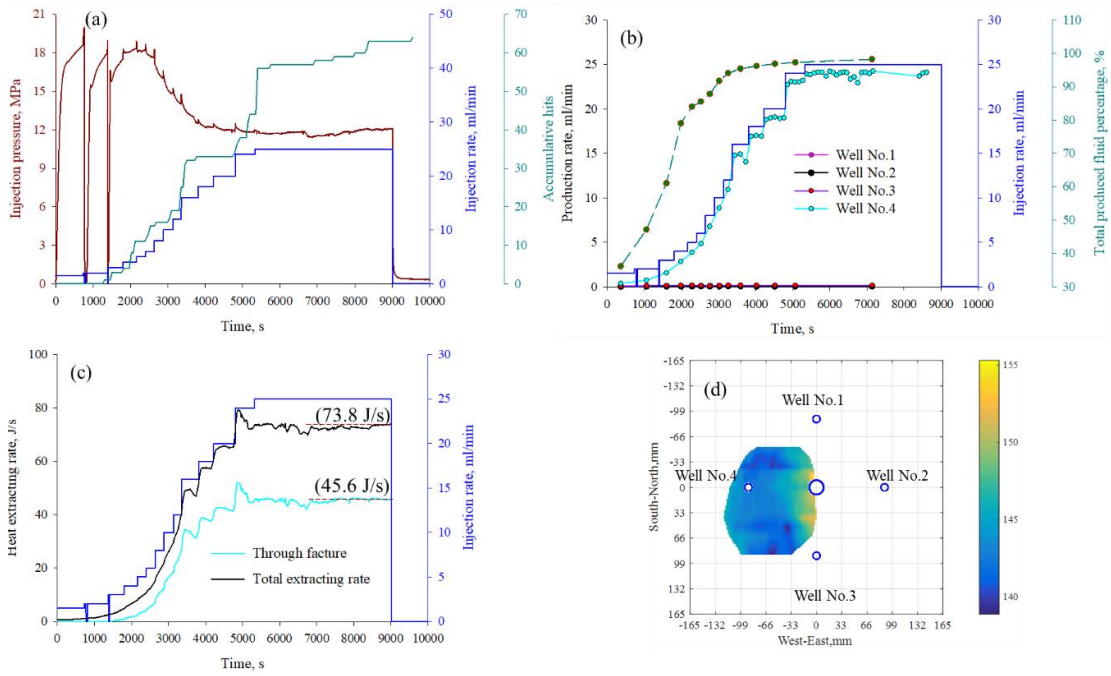


Figure 5-1. Case I results: Injection data and the recorded AE (a), production rate (b), heat extraction rate (c), the reconstructed fracture geometry (d).

During circulation, water produced from the production wells was collected and then weighed to calculate the production rate. Figure 5-1(b) shows the injection rate, production rate, and the percentage of the total produced fluid during the circulation test. It is found that the total percentage of the produced fluid increased when using a higher injection rate. This can be attributed to a lowering of the fluid loss into the rock matrix due to lower pressure in the fracture (pressure-dependent leak-off) and the improved hydraulic conductivity from the injection well to the producer. Since the induced fracture only intersected Well No.4, with injection rate of 25 ml/min Well No.4 produced 95.8 % of the injected fluid. The total flow rate from other production wells accounted for 2.5 % of the injection rate. So, only 1.7 % of injection fluid was lost to the rock matrix. This may provide some practical guide for field application: if early thermal breakthrough and undesirable fracture propagation could be

avoided, higher injection rate could result in not only higher production rate but also less fluid loss.

Figure 5-2(left) shows the temperature and the injection rate during the circulation test. The temperature at the bottom of the injection well decreased with increasing injection rate. The temperature change in the production wells was very small before t=2840s for two reasons; the temperature of the injected water was high due to the low fluid rate, and the cooling front had not reached the production wells yet. After two and half hours of circulation, the temperature in injection wells and production wells 1-4 was 20.7^{o}C, 57.7^{o}C, 59.3^{o}C, 57.4^{o}C, and 47.8^{o}C, respectively. The corresponding temperature drops were 43.0^{o}C, 6.1^{o}C, 4.6^{o}C, 6.5^{o}C and 16.0^{o}C. It is quite clear that since most of the injected water flows to Well No.4, it experienced the highest temperature drop among the production wells. The temperature decrease in other wells was caused by the fact that the central part of the granite block was cooled by cold water injection. So, the injected water temperature experienced a temperature increase of 27 ^{o}C as it traveled through the fracture and reached Well No.4. The apparent length of the fracture along that trajectory is about 88.9 mm (the distance from the injection well to the production well).

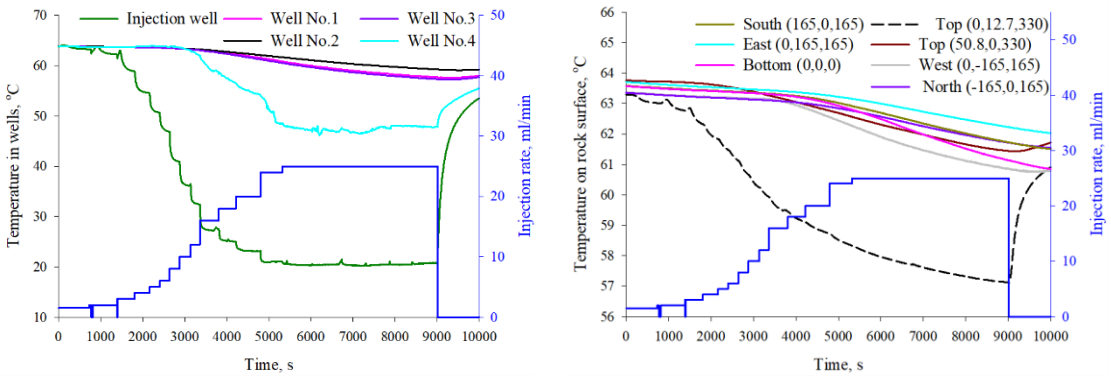


Figure 5-2. Temperature at the wellbore bottom (left) and on the rock surfaces (right) for Case I. The coordinates refer to the center of the bottom face of the block with positive x- , y-, and z-directions pointing to the north, west, and up, respectively. The units for coordinate are in mm.

Figure 5-2(right) shows the temperature variation on the rock block surfaces. It is apparent that at low injection rates, the temperature at the rock block surfaces were almost constant and at higher injection rates the temperature started to decrease. The temperature drop on the rock surfaces were: top (0, 12.7,330): 6.2^{o}C; top (50.8,0,330): 2.3^{o}C; west surface: 2.5^{o}C; north surface: 1.6^{o}C; south surface: 1.9^{o}C; east surface: 1.5^{o}C and the bottom surface: 2.4^{o}C. The PEEK plate placed directly on the rock surface (to obtain a better Self-potential (SP) signal) contributed to the relatively large temperature drop since its thermal conductivity (0.922W/m-K) is not high enough to transfer the heat from the heating system water to the rock. In subsequent cases (Case III), thin copper sheets or 0.5/1.0-inch-thick aluminum plates (Case II and IV) were used directly on the rock surface instead of PEEK plates. It should be pointed out that both PEEK plates and the aluminum plates have shallow grooves on the side attached to the rock to allow the water flow through. The temperature variation on the top surface near the injection tubing had the maximum variation (6.2^{o}C). The

influence of the injection tubing is limited to a couple of inches as indicted by the temperature change of the two points on the top surface.

The heat extracting rate and the total heat extracted during circulation was estimated based on the following assumptions and calculation. First, the water temperature at the injection wellhead was estimated based on the water tank temperature and the measured bottom hole temperature with the assumption that after the water enters the frame its temperature increases linearly from its value in the water tank to the injection wellbore temperature. With estimated water temperatures at the production wellhead, the temperature increase (the temperature difference between the production/injection wellheads, including the temperature gain by water flowing through the tubing and the induced fracture) was calculated. Note that the injected water is heated not only when it flows through the fracture but also when it flows in the wellbore. And due to size of the block, the extracted heat through the wellbore cannot be neglected. However, the heat extracted by fluid flowing through the induced fracture can be directly calculated since the temperature of the water at both the injection well and production well was directly measured. Based on the flowrate (of only Well No.4 because the flow rate in other wells is negligible) and the production temperature, the extracted heat was calculated by integrating the heat extraction rate curve (i.e., Figure 5-1c) from the beginning to the end of the circulation:

$$\dot{E} = \frac{dE}{dt} = \rho q c \Delta T \tag{5.1a}$$

$$E = \int_0^{t_{end}} \dot{E} dt \tag{5.1b}$$

where $\dot{E}$, ρ, q, c, ΔT, t_{end} are heat extraction rate, fluid density, volumetric flow rate, specific heat capacity of the fluid, temperature change, and period of the circulation test, respectively.

Figure 5-1 (c) shows that a higher injection rate results in a higher heat extraction rate and about 62% of the extracted heat is from the water flowing through the fracture. With the injection rate of 25 ml/min, the heat extracting rate is about 45.6J/s while the total heat extracting rate is 73.8 J/s. 421kJ heat was extracted during the whole circulation stage (about two and half hours), with 262kJ of the heat extracted by water flowing in the fracture.

5.2 Case II: Heat Extraction form a Hydraulic Fracture Intersecting a Wellbore and the Block Boundary

In this case, the induced fracture only intersected Well No.1, slightly connecting with the North surface of the block and passing underneath Well No.2 (Hu et al., 2019). The stress magnitudes applied were 3.45 MPa (500 psi) higher than in Case I with 6.89MPa (vertical), 10.34 MPa (minimum horizontal) and 13.79 MPa (maximum horizontal). After stimulation, the rock block was heated up to a uniform temperature of 76.6^{o}C and a circulation tests performed. Figure 5-3(a) shows the injection rate and pressure during the circulation test. The initial injection rate was 1.0 ml/min and at the end of the test, the injection rate had reached 24.0 ml/min. The injection pressure first increased with increasing injection rate but then it began to decline as the injection rate continued to increase. This is a clear manifestation of thermal stress caused by cooling the fracture faces (Ghassemi et al., 2008; Ghassemi and Zhou, 2011; Rawal and Ghassemi, 2014; Ghassemi and Tao, 2016). During the final stage of the test, the injection pressure was about 10.4MPa (about 1500 psi). The rapid pressure drop at the beginning of the circulation likely represents the reopening of the fracture. The fracture did not propagate during the circulation phase since no sudden pressure drops were observed after the initial event, and very few AE hits were observed. There are some small pressure drops in the injection pressure history and they are due to switching between the two injection pumps used.

Figure 5-3(b) shows the production data. Since only Well No.1 was intersected by the induced fracture, most of the injected fluid was produced from it. At a high injection rate of 24 ml/min, more than 92.2 % of injection fluid was recovered from production wells. Well No.1 yielded 91.6 % of the injected fluid in the later stages of the test. And the total flow in the other three production wells was about 0.6 % of the total injection rate. If it is assumed that the amount of fluid leaked off into the rock matrix was similar to Case I (since the injection pressure at the late phase for this two cases were similar), then the estimated fluid lost to the drum via the fracture intersection with the block surface is about 5~6 %. The relatively small fluid loss can be explained by the very small size of the intersection (about 3.3 cm as shown in Figure 5-3(d)). and the venting of all the production wells.

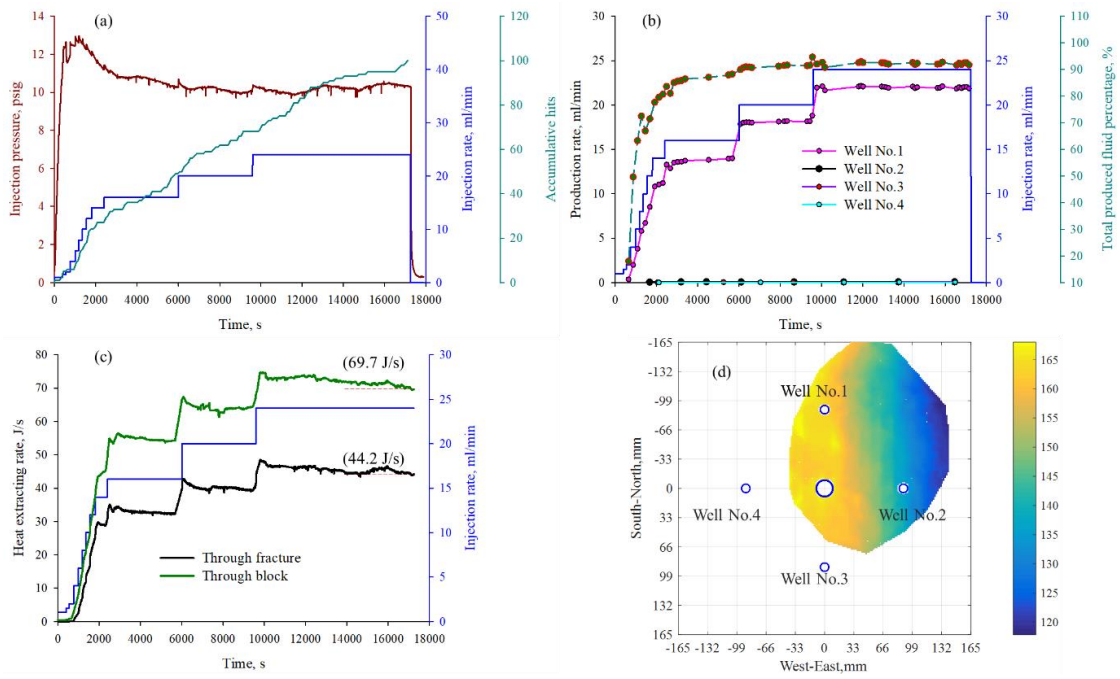


Figure 5-3. Case II results: injection data and the recorded AE (a), production rate (b), heat extraction rate during circulation (c), and the reconstructed fracture geometry (d).

Figure 5-4(left) shows the temperature evolution in the wells and the injection rate information during the circulation test. After a long time of circulation (about 4.8 hours), the temperatures at the wellbore bottom were: injection well: 20.2^{o}C; Well No.1: 49.9^{o}C; Well No.2: 67.2^{o}C; Well No.3: 71.7^{o}C; Well No.4: 71.0^{o}C. The temperature drop in these wells is: 52.6^{o}C, 26.8^{o}C, 9.5^{o}C, 5.0 ^{o}C and 5.7^{o}C, respectively. It is quite clear that since most of the injected water flows to Well No.1, it has the highest temperature drop among the production wells. The temperature decrease in other wells was caused by fact that the central part of the granite block was cooled by cold water injection. Figure 5-4(right) shows the temperature variation of the rock block surfaces. The impact of the injection tubing on the temperature distribution on the top surface was minimized. In this test, aluminum plates were put directly on the rock surfaces to facilitate heat transfer from the hot circulating water in the frame to the rock block. Compared with the previous circulation test results, the temperature on the rock surface is very stable even for with a much longer circulation time.

The heat extraction calculation (in Figure 5-3(c)) shows that a higher injection rate results in a higher heat extraction rate and about 63 % (which is very similar to Case I) of the extracted heat is from the water flowing through the fracture when the injection rate was 24 ml/min. In total, 1029kJ heat was extracted during the circulation stage, with about 643kJ of the heat extracted by water flow in the fracture.

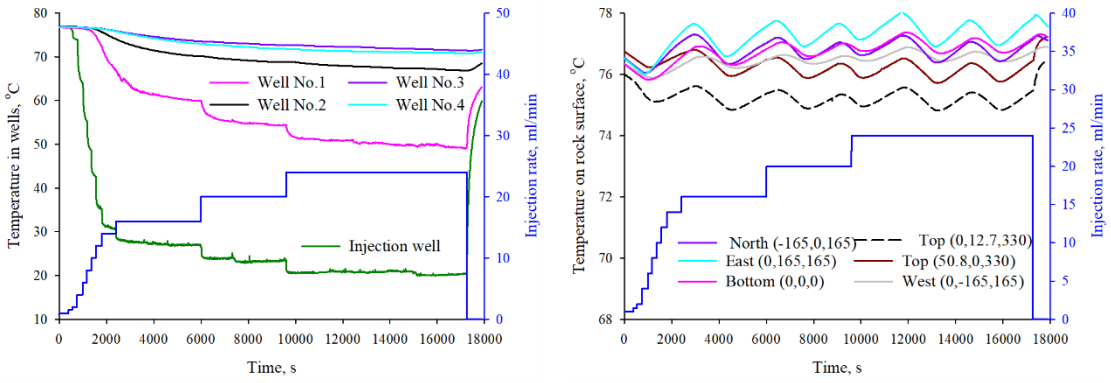


Figure 5-4. Temperature at the bottom of the wells (left) and on the rock surfaces (right) (Case II).

5.3 Case III: Heat Extraction from a Hydraulic Fracture Connected with Two Wells

The stimulation of the block resulted in a horizontal fracture that connected with two of the production wells (Well No.3 and Well No.4). The induced hydraulic fracture reached to within several millimeters of Well No.2. After stimulation, the rock was heated to a uniform temperature of 68.9°C in preparation for the circulation test. The stress condition used was: 3.45MPa (vertical), 6.89 MPa (minimum horizontal), and 10.34 MPa (maximum horizontal). Figure 5-5(a) shows the injection rate and pressure during the circulation test. The initial injection rate was 2.0 ml/min, reaching 25.0 ml/min at the end. The pressure record shows a large pressure drop at the onset of the test. It is our opinion that the hydraulic fracture had somewhat healed (for this test block, the circulation test was conducted one week after the hydraulic fracture stage) during the heating process while it was subject to the applied stresses.

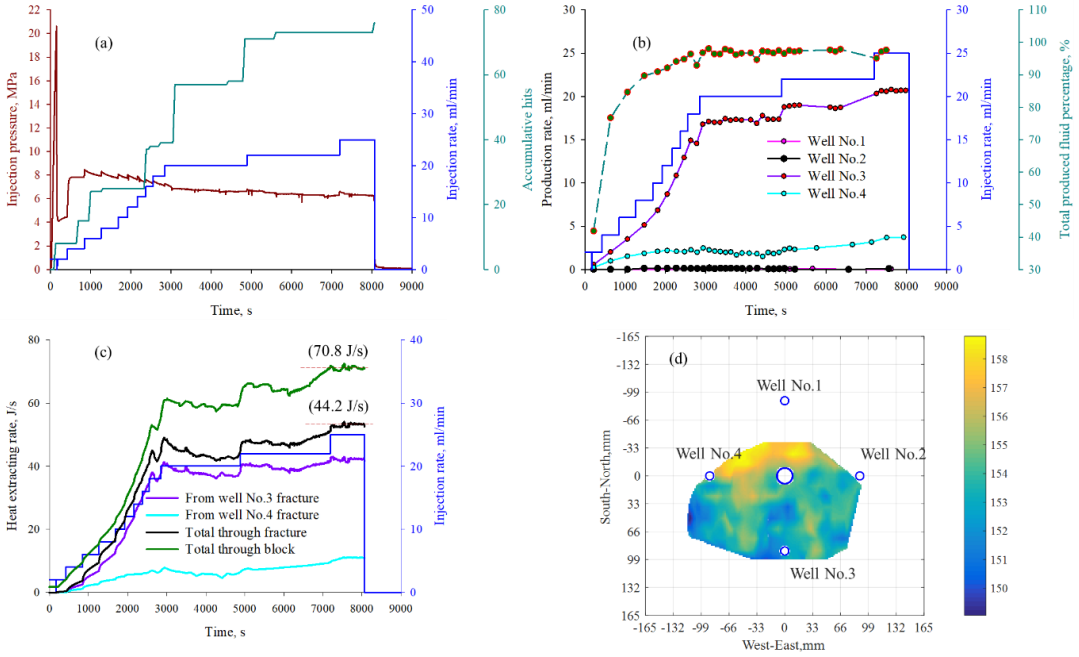


Figure 5-5. Case III results: Injection data and the recorded AE(a), production rate (b) and heat extraction rate (c), and the reconstructed fracture geometry (d).

It seems the fracture did not propagate much during the whole circulation phase since no sudden pressure drops occurred and the accumulative number of AE hits was small and most of them occurred whenever the flow rate was increased suggesting fracture aperture re-adjustments or local failure events in the neighborhood of the fracture. Figure 5-5(b) shows the production data, from which it is clear that Well No.1 produced most of the injected fluid. At high injection rates, more than 97.5 % of the injection fluid was recovered from the production wells. Well No.3 and No.4 each produced 82.8 % and 14.8 % of the injected fluid at the later stages. And the total flow in the other two production wells was less than 1.0% of the injection rate. During the circulation, a competition between Well No.3 and No.4 is observed. At the beginning of the circulation, the production rates of these two wells increased with the injection rate. However, after the injection rate reached 10 ml/min, the production rate in Well No.4 remained low and nearly constant (a slight increase was

observed in the last stage). This is essentially a short circuiting (refer to Case IV) phenomenon. The injected fluid tends to flow through the path of higher conductivity, cooling the adjacent rock matrix and causing further fracture aperture increase and enhancing flow concentration. This phenomenon indicates that, well management is also required in EGS field especially when several production wells are connected to the same injection well. Figure 5-6(left) shows the wells temperature and injection rate information during the circulation test. After about 8000s (two hours and 13 minutes) of circulation, the well temperatures were: injection well: 16.9^{o}C; Well No.1: 64.6^{o}C; Well No.2: 64.2^{o}C; Well No.3: 45.3^{o}C; Well No.4: 59.0^{o}C as shown in Figure 5-6. These correspond to temperature drops of 52.6^{o}C, 4.5^{o}C, 4.8^{o}C, 23.8^{o}C and 10.0^{o}C, respectively. It is quite clear that since most of the injected water flows to Well No.3, it has the highest temperature drop. The temperature drop was also higher in Well No.4 than the other two non-producing wells. The small temperature decrease in other wells was caused by fact that the central part of the granite block was cooled by cold water injection and heat extraction.

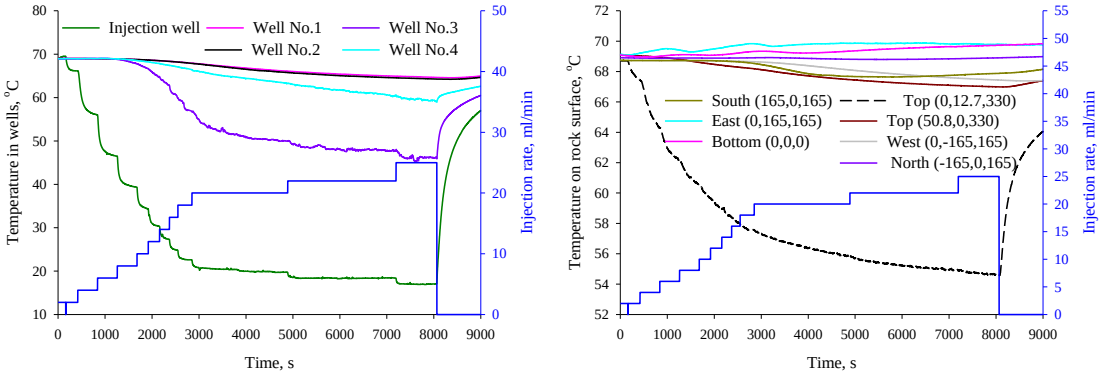


Figure 5-6. Temperature at the bottom of the wells (left) and on the rock surfaces (right) for Case III.

Figure 5-6(right) shows the temperature variation on the rock block surfaces. During the circulation test, the temperature change on the north, east and bottom surface was less than 1^{o}C. While the top, south and west surfaces had a higher temperature change due to the injection tubing and the fact that the production wells corresponding to these surfaces were connected by the fracture. The measured temperature change close to the injection tubing is larger than other test since it is closer to the injection tubing.

Figure 5-5(c) shows that a higher injection rate results in a higher heat extraction rate and about 74% of the extracted heat is from the water flowing through the fracture when the injection rate was 25 ml/min. 398kJ of heat was extracted during the whole circulation stage, with about 295 kJ of the heat extracted by water flow in the fracture.

5.4 Case IV: Heart Extraction from a Hydraulic Fracture in Gabbro Intersecting Four Wells

The fourth case study was conducted on a block of the Raven Noir gabbro which has an extremely low porosity and permeability. The rock is fine grained and more homogeneous than the Sierra White granite. In this case, the induced fracture intersected all four production wells during stimulation. Then the rock block was heated up by hot water circulation in the drum to a uniform temperature of 77.7^{o}C (in this test the heating process took about 24 hours because the high power heater was shut-down intentionally after 3 hours of working, and the target temperature was also higher). The stress condition was: 6.89MPa (vertical), 10.34 MPa (minimum horizontal) and 13.79 MPa (maximum horizontal) stress.

Figure 5-7(a) shows the injection rate and pressure during the circulation test. The initial injection rate was 0.2 ml/min and at the end period of the test, the injection rate was 25.0 ml/min. The injection pressure first increased with injection rate and then decreased with increasing injection rate. As before, this is attributed to increased aperture in response to thermal stress by cooling of the rock matrix around the fracture. At the later stage, the injection pressure was about 9.17 MPa (1330 psi).

Since the rock block is almost non-porous and the induced fracture is within the rock block, all the injected fluid was produced from production wells. At the beginning of the circulation test, the production rate in all production wells increases with increasing injection. Later, Well No.3 started to dominate the production and production in other three production wells started to decrease to a negligible level.

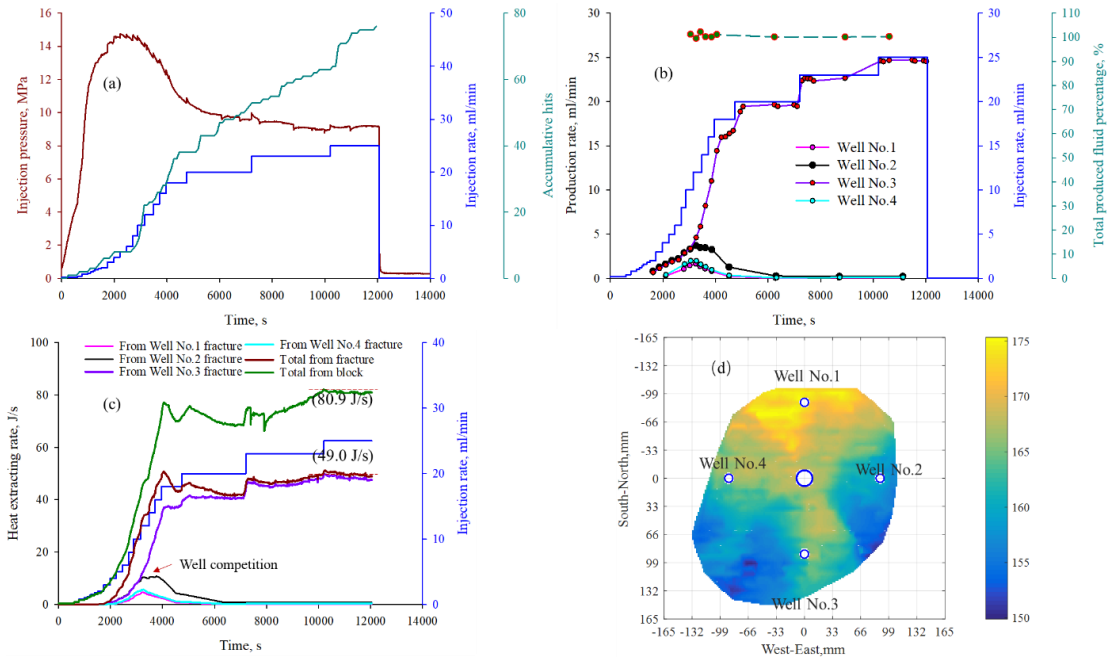


Figure 5-7. Case IV results: Injection information and the recorded AE(a), production rate (b) and heating extraction rate (c), and the reconstructed fracture geometry (d).

During the last stage of circulation, about 98.2% of the injected fluid was produced from Well No.3 and only less than 2 % was being produced from all other three production wells. It can be expected that the well competition could have been mitigated if the injection rate had remained at the level where production rates from Wells 2 and 3 were increasing harmoniously, but it is unlikely it could have been completely avoided. It can be observed from the reconstructed fracture geometry (Figure 5-7(d)) that the fracture propagated more outwards in the Well 3 direction. Furthermore, the flow path from the injection well to Well 3 has less elevation variation and thus it has a small tortuosity and higher hydraulic conductivity (and lower normal stress). All these elements favored fluid flow to Well No. 3.

Figure 5-8(left) shows the temperature in the wells and the injection rate information during the circulation test. After a 12053 s (3 hours and 20 minutes) of circulation, the well temperatures were: injection well: 20.8^{o}C; Well No.1: 71.9^{o}C; Well No.2: 71.0^{o}C; Well No.3: 49.1^{o}C; Well No.4: 70.4^{o}C. The temperature drops in these wells are: 57.1^{o}C, 6.2^{o}C, 7.0^{o}C, 28.7^{o}C and 7.5^{o}C, respectively. It is quite clear that since most of the injected water flows to Well No.3, it has the highest temperature drop among the production wells. The temperature decrease in other wells was caused by fact that the central part of the granite block was cooled by cold water injection.

Figure 5-8(b) shows the temperature variation on the rock block surfaces. In this test, an aluminum plate was put directly on the rock surface to help transfer the heat from the hot water to the rock block. The impact of the injection tubing on the temperature distribution on the top surface was minimized. The temperature change on all the rock surfaces is around 1^{o}C.

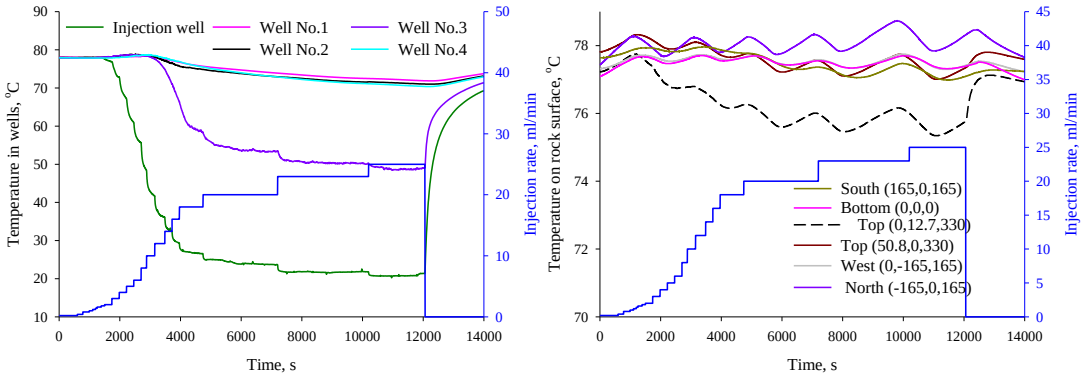


Figure 5-8. Temperature at the bottom of the wells (left) and on the rock surfaces (right) for Case IV.

Figure 5-7(c) shows that a higher injection rate results in a higher heat extraction rate and about 61% of the extracted heat is from the water flowing through the fracture when the injection rate was 25 ml/min. 684kJ heat was extracted during the whole circulation stage, with about 424kJ of the heat extracted by water flow in the fracture. It is worth noting that before the "short circuit" was established, about 67 % of the heat was extracted from the fracture, which means well management is essential for a EGS systems with multi-production fractures connected to the same injection well(s). No attempt was made in this test to divert flow to other wells by shutting the main production well.

5.5 Comparison of the test data with Gringarten solution

Gringarten et al. (1975) presented the analytical solution for heat extraction from fractured hot dry rock. In the investigated model, two wells connected a series of parallel vertical fractures of uniform aperture and the cold water is injected from the to the deeper well and hot water is produced from the upper production well. With several assumptions such as 1) constant properties for both the formation and water; 2) water temperature is uniform in any cross section of the facture and is same as the formation temperature and the fracture wall;

3) the heat transport in the formation is one dimensional and by forced convection in the fracture and 4) Initially, both the water in the fracture and the formation are at the same temperature. The analytical solution for the case with single fracture and without geothermal gradient in vertical direction could be given as following:

$$T_{WD}\left(t_D^{'}\right)=1-erf\left(\left(t_D^{'}\right)^{-0.5}\right) \tag{5.2a}$$

In which, the dimensionless parameters were defined as:

$$T_{WD}=\left.T_{RO}-T_W\left(z,t\right)\right/T_{RO}-T_{WO} \tag{5.2b}$$

$$t_D^{'}=\left[\left(\rho_w c_w\right)^2/\left(K_R\rho_R c_R\right)\right]\left(Q/z\right)^2 t^{'} \tag{5.2c}$$

$$t^{'}=t-\left.z\right/v \tag{5.2d}$$

Where, T_{RO}, T_{WO} are the reservoir temperature and the injection temperature, respectively; $T_{W(z,\,t)}$ is the water temperature in the fracture at a distance z from the inlet. To model the experiment, the distance from the injection well to the production well is used as z (8.89 cm). ρ_w, ρ_R, c_w, c_R are the density, specific heat for water and formation rock respectively; K_R is the rock thermal conductivity; Q is the volumetric flow rate per fracture per unit thickness; $\left.z\right/v$ is the time lag between the departure of the water from the injection point and the arrival time at point z and it could be ignored if the time slag is very small.

The experimental data from Case II are compared with the analytical solution of Gringarten. The recorded test data is shown in Figure 5-9. The constant parameter used to calculate the dimensionless parameters for the water and test rock is given in Table 5.1. The investigated

time interval was marked out with the two red dash lines. And the average injection rate and average injection temperature during this period was used for the calculation.

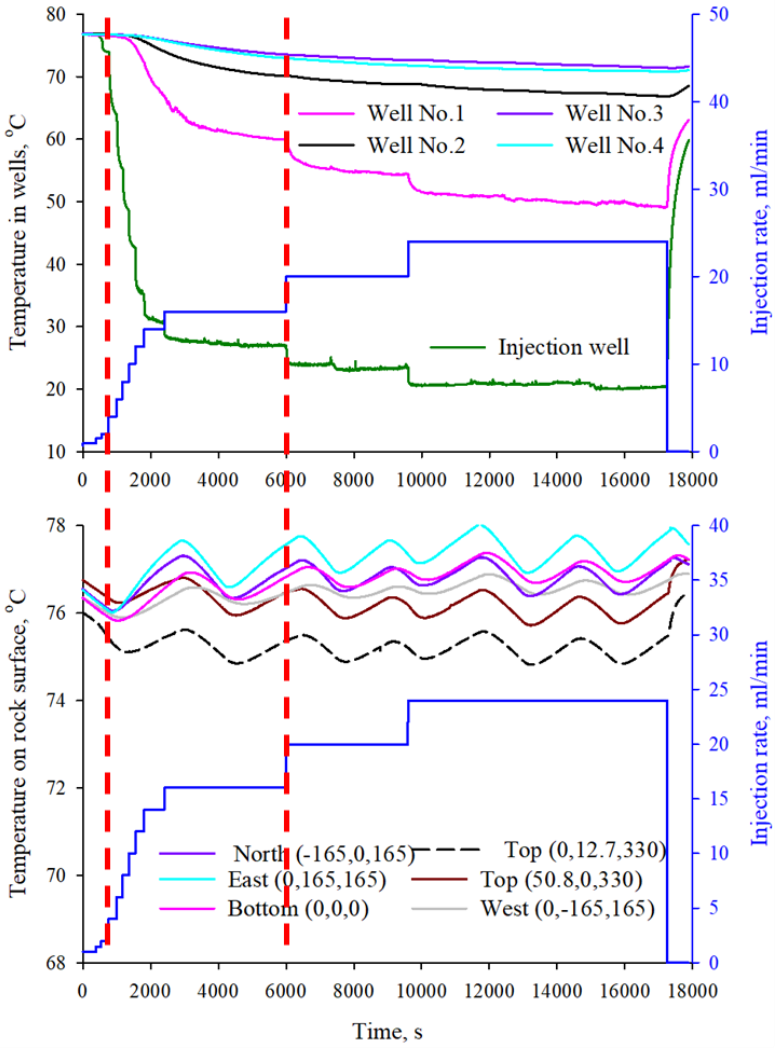


Figure 5-9. The injection rate, injection temperature, production temperature and the temperature and the rock boundaries.

Table 5.1. The properties for water and granite and the test conditions

Quantity	units	value
Injection rate	ml/min	14.19
Rock specific heat	J/(kg K)	793
Water specific heat	J/(kg K)	4180
Injection temperature	^{o}C	32.4
Reservoir temperature	^{o}C	76.6
Rock thermal conductivity	$W \cdot m^{-1} \cdot K^{-1}$	2.8
Flow distance	cm	8.89
Fracture width	cm	16.4

The analytical solution and the result from our test is shown in Figure 5-10, in which a good agreement is obtained. The main factor contributing to the difference at the later time of the investigated time period is the impact of boundary condition. The Gringarten solution with one fracture assumed infinite size of the reservoir while in the lab test the constant temperature boundary has a finite distance from the fracture. Moreover, in the Gringarten solution one the heat conduction perpendicular to the fracture was considered while in lab test, the heat conduction in the rock block is three dimensional. These factors lead to a higher production temperature in the test (i.e, lower dimensionless produced temperature).

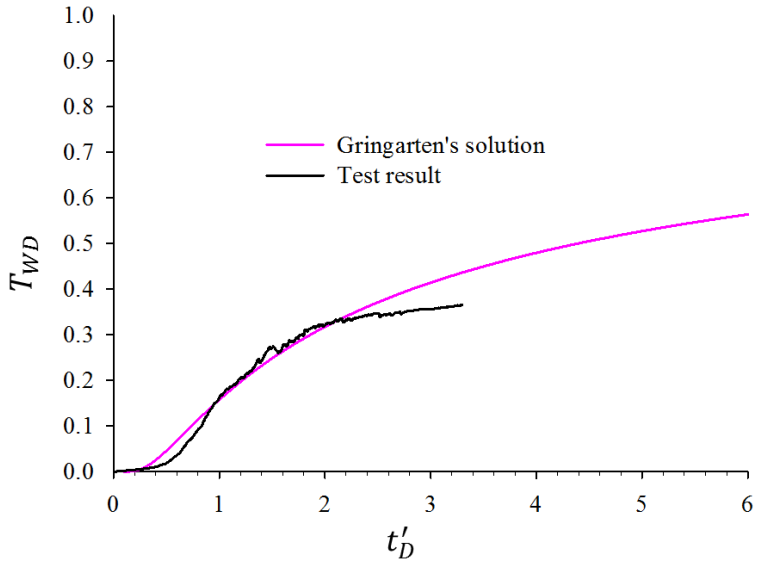


Figure 5-10. Comparison between the Gringarten's solution and the test result.

5.6 Summary and Conclusions

A novel Lab-scale EGS apparatus was designed and used to simulate EGS hydraulic fracturing and circulation experiments relying on hydraulic fracturing for reservoir creation rather than other reservoir creation mechanisms (Ye and Ghassemi, 2018 and 2019). Table 5.1 summarizes the most important data on heat extraction for the test cases described in the text. Only the heat extracted via the hydraulic fractures is used to calculate the heat extraction rate listed in the table. The reconstructed fracture geometries (2D) are also provided in Figure 5-9.

Table 5.2. Important data for all the test cases

Parameters	**Case I**	**Case II**	**Case III**	**Case IV**
Rock type	SWG*	SWG	SWG	RNG**
Boundary temperature, ^oC	63.6	76.6	68.9	77.7
Stored heat energy in the rock block, kJ	2867	3832	3261	3914
Maximum injection rate, ml/min	25.0	24.0	25.0	25.0
Injection pressure [a], MPa	12.4	10.4	6.3	9.2
Flow impedance [b], MPa/(ml/min)	0.496	0.433	0.252	0.368
Temperature increase [c], ^oC	27.0	29.8	28.8	28.4
Heat extracting rate [d], J/s (W)	46.15	40.13	52.5	46.8
Power consumed for pumping [e], J/s	5.17	4.16	2.62	3.83
Injection rate at 2000 ml injection [f], ml/min	25.0	20.0	25.0	23.0
Fracture area, cm^2	144	345	224	495
Circulation time, hours	2.5	4.8	2.2	3.3
Total extracted heat [g], kJ	262	643	295	424
Total extracted heat [h], kJ	215	239	256	262
Percentage of extracted heat [i], %	7.15	6.24	7.85	6.69
Heat extraction rate per unit injection rate, W/(ml/min)	1.85	2.00	2.10	2.03
Heat extraction rate per unit injection rate pure unit area, W/(ml/min*cm^2)	0.013	0.006	0.009	0.004

a: The injection pressure at the maximum injection rate.
b: The flow impedance at the maximum injection rate.
c: The temperature increase for the water produced from the production well at maximum rate
d: The heat extracting rate when the injected volume reached 2000 ml.
e: The power consumed for pumping the injection fluid into the block.
f: The injection rate when the injected volume reached 2000 ml.
g: The total heat extracted from the induced fracture for the whole circulation test.
h: The total heat extracted from the induced fracture when the injected volume reached 2000 ml.
i: The percentage of extracted heat from the induced fracture when the injected volume reached 2000 ml.
SWG*: Sierra White granite; RNG**: Raven Noir gabbro

The color in the Figure 5-11 indicates the fracture surface height variation. Comparing the test results and the fracture geometry yields some useful information and insights. The first interesting finding is the flow impedance in different cases as listed in the table. It is noticed that Case III has the lowest flow impedance (almost only half of that in Case I), and this is because in Case III two production wells were producing (larger accessible drainage area) while in other cases only one production well produced (in Case IV, all four production wells produced in the beginning, but in later phase of the circulation, only one well produced due to well competition). Case I and Case II had similar flow impedances, since in cases one production well was intersected by the fracture in the same type of rock. Case IV had a smaller flow impedance compared with Case I and Case II, and this is mainly due to the fact that the induced fracture in the gabbro has smaller tortuosity (demonstrated by the 3D laser scan profile, in Table 3.1) and more homogenous flow geometry (as shown in the tracer analysis at Chapter 6, refer the F-Φ curve in Figure 6-5 and Figure 6-11). So, the impact of rock texture on the fracture geometry and profile and thus on the fluid flow/ heat transfer is observed in the tests.

The great potential of geothermal energy as the future clean energy supply was demonstrated by the fact that about 50W of power was produced in each test from a fracture with 9 cm (3.5-inch) pathway (the distance from the injection well to the production well) in a 330.2 mm (13-inch) cubic rock block with temperature less than 80^{o}C. And the power required to inject the water to flow through the induced fracture (product of the injection rate and injection pressure) was less than 6W as listed in Table 5.2. In the field, the well distance can be several hundred meters and the rock temperature could reach 200 ^{o}C. The initial heat energy stored in the heated blocks relative to room temperature is listed in Table 5.1. This is

based on the initial temperature and the volumetric specific heat capacity of the rock (assumed to be 2060kJ/ (m^3. K)). The percent heat extracted corresponds to that from circulation of 2000 ml of water. It is found that about 6.24 %~ 7.85% of the heat stored in the heated rock blocks is produced by circulation through the fracture.

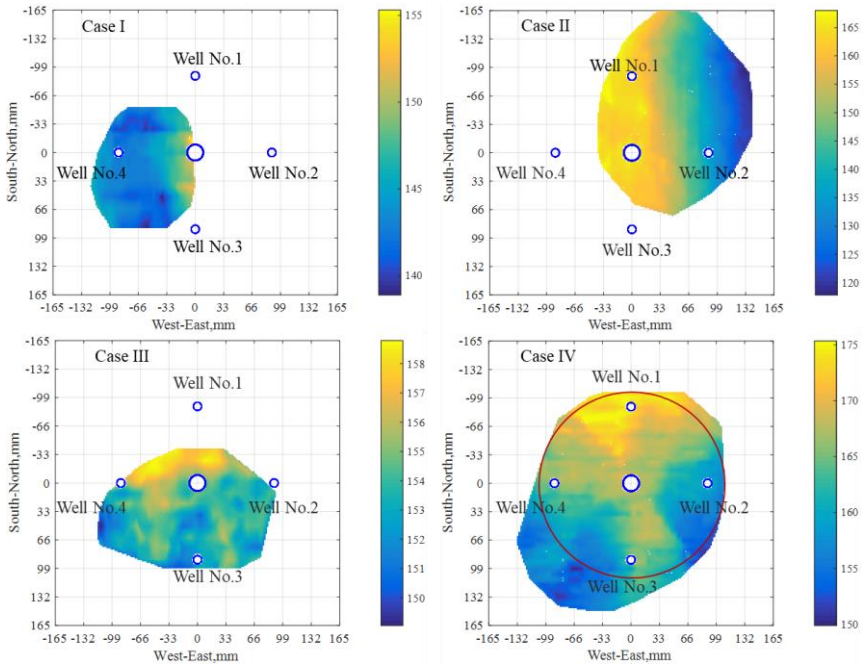


Figure 5-11. Top view of the fracture geometry for the tests discussed above. The color indicates the height variation of the fracture surface and the dark red circle indicates the possible induced fracture front after reservoir stimulation.

The heat extraction rates per unit injection rate when 2000 ml of cold water was injected are listed in Table 3 for all cases. It is found that the Cases II and IV have a similar heat extraction rate value (2.0 W/(ml/min)) reflecting the fact that the two systems have similar effective heat exchange area and boundary temperature (the injected fluid was produced from one producer in both cases at the moment when 2000 ml cold water was injected). Case I has a lower value since the boundary temperature was lower in that case. Case III has the highest value even though the boundary temperature is about 9 degrees less than Case II and Case

IV. This is because Case III has a larger effective heat exchange area (production is from two wells producing fluid with considerable flow rate).

The heat extraction rate per unit injection rate per unit fracture area (HEPIPA) was calculated and listed is in Table 5.1. The calculated values (Case I: 0.013, Case II: 0.006; Case III: 0.009; Case IV: 0.004) show that Case IV has the smallest HEPIPA even though it has the largest fracture area. This is because the heat extraction rate is a function of the effective heat exchange area (the actual flow path between the injection and production well) rather than the total fracture surface area. This suggests that the distance between injection/production wells or the location of the producer(s) and flow path tortuosity need be optimized to increase the effective heat exchange area in reservoir stimulation practice. The maximum heat extraction rate is obtained in Case III where both of the production wells intersected by the hydraulic fracture were producing.

The results of the circulation tests highlight the importance of reservoir creation and field management, i.e., controlling the injection and production rates to obtain a higher thermal production rate. For example, in both Case III and Case IV, multiple production wells were connected to the injection well but Case III had a higher heat extraction rate. In Case IV there was serious short circuiting and the production rate in three of the production wells dropped to a negligible level.

In Case IV, the injected fluid was produced from all production wells at the beginning of the circulation test, however, later the injected water was produced solely from Well No. 3. This was likely caused by slight fracture propagation in the S-SW direction as can be seen in Figure 5-9 (the likely outline of the hydraulic fracture prior to 3000s is marked by the dark

red circle. The suggestion that the fracture extended during the circulation phase in the period 3000s-4500s, is supported by the sudden jump in AE activity during the same time interval (see Figure 5-7). The asymmetric fracture growth and the fracture geometry and morphology enhanced and focused flow into Well No. 3. The impact of fracture geometry/tortuosity on the preferential flow path development is evident in tests results. In the case where multiple wells were connected by the induced hydraulic fracture, the fluid tends to flow into the direction with less tortuosity and thus lower flow impedance. For example, in Case IV, the flow path from the injection well to Well No.3 has less elevation variation and thus, it has a smaller tortuosity and higher hydraulic conductivity as shown in Figure 5-9, which favored flow to Well No.3.

Excessive fracture propagation and high injection pressure was avoided during circulation tests by increasing the injection rate step by step. The cooling effect of the rock matrix i.e., increased fracture conductivity and lowering of the injection pressure is clearly manifested in the circulation experiments. Numerical simulation had suggested that thermal, mechanical, and hydraulic effects must be considered when modeling the behavior of an EGS reservoir. This is confirmed in our circulation experiments. For example, the injection pressure history in all the circulation phases indicates that the cooling of the rock matrix has a very important impact on the fracture flow capacity. The test results provide insight for performing similar tests at larger scales e.g., in the COLLAB and FORGE projects.

6. Lab-scale Tracer Test in Enhanced Geothermal System

6.1 Calculation of the Tracer Concentration and Methodology Verification

In Chapter2 the tracer system was presented and the fluid properties were given. In this Chapter, the method to analyze the test data will be discussed in detail. During the tracer test, production rate (usually less than 0.3 ml/min) from the production wells was small and the instrument used to measure the fluid conductivity cannot lack sufficient sensitivity in very small fluid volume, the collected fluids were diluted with deionized water and the original fluid concentration was calculated based on the added fluid volume and conductivity of the resulting fluid. This approach has been verified with standard fluids as described below.

Before tracer test, the weight of the empty sample containers was measured and recorded. And then a certain amount of deionized water was added to the container, the total weight of the container and the added water was measure and recorded. After a tracer test, the final weight and concentration of the resulting fluid was measured. Using this information, the concentration of the produced fluid was calculated based on the mass conservation:

$$\frac{m_d}{\rho_d} C_d + \frac{m_t}{\rho_t} C_t = \frac{m_r}{\rho_r} C_r \tag{6.1}$$

Where, m_t, m_d, and m_r is the weight of the tracer fluid, deionized water, and resulting fluid respectively, g; ρ_t, ρ_d, and ρ_r is the density of the tracer fluid, deionized water and resulting fluid respectively, g/cm^3; C_t, C_d, and C_r is the concentration of the tracer fluid, deionized water and resulting fluid respectively, PPM. The relationship between electrical conductivity vs concentration and density vs concentration is shown in Figure 2-9. The concentration of

the collected production fluid is then calculated with EQ (6.1) and the relationship list in Figure 2-9.

To verify the feasibility and the accuracy of the proposed method, OAKTON conductivity standard fluids with known conductivities were used as tracer. The results of the trial tests using a series of standard fluids with different concentrations and weights are listed in Table 6.1. The calculated and true conductivities of the tracer fluid and their difference are plotted in Figure 6-1. The relative error variation with tracer weight and fluid concentration is plotted in Figure 6-2. It can be seen from the figures that the accuracy of the proposed method is very good except at very low concentrations. The larger error for the low concentration scenario is caused by the fact that the concentration of the resulting diluted fluid is very small and can be contaminated easily causing the conductivity of the resulting fluid to be relatively higher.

Table 6.1. The results of the feasibility test of the proposed method to measure the conductivity of small volumes of the produced fluid

Sample ID	Water weight, g	Tracer weight, g	Water conductivity, us/cm	Resulting fluid conductivity, us/cm	Real Conductivity, us/cm	Calculated Conductivity, us/cm	Error, %
1	29.43	0.13	1.30	1.79	84	108.48	29.14
2	28.51	0.12	1.35	1.82	84	109.17	29.97
3	29.74	0.22	1.37	2.16	84	105.05	25.06
4	31.17	0.21	1.35	2.08	84	106.40	26.66
5	29.06	0.40	1.42	2.78	84	99.26	18.16
6	29.98	0.50	1.44	3.05	84	97.63	16.23
7	28.70	0.10	1.40	3.10	447	459.92	2.89
8	30.12	0.10	1.37	3.00	447	462.24	3.41
9	24.65	0.20	1.42	5.30	447	455.77	1.96
10	28.83	0.22	1.39	5.10	447	462.79	3.53
11	28.16	0.41	1.39	8.10	447	466.81	4.43
12	23.44	0.42	1.49	9.50	447	468.12	4.72
13	24.46	0.10	1.38	7.63	1413	1478.75	4.65
14	25.27	0.11	1.52	8.05	1413	1470.47	4.07
15	27.32	0.20	1.35	12.17	1413	1442.02	2.05
16	27.25	0.20	1.36	12.54	1413	1477.77	4.58
17	29.28	0.43	1.46	23.15	1413	1367.65	-3.21
18	29.76	0.42	1.41	22.17	1413	1355.23	-4.09
19	26.07	0.11	1.32	14.40	2764	2878.37	4.14
20	28.14	0.10	1.36	11.95	2764	2862.84	3.58
21	31.61	0.20	1.37	20.04	2764	2638.91	-4.53
22	29.87	0.20	1.51	22.38	2764	2809.46	1.64
23	27.43	0.40	1.36	42.43	2764	2674.07	-3.25
24	28.87	0.40	1.35	41.62	2764	2755.10	-0.32
25	28.09	0.11	1.34	58.43	12880	12454.08	-3.31
26	29.71	0.10	1.50	52.74	12880	12994.61	0.89
27	29.98	0.19	1.40	94.49	12880	12587.15	-2.27
28	29.35	0.20	1.41	102.60	12880	12782.01	-0.76
29	30.31	0.38	1.41	189.20	12880	13018.90	1.08
30	30.45	0.39	1.43	188.5	12880	13018.90	1.08

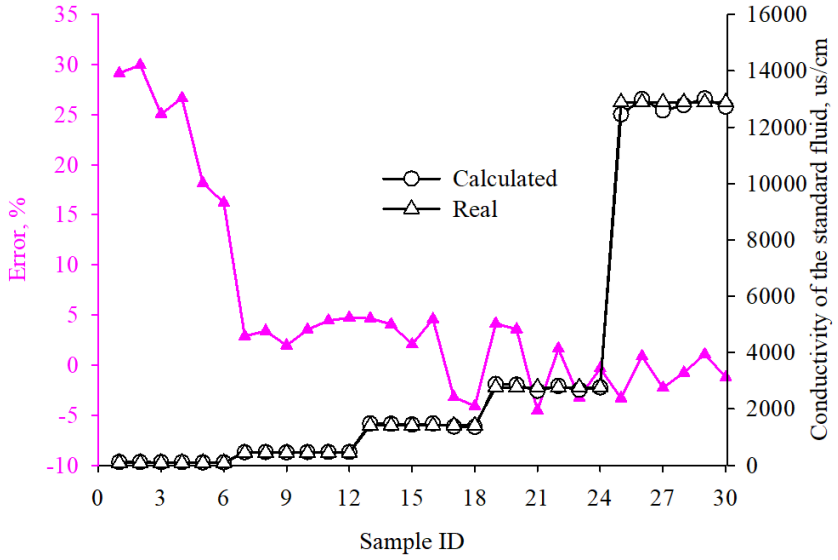


Figure 6-1. The true and calculated conductivity of the tracer fluid and the corresponding errors.

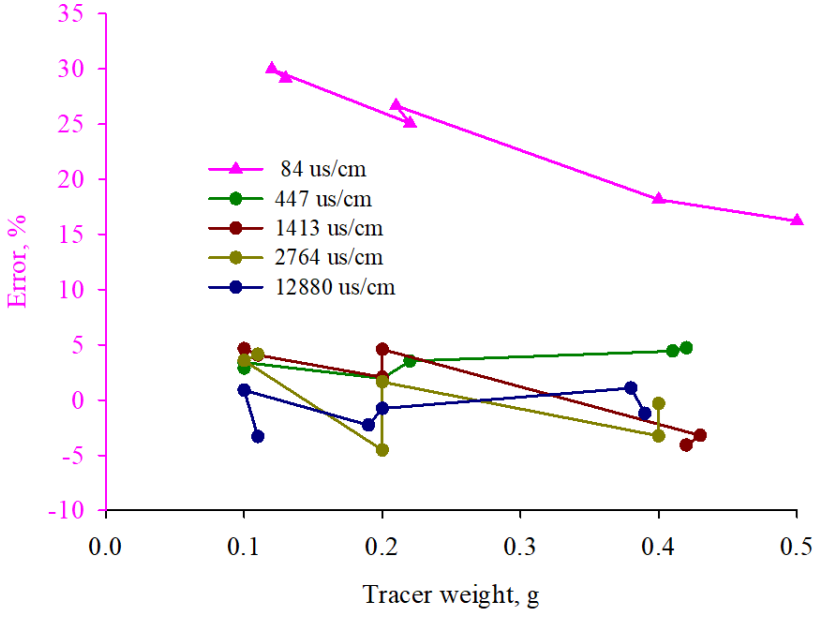


Figure 6-2. The error of the calculated conduction for different standard fluid with different weight.

6.2 Velocity of the Tracer Fluid in the Fracture

The primary motivation for tracer tests in early field applications was to obtain a better understanding of the fluid movement and the formation hydraulic conductivity. In our lab-scale fracture characterization, the velocity in the stream-line directly connecting the injector and the producer in the hydraulically induced fracture has been investigated based on the fluid travel time from the injection well to the production well. Since the tracer concentration was measured after the fluid was produced from the production tubing as shown in Figure 2-5, it was necessary to calculate the time needed for the fluid to flow from the pump to the bottom of the injection well, and from the bottom of the production well to the collection point outside the polyaxial frame housing the sample. As mentioned before, the length of the hydraulic tubing was measured and based on the injection/production rates and the geometrical information of the tubings (inner diameter and length), the travel time of the fluid in the tubings was estimated. Thus, the tracer travel time in the fracture is obtained by subtracting the travel time in the tubing from the total travel time, and the total travel time is determined from the tracer concentration curve at the point when the fluid concentration starts to increase The apparent average velocity is estimated using the distance from the injection well to the production well (88.9 mm), and due to the tortuosity (about 1.1 for hydraulic fracture in Sierra White granite, refer to Hu et al., 2019 and 1.05 for Raven Noir gabbro) of the fracture (and thus the flow path), the true velocity would be larger than the calculated value

6.3 Determination of Swept Volume with the Method of Moments

Methods for the temporal analysis of tracer were originally developed for closed reactor vessels (Danckwerts 1953; Levenspiel 1972). However, they have been employed in

characterization of, fractured reservoirs under continuous tracer reinjection (Robinson and Tester, 1984), and for estimating the flow geometry (Shook, 2003). Himmelblau and Bischoff (1968) provided detailed derivation of the method of moments for analyzing packed beds reactors. The tracer swept volume can be estimated from the mean residence time obtained from the first temporal moment of the tracer response curve (Himmelblau and Bischoff, 1968; Levenspiel 1972; Zemel, 1995). In the case of a slug injection of duration t_{slug} with constant injection rate, the mean residence time of the tracer in the medium is defined as EQ (6.2) (Jin, 1995).

$$t^* = \frac{\int_0^\infty Ctdt}{\int_0^\infty Cdt} - \frac{t_{slug}}{2} \tag{6.2}$$

where $C, t^*,$ and t_{slug} denote tracer concentration, the mean residence time, tracer slug injection period, respectively.

In field applications, sample collection usually is terminated before the tracer concentration level falls below the resolution of the measurement device. The exponential decline is the most common tracer decline trend observed in the field (Shook and Forsmann, 2005), so it is commonly used to extrapolate the tracer history. However, two linear portions of the tracer tail in semi-log plot have been predicted by some numerical models (Tian et al, 2016) and also have been observed in some field tests (Axelsson, et al 2001; Leong, et al 2015). The first linear portion is mainly controlled be the fracture flow while the second linear tracer tail is due to the tracer from the fluid that leaked-off into the matrix during the injection stage, which flows back at later stages of production. This phenomenon has been observed

in our lab-scale tests, so that only the first linear part of the tracer tail was employed to estimate the tracer decline trend (Tian et al., 2016). Shook and Forsmann (2005) presented the procedure for interpreting geothermal tracer tests to obtain the tracer swept volume based on the first temporal moment of the tracer and showed the volume swept by the tracer can be estimated by the following equations:

$$C = be^{-at} \quad for\ t > t_b \tag{6.3a}$$

$$V_{swept} = q_{inj} \frac{m}{M_{inj}} t^* \tag{6.3b}$$

where $C, t_b, m, M_{inj}, q_{inj}$, and V_{swept} denote tracer concentration, time at which the onset of the exponential decay of tracer history is observed, mass of the produced tracer, total mass of the injected tracer, volumetric injection rate, and tracer swept volume, respectively. Constants *a,* and *b* are two fitting parameters obtained from the first portion of the tracer tail in a semi-log plot.

6.4 Flow Geometry Revealed by the Tracer Response

In reservoir engineering, the concept of flow capacity- storage capacity diagram has been used to describe the heterogeneity of the formation flow and storage (Stiles, 1949; Schmalz and Rahme, 1950; Lake, 1989; Gunter et al., 1997). Shook (2003) and Shook and Forsmann (2005) have shown that the flow geometry of the fractured rock can be estimated from the tracer test data. The detail derivation process of flow capacity- storage capacity curve (F-Φ curve) from tracer data was provided in Shook and Forsmann (2005) and Shook et al. (2009).

Briefly, the calculation of F (flow capacity) and Φ (storage capacity) with constant fluid flow rate was given in EQ (6.4).

F- Φ curves are used qualitatively and quantitatively. The Lorenz coefficient (Schmalz and Rahme, 1950; Lake, 1989), defined as in EQ(6.5), is a commonly accepted parameter calculated from the F- Φ curve to quantify the flow geometry heterogeneity. Figure 6-3 shows examples of F-Φ curve with the solid line showing the ideal homogenous condition. The upper curve is for a high heterogeneity while the middle curve shows a case very close to the homogenous scenario. For example, for the pink curve, 20% of the pore volume of the fracture contributes 85% of the flow while in the middle case the same percentage of pore volume provides 29% of the flow; i.e., for the middle case, each pore volume has a similar contribution to the flow. For the ideal homogeneous condition, the Lorenz coefficient is equal to zero meaning equal volumetric flow from every incremental fracture pore volume. Larger Lorenz coefficient (Lc) indicates more heterogeneous flow profile. This value was 0.70 and 0.16 for the upper case and middle case in Figure 6-3 respectively.

In this study, the flow geometry in the fracture was analyzed with the collected tracer data. As mentioned before, two linear portions of the tracer tail in semi-log plot was observed in our Lab-scale tests with the first linear portion mainly controlled be the fracture flow. So, only the first linear portion and its extrapolation are used to calculate the F-Φ curve and corresponding Lorenz coefficient in the following sections.

$$F(t) = \int_0^t C d\tau \Big/ \int_0^\infty C d\tau \qquad (6.4a)$$

$$\Phi(t) = \int_0^t C\tau d\tau \Big/ \int_0^\infty C\tau d\tau \tag{6.4b}$$

$$L_c = 2\left(\int_0^1 Fd\Phi - 0.5\right) \tag{6.5}$$

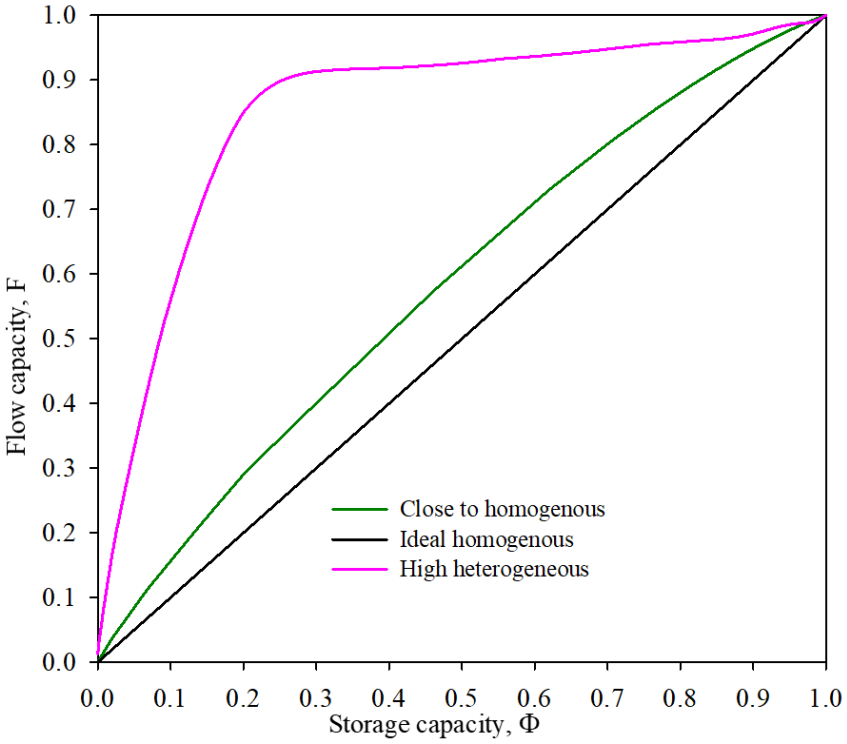


Figure 6-3. Example for the F-Φ curves with different degrees of flow geometry heterogeneity.

6.5 Test results under different fracture geometries and rocks materials

6.5.1 Case I: multi-production wells intersected by the induced fracture

Due to the heterogeneity of the granite and the stresses within the rock block, the induced hydraulic fracture during reservoir stimulation usually did not propagation equally in all

directions resulting is different fracture geometries which connect with different number of production wells. This provides an opportunity to observe the tracer response under different conditions. The first case study is for when the induced fracture intersected multiple production wells. The tracer test had three phases according to the concentration of the injection fluid as shown in Figure 6-4. Since the method of moments assumes a steady-state flow for the tracer fluid, a fluid with normal tracer concentration was injected to establish steady flow before the actual tracer slug was injected and the injection rate was 1.0 ml/min (the same injection rate was applied in all the tests discussed in this work). The injection pressure perturbation during the tracer test was mainly caused by the switching between pumps. There is no apparent large pressure drop, which indicates there is no further fracture propagation during the tracer test. During Phase #2 the injected, a solution of 1 mole/L NaCl (PPM: 58440, nearly 500 times higher than pore fluid) was used whereas in Phase #1 and Phase #3 the injected solution was 0.002 mole/L NaCl. A number of fluid samples were collected from the production well before the slug injection to obtain the background fluid concentration. Figure 6-4 shows the injection rate, pressure and the production rate during the tracer test. In this case, the hydraulic fracture intersected wells No.3 and No.4 and has come very close to Well No.2 (the reconstructed fracture geometry confirms this). Well No.3 produced most of the production fluid since the hydraulic conductivity in this direction is higher (During circulation, it produced 83% of the injected fluid) and Well No.1 had the smallest production rate since the induced fracture is about 43.2 mm (1.7 inch) away to this production well. The average production rate in the wells 1-4 was 0.04ml/min, 0.08 ml/min, 0.28 ml/min and 0.12 ml/min, respectively. It is noticed that the total production rate is 0.52 ml/min which is less than the injection rate (1.0 ml/min); this is interpreted to be dues to

fluid leaked off into the rock matrix (the induced fracture did not reach the rock boundary). Figure 6-5 (left) shows the concentration of the injection and production fluids. In Well No.3 and Well No.4, two apparent linear relationships of the trace tail are apparent on the semi-logarithmic plot (marked with red dash lines). The first one represents flow dominated by the fracture volume, pipe volume, and any unoccupied volume in the open interval of the wells, while the second straight line is due to flow back from the rock matrix. As mentioned before, this phenomenon has also observed in some field data and predicted by numerical simulations. Based on the method of moments and using the first linear section of the tracer tail, the estimated fracture volume is 3.66 ml. Figure 6-5 (right) shows the F-Φ curve calculated from the collected tracer data and its extrapolation. It indicates that the fluid flow geometry was relatively homogeneous in each calculated direction. The Lc value for well 1-4 were 0.31, 0.23, 0.21, 0.24, respectively.

After the test, the granite block was cut into slabs to reveal the fracture trace to reconstruct the fracture geometry in 3D. Figure 6-6 (top) shows one of the slabs cut through the injection well with the fracture highlighted under ultraviolet lamp (bottom). From this picture, it is clear that the induced fracture intersects Well No.4 and it is only a few millimeters away from Well No.2. The estimated fracture area from the reconstructed 3D fracture geometry is 224.5 cm^2 from which we calculate the average fracture aperture to be about 163μm. The travel time of the fluid in streamline directly connecting the injector and the producer in the fracture was also calculated (using the method of Section 2.4) to be 373.0 s, 103.0 s, 65.0 s and 325.0 s, respectively. The apparent fluid velocity flowing through the fracture was estimated to be 0.24 mm/s, 0.86 mm/s, 1.36 mm/s and 0.27 mm/s, respectively.

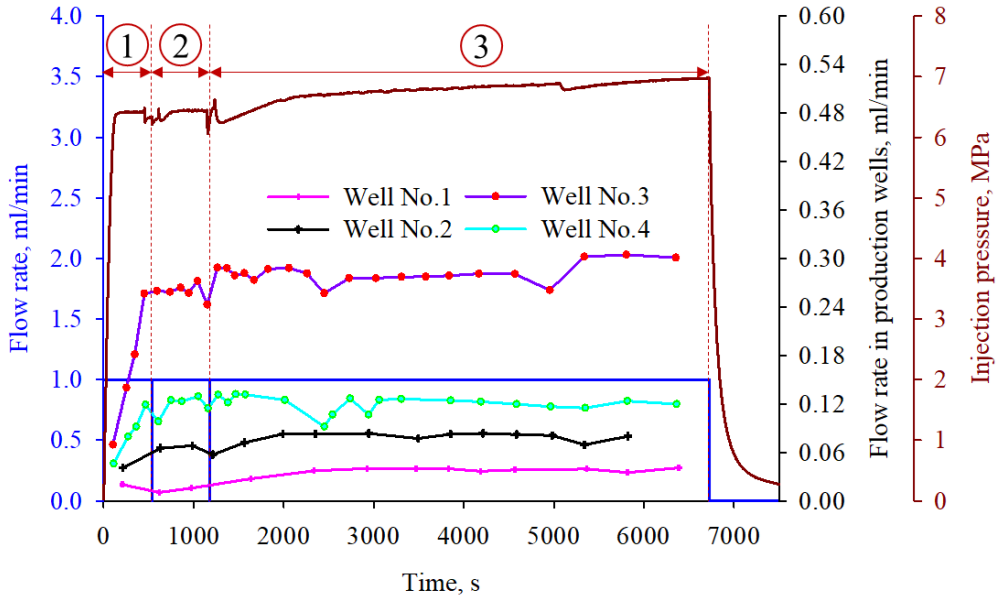


Figure 6-4. Flow rate of the injected and produced fluid and the injection pressure (Case I).

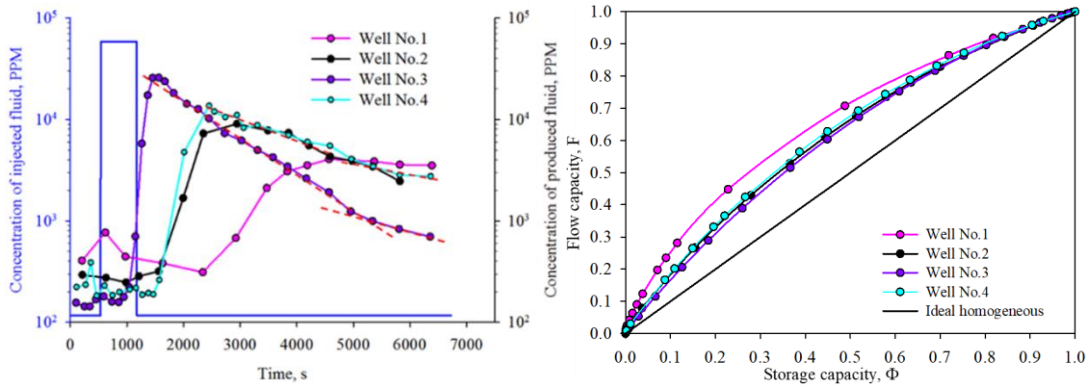


Figure 6-5. Concentration of the injected and produced fluid (left) and the corresponding F-Φ curves (right) (Case I).

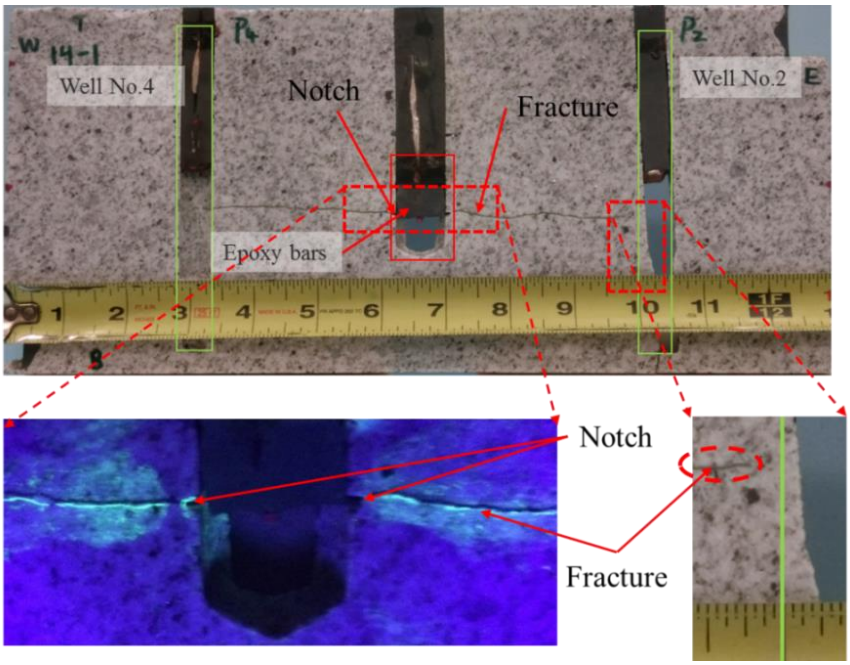


Figure 6-6. Fracture on slab surface (left) and reconstructed fracture (right) (Case I).

6.5.2 Case II: Only one production well intersected by the induced fracture

For the second case study, the induced fracture reached the rock surface and the tracer test was conducted using the same procedure as Case I. However, fluid production rates from Wells No 3 and No 4 were too small for measurement (a couple of drops over the whole tracer test), so only fluid produced from Well No.1 and No.2 were collected and analyzed. The average production rate in Well No.1 and No.2 was 0.24 ml/min and 0.03 ml/min, respectively as shown in Figure 6-7. In this case, the total fluid recovery rate is 0.27 ml/min, and the balance fluid mainly leaked-off into the rock matrix and a small amount (5-6%) of fluid could have been lost to the into the frame. Figure 6-8 shows the concentration of the injection and production fluid. For Well No.1 two apparent linear relationships of the trace tail can be seen on the semi-logarithmic plot. Because the test was stopped after about 110 minutes, the second linear tracer tail in is not observed in Well No.2. Based on the method

of moments and the first linear relationship of the tracer tail, the estimated fracture volume is 4.8 ml. The F-Φ curve calculated from the collected tracer data and its extrapolation was shown in Figure 6-8 (right), which suggests that the geometry was relatively homogeneous in directions towards Well No.1 and No.2 with The Lc value of 0.14 and 0.19, respectively. As in Case I, the tested block was cut into sable to reveal the hydraulic fracture. Figure 6-9 shows one of the slabs (top) through the injection well. It is clear that the induced fracture intersects Well No.1. In Figure 6-9 (bottom) the slab with Well No.2 is visible; it can be seen that the induced fracture did not intersect the well but passed underneath it. The fracture area was calculated to be 344.7 cm^2 from the reconstructed fracture geometry, and was used to estimate the fracture width from the fracture volume obtained from the tracer test. The estimated fracture width is about 139 μm with the fracture volume (4.8 cm^3) estimated from method of moments. The travel time of the fluid in streamline directly connecting the injector and the producer in the fracture for Well No.1 and Well No.2 was also calculated to be 52.0 s and 424.0 s, respectively and thus the apparent fluid velocity through the fracture was estimated to be 1.71 mm/s and 0.21 mm/s, respectively.

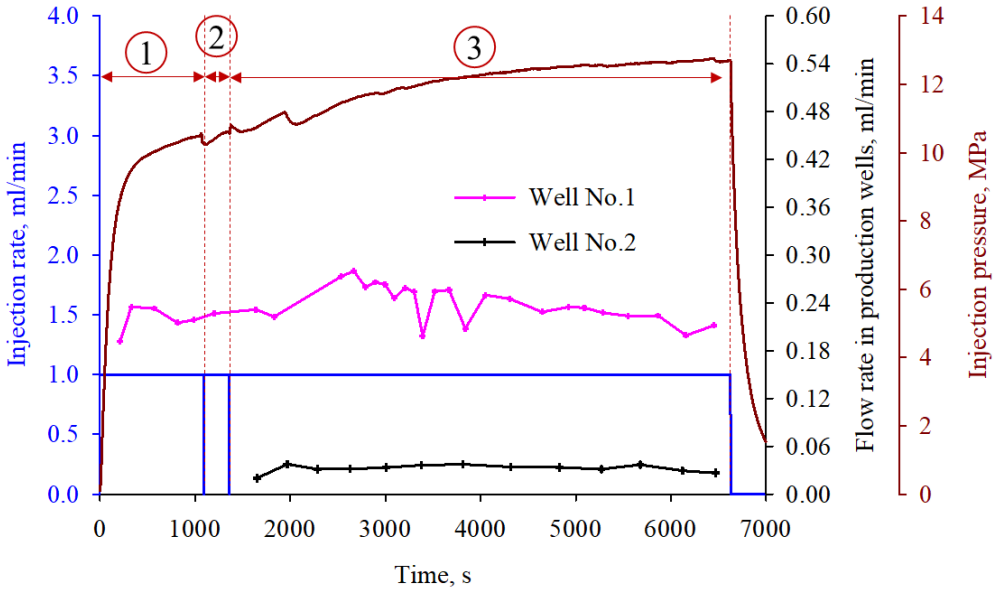


Figure 6-7. Flow rate of the injected and produced fluid and the injection pressure (Case II).

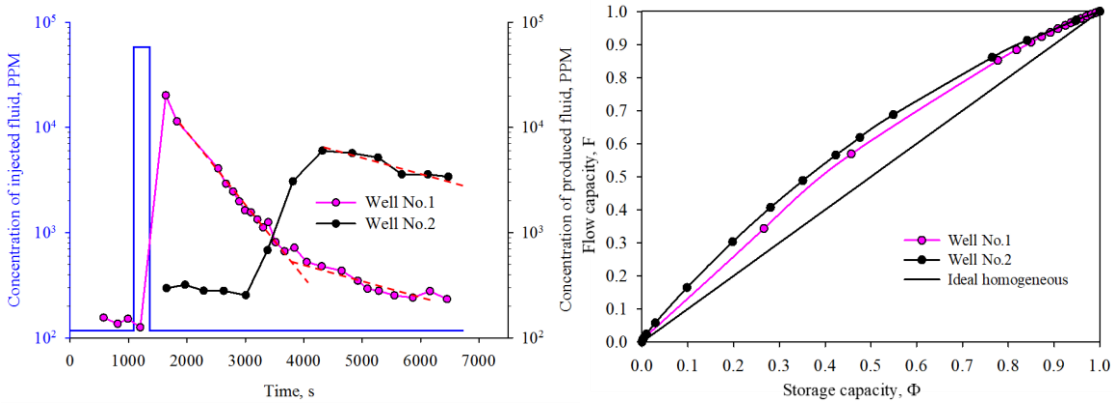


Figure 6-8. Concentration of the tracer and produced fluid (left) and the corresponding F-Φ curves (right) (Case II).

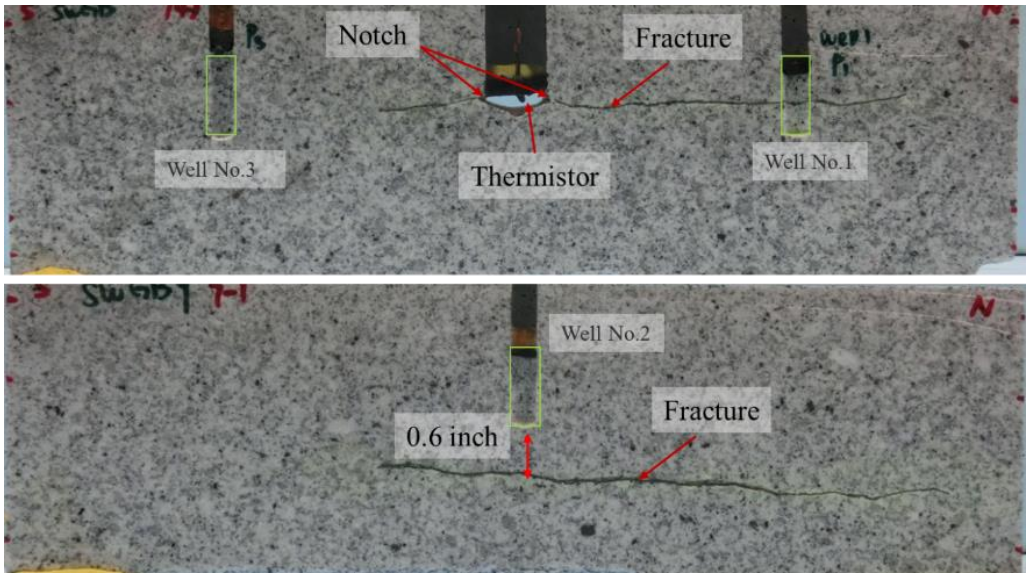


Figure 6-9. Fracture on slabs at the center (top) and at Well No.2 (bottom) (Case II).

6.5.3 Case III: Test Result with Raven Noir Gabbro

The last case study is a test conducted using a hydraulic facture created in a block of Raven Noir gabbro. As mentioned before, this igneous is very tight with near zero porosity and permeability. The induced hydraulic fracture intersected all the production wells and it was constrained within the block. Details of the stimulation test and circulation tests on this block can be found in Hu and Ghassemi 2018b.

The tracer test was conducted in the same way described previously. Figure 6-10 provides the injection and production data; it can be seen that Well No.3 dominated the production during tracer test as it did during the circulation test even though all production wells were connected by the induced fracture. The production rates for the four wells were 0.05 ml/min, 0.12 ml/min, 0.75 ml/min, and 0.08 ml/min. Because the rock matrix is almost non-porous and the induced fracture was contained within the rock block, all the injected fluid was produced. Unlike the test in Sierra White granite, the second linear tracer tail on the semi-

logarithmic plot is not observed (Figure 6-11) because of the nearly zero permeability of the tested rock. Based on the method of moments, and the first linear relationship of the tracer tail, the estimated fracture volume is 8.6 ml. Figure 6-11 (right) shows the F-Φ curve calculated from the collected tracer data and its extrapolation. It indicates that the fluid flow geometry was relatively homogeneous in each calculated direction. The Lc value for well 1-4 were 0.10, 0.04, 0.07, 0.17, respectively.

Figure 6-12 shows the picture of a slab from the block with the fracture visible. It is clear that the induced fracture initiated from the notch in the injection well and propagated to intersect wells No. 2 and No.3. The fracture surface estimated from the reconstructed geometry is 491.6 cm^2 and thus the fracture width is estimated to be about 174 μm. The travel time of the fluid in stream line directly connecting the injector and the producer in the fracture for wells 1-4 is calculated to be 47.0 s, 78.2 s, 1.2 s and 40.3s, respectively and thus the apparent fluid velocity flowing in the fracture is estimated to be 1.89 mm/s, 1.14 mm/s and 74.1 mm/s, and 2.2 mm/s, respectively (see Table 6.2 for comparison).

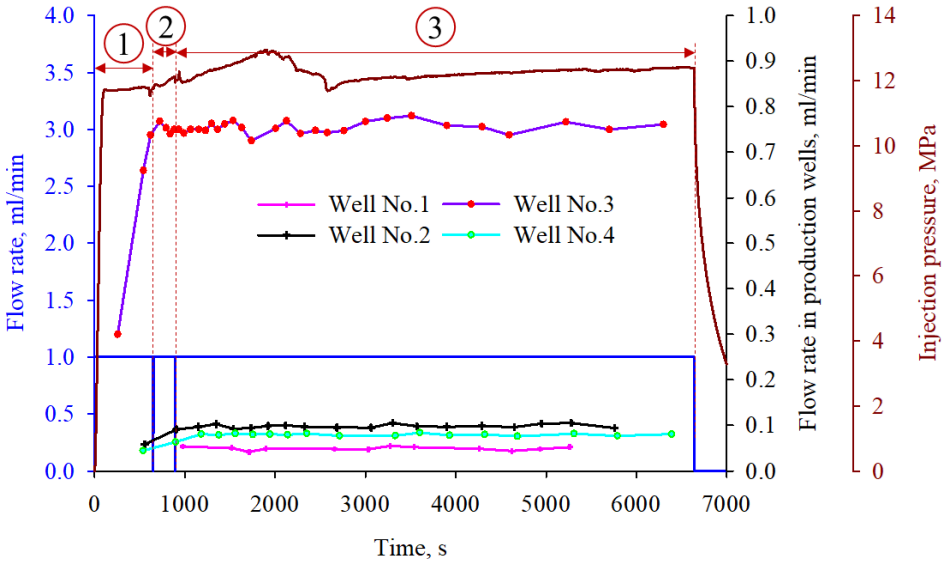


Figure 6-10. Flow rate of the injected and **produced fluid and the injection pressure (case III).**

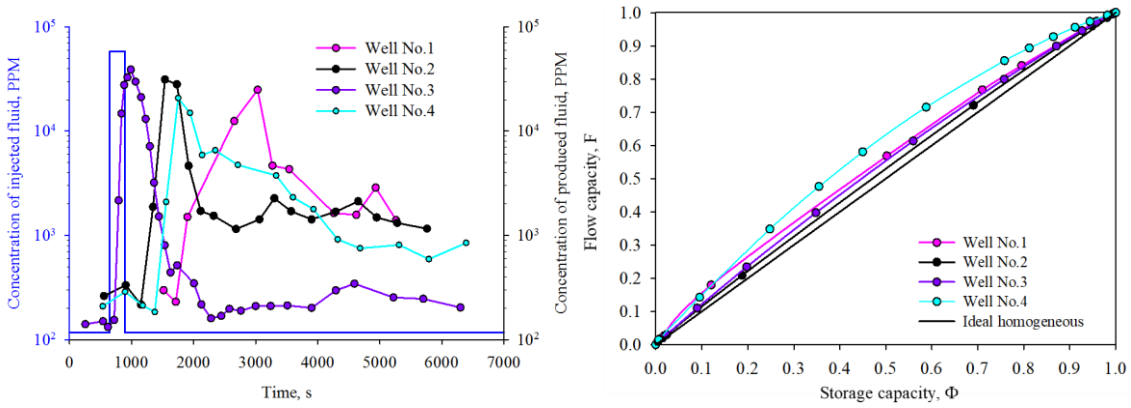


Figure 6-11. Concentration of the tracer fluid and produced fluid (Case III).

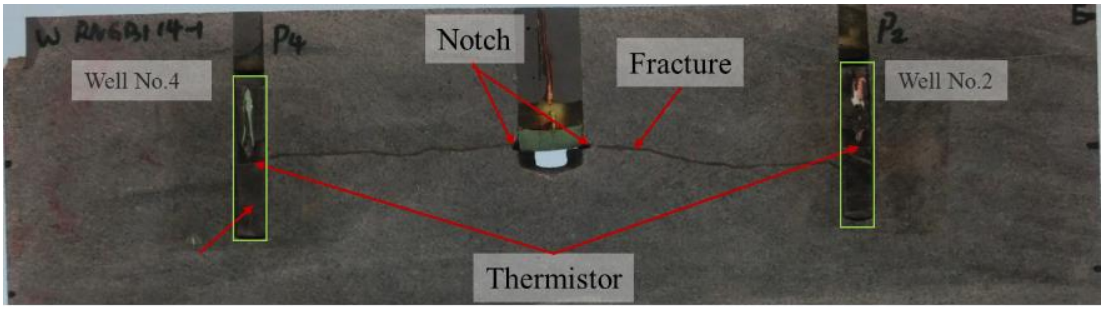


Figure 6-12. Fracture trace on slab at the center (Case III).

6.6 Conclusions and Discussion

A series of lab-scale tracer test has been carried out in rock block that were hydraulically fractured to replicate future EGS development. Two kinds of igneous rocks with different texture and permeability were tested. The Sierra White granite has a matrix permeability of about 700 nD while the Raven Noir gabbro has zero permeability. The tracer used was 1.0 mole/liter sodium chloride (NaCl) solution and was injected as a slug. The tracer fluid was collected from the production wells after flowing through the hydraulically induced fracture under continuous injection from the central injection well. The three cases involved different induced hydraulic fracture geometries.

During circulation of the tracer, electrical conductivity of the fluid produced from the production wells was analyzed to determine the tracer concentration. For the relatively permeable granite, the calculated tracer curves show two linear portions of tracer tail in semi-log plot, while for the nearly impermeable gabbro only one linear portion was observed in the tracer tail. This difference is attributed to the tracer leaking into the rock matrix in the case of the granite and produced back at the late phase of tracer test. The flow geometry analysis using F-Φ curves from the tracer response shows that the fracture flow geometry to be relatively homogeneous in the measured directions. This can be attributed to the relatively simple fracture geometry with small tortuosity: a nearly horizontal fracture connecting the wells. However, the impact of fracture roughness on the fluid flow geometry still is evident. The fracture with a lower roughness experienced more homogeneous flow (lower Lorenz coefficient). For example, the roughness of the induced fracture in the gabbro was smaller (joint roughness coefficient of 11.16) compared to that of the Sierra White granite (12.98).

The average Lc coefficient in the gabbro block fracture was about 0.1 and in Sierra White granite fracture it was 0.26.

Table 6.2. Fluid velocity obtain fracture tracer tests.

	Production rate, ml/min				Calculated fluid velocity, mm/s			
	Well 1	Well 2	Well 3	Well 4	Well 1	Well 2	Well 3	Well 4
Case I	0.04	0.08	0.28	0.12	0.24	0.86	1.36	0.27
Case II	0.24	0.03	-	-	1.71	0.21	-	-
Case III	0.05	0.12	0.75	0.08	1.89	1.14	74.1	2.2

Table 6.2 lists the calculated fluid velocity in the fracture for all tracer tests discussed before. The time variation of tracer arrival in different flow direction reflects the hydraulic conductivity in the corresponding direction. The fluid velocity in the fracture was calculated using the tracer travel time and the distance between the injection and production wells. The maximum fluid velocity observed is 74.1 mm/s with a production rate of 0.75 ml/min. However, it is found that the calculated fluid velocity does not have a proportional relationship with the production rate in all cases. For example, in Case I, the production rate in Well No.4 is three times that of the Well No.1 (0.12 ml/min vs 0.04 ml/min) while the calculated fluid velocity in these two directions is similar (0.27 mm/s VS 0.24 mm/s). The main reason is that the tracer concentration in the production wells was not obtained continuously in time, rather it was obtained from discrete data points (collecting more than 0.2 g of fluid at different intervals) and thus there are avoidable errors in the tracer arrival time. The true fluid velocity estimated from the fluid volumetric rate and the injection pressure and modeling is of the order of 10 mm/s under the test condition and thus the calculated velocity from the tracer test is about one order smaller except for the result from Well No.3 in Case III. Moreover, the calculated average fracture aperture based on the tracer

test result is around 150 μm which is about two orders higher than the fracture aperture estimated from the cubic law (about two micrometers). Numerical modeling (for the same blocks discussed herein) has shown that the average fracture aperture of about several micrometers provides a good match with experimental data (Gao and Ghassemi, 2019). Though the cubic law tends to underestimate the real fracture aperture, the actual fracture in the tracer test should be less than 150 μm. The apparent overestimation of the aperture from tracer data in the lab-scale lies in the small-scale of the fracture volume. In the field, the fracture aperture, volume, and tracer travel time are on order of millimeter, cubic meter, and a month, respectively. In comparison, in the lab-scale, these parameters are of order of micrometer, 10^{-8} cubic meter, and second respectively. In addition, the flow rate in lab scale is much small than field case, which introduces considerable difficulty on taking samples. In lab-scale, the sampling rate has to be small to obtain enough fluid for measurement while in field this time may just be a few seconds. However, as the first lab-scale tracer test, what we obtained was promising. The existing of two linear tracer tail was observed in Sierra White granite test and tracer result does show a good correlation between hydraulic conductivity and the tracer concentration response. The impact of rock texture was observed. What's more, the test result could provide some useful guide for future lab-scale tracer test deign. Low permeability rock is recommended for tracer test to minimize leakage of tracer fluid into the rock matrix and also improve the fluid recovery. Low injection rate will increase the tracer time the in the fracture while proper tracer candidate with low-concentration detectability is required.

7. Slippage of a Natural Fracture Resulting from an Approaching Hydraulic Fracture

7.1 Test setup and Test Procedures

In this Chapter, the slippage of a natural fracture due to the induced stress caused by an approaching hydraulic fracture was investigated in experimental rock. The analog experiments were conducted with 101.6 mm (4.0 inches) diameter cylinders with a polished, inclined saw-cut joint surveying as a natural fracture. The cylinders have a height of about 152.4 mm (6.0 inches). The saw-cut joint surfaces were polished by 600 grit sand paper to lower the frictional angle. This work includes the results from four samples: one PMMA cylinder, two shale sample and one Sierra White granite sample. Both of the two shale cores were provided by Devon Energy Corporation. The inclined natural fracture (polished saw-cut joint) was loaded to a near critical stressed condition before fracturing. Hydraulic fracture was induced by injecting oil into a horizontal well with a vertical notch. Injection pressure, stresses, and acoustic emission are monitored during the test. In addition, strain gauges are used to measure the slippage on the natural fracture. The slippage of the natural fracture could be demonstrated by the axial stress drop, acoustic emission activities, and direct measurement of the sliding.

Figure 7-1 (left) shows the layout of the tested samples. A horizontal well was drilled about 55.9 mm (2.2 inches) -deep into the sample. The wellbore was notched near the bottom (at 50.8 mm/2.0 inch) to create a starter crack to lower the breakdown pressure and to provide for a less complex fracture geometry. Injection tubing was installed in the wellbore and the annulus between the injection tubing and the wellbore was filled with epoxy leaving a 7.6 mm (0.3 inch) open interval at the bottom for fracturing. During the test, confining pressure

is applied as the minimum principal stress, thus a vertical fracture perpendicular to the wellbore is expected to be generate from the notch. The diameter of the wellbore in the PMMA and shale/granite samples were 12.7 mm (0.5 inch) and 20.3 mm (0.8 inch), respectively.

The testes were carried out on using the MTS 315 loading system in the Reservoir Geomechanics & Seismicity Research Group's Laboratory. Strain gauges were installed on the sample to measure the relative displacement (slippage) of the joint surfaces (as shown in Figure 7-1 (right)). The strain gauges were attached in a way that only the two ends were glued on the sample surface and it was in slight tension. During the test, when the upper part of the cylinder slides downward relative to the lower part, the strain gauge is stretched allowing the measurement and then calculation of the shear displacement. For the test on rocks, an extra strain gauge was attached in the same way on the upper part of the cylinder perpendicular to the plane of the potential hydraulic fracture as shown in Figure 7-1 (right) so that the strain gauge will across the fracture path on the sample surface. For easier installation, large strain gauges with 50.00 mm grid length were used. Acoustic Emission sensors with resonance frequency of 500 kHz (0.25 inch in diameter) were glued on the sample surface for acoustic emission monitoring.

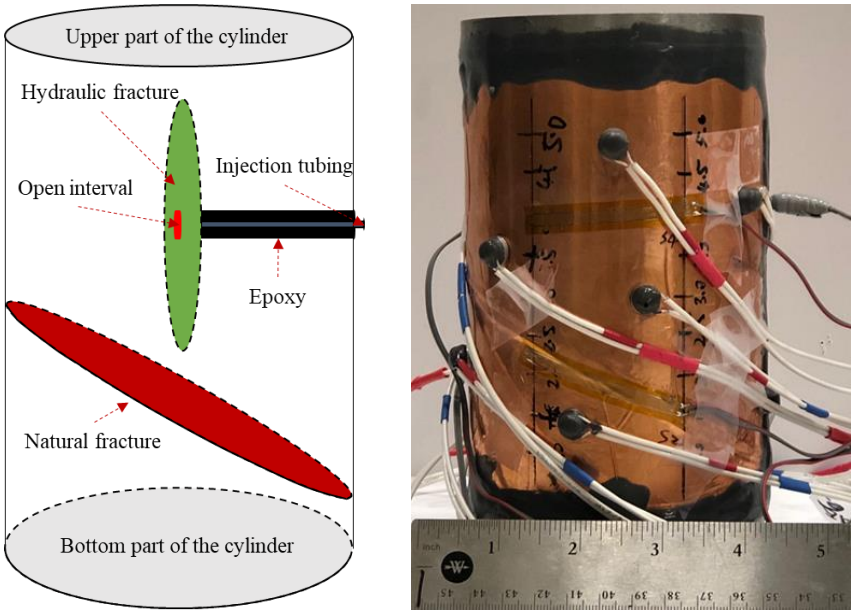


Figure 7-1. Schematic of the sample layout (left) and a prepared sample ready to be tested (right).

After a sample equipped with AE sensors and strain gauges was assembled into the MTS 315 with the frame chamber full of confining oil, the signal quality of the AE sensors, the strain gauges and load cell was rechecked. And then, the predetermined confining pressure was applied and maintained constant. A deviatoric stress was applied manually with displacement control of 0.01 mm displacement increment until a peak load was reached. The frictional angle was obtained from the peak load, confining pressure and inclination angel of the natural fracture based on Mohr-Coulomb criterion. Then, the sample was reloaded to a near critical stress condition. The fracturing fluid (mineral oil) was then injected into the wellbore the create the fracture while the applied deviatoric stress, strain, the injection pressure and acoustic emission were recorded. After breakdown, the injection was continued for some time (usually about one minute). The induced fracture on the sample surface was observed and recorded after the completion of the test.

7.2 Calculation of the slippage on the natural fracture

As mentioned before, the slippage on the natural fracture was measured by stain gauges. However, the output of the strain gauges, is our case, was the its stretch. Necessary assumption and calculation is required to obtain the slippage of the natural fracture. As shown in Figure 7-2, a x-y coordinate system is established on the surface of the cylindrical sample and the red dash line indicates the location of the smooth natural fracture. Points A on the lower part of the sample and Point B on the upper part of the sample represent the two ends of the strain gauge, respectively. Since during the tests, either the loading was small or the drop of the deviator stress was small, it is assumed that the measurement from the strain gauge across the natural fracture was mainly controlled by the slippage of the natural fracture. With this assumption, the location of Point A is fixed while Point B moves downwards to Point B' parallel to the natural fracture surface when the slippage of the upper part of the sample occurs. The distance between Point A and point B' is calculated with the initial distance between Point A and Point B and the elongation of the strain gauge as shown in Eq.(7.1a). The parallel movement of Point B related the natural fracture can be mathematically descried as Eq. (7.1b). With these two equations, the coordinate of Point B' can be solved and then the slippage is obtained as the distance between Point B and Point B'.

$$\sqrt{\left(x_A - x_{B'}\right)^2 + \left(y_A - y_{B'}\right)^2} = (1+\varepsilon)\sqrt{\left(x_A - x_B\right)^2 + \left(y_A - y_B\right)^2} \tag{7.1a}$$

$$\frac{y_B - y_{B'}}{x_B - x_{B'}} = \tan(\alpha) \tag{7.1b}$$

Where, (x_A, y_A) and (x_B, y_B) are the original coordinates of Point A and Point B, respectively while $(x_{B'}, y_{B'})$ is the new coordinates of Point B after slippage; ε is the strain reading from the strain gauge; α is the inclination of the natural fracture.

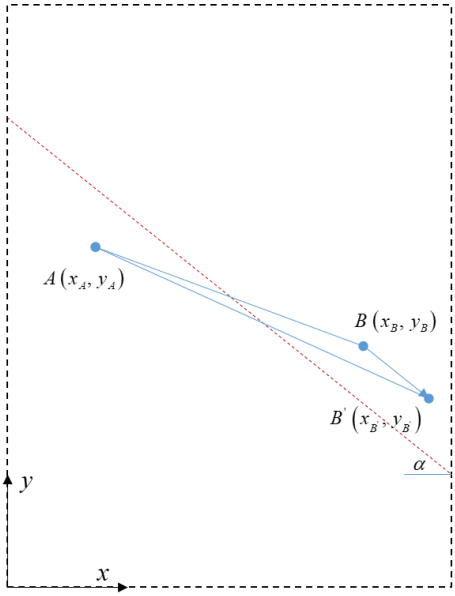


Figure 7-2. The coordinate system on the sample surface and the coordinated of the ends of the strain gauge before and after slippage.

As mentioned before, an extra strain gauge was attached in the same way on the upper part of the cylinder perpendicular to the plane of the potential hydraulic fracture. Before the fracture reaches the sample surface, this reading is caused by the deformation of the rock resulting from the formation and opening of the hydraulic fracture. After the fracture reaches the sample surface, the reading can reflect the aperture of the hydraulically induced fracture. Therefore, this strain gauge reading was converted to deformation across the fracture on the sample surface with the strain gauge length.

7.3 Test Results

The slippage of a natural fracture resulting from an approaching hydraulic fracture was investigated with the experimental setup and procedures with different materials including PMMA and rock. Table 7.1 lists the tested materials, basic material properties and test conditions. The frictional angel of the PMMA sample was measured from 25.4 mm (1.0 inch) diameter sample while this parameter for other samples was determined during the loading process before fracturing as described in Section 7.1. The experimental results and observations from these samples will be given and analyzed in the following subsections in detail.

Table 7.1 Basic rock properties and loading condition of the tested shale sample

Sample	Elastic modulus GPa	Poisson's ratio	NF inclination, degree	NF friction angle, degree	Confining pressure, MPa	Deviatoric stress, MPa
PMMA	2.45	0.375	31.1	15.6	4.1	3.3
Thistle shale	63.5	0.25	44.9	14.8	3.4	2.1
Janis shale	57.0	0.22	32.1	20.8	10.3	20.1
Granite	68.2	0.27	45.4	19.7	6.9	7.0

Note: the elastic modulus and Poisson's ratio for shales were dynamic value.

7.3.1 Case I: Test Result with PMMA

For the PMMA cylinder, the horizontal injection well was drilled for fracturing. A notch was created 5.08 mm (0.2 inch) above the wellbore bottom to lower the breakdown pressure and guide the fracture initiation. And then the cylinder was cut into two pieces with a line saw at 31.1 degrees with the horizontal. Both cutting surfaces were polished with 600 grit sand papers to lower the frictional coefficient. The two parts were put back together and sealed from the confining fluid. AE sensors and the strain gauges were glued on the sample surface.

The PMMA cylinder with a smooth 31.1^{o} inclination smooth joint was subjected to a confining pressure of 4.1 MPa (600 psi) and a deviatoric stress of 3.3 MPa (485 psi). These provide for a near critical condition (the friction angle of the smooth joint was measured to be 15.6^{o}, and the elastic modulus of PMMA is about 2.45 GPa). The injection rate was constant and equal to 0.1 ml/min. The recorded stress, injection pressure, acoustic emission activity and calculated slippage during the experiment are shown in Figure 7-3. During the early stage of injection, the deviatoric stress showed a slight decrease with increasing displacement across the joint and relaxation of the sample. A breakdown pressure of 26.2 MPa (3800 psi) was observed after 1023 s of injection. At breakdown, sliding was detected with increased AE activity, as well as sudden drop of the deviator stress and a displacement jump across the joint (see Figure 7-3 and Figure 7-4). Note that the stress, strain, AE and the injection pressure and flowrate were recorded using three different computers, so the manual synchronization is imperfect (error is less than 1 second). Another evidence of joint slippage is the fact that after breakdown the stress drop did not fully recover and that the increased displacement did not return to the original trend. However, the peak displacement does include contributions from the joint slippage and the deformation of the solid caused by the induced hydraulic fracture. The slippage on the joint is estimated to be 0.009 mm with a stress drop (at breakdown) of about 0.14 MPa (20 psi).

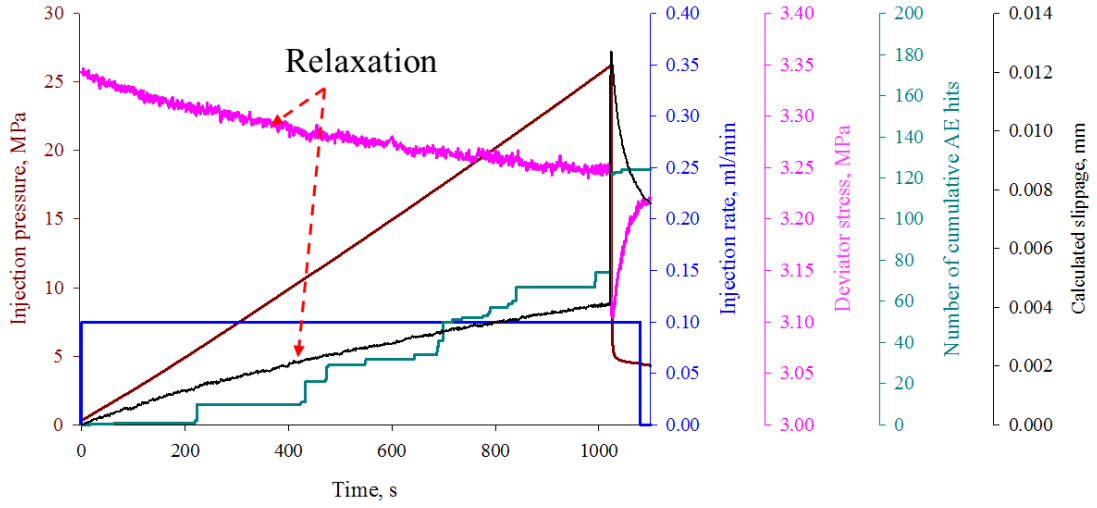


Figure 7-3. Recorded data during the test: AE activity jump and displacement jump was observed (PMMA).

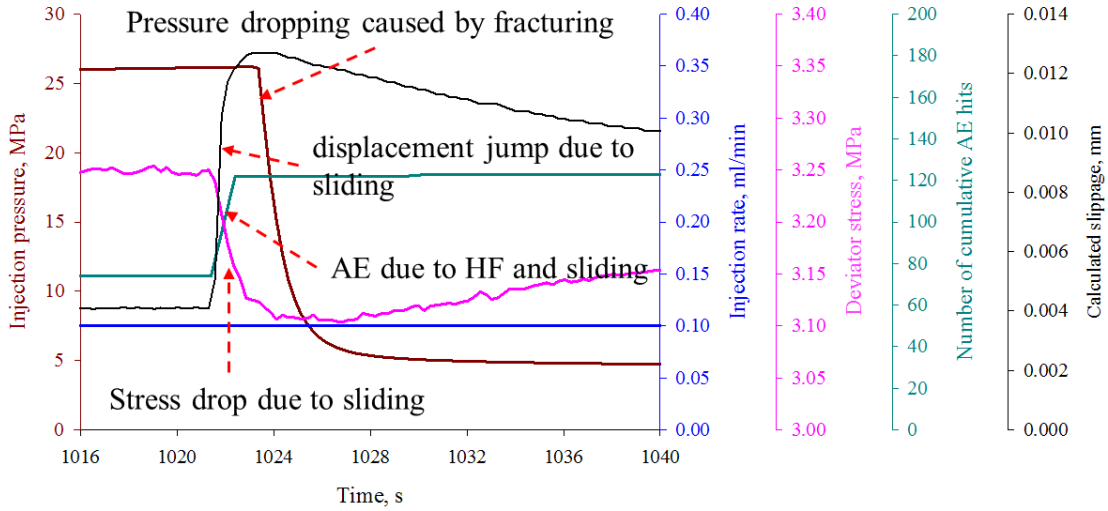


Figure 7-4. Recorded data near the pressure breakdown (PMMA).

Figure 7-5 provides the top view (left) and side view (right) of the sample after testing. It is noticed that the hydraulic fracture initiated at the notch and did not intersect the joint. The fracture did not propagate equally in every direction due to the notch heterogeneity; it propagated more to the right side (in Figure 7-5 left) and eventually reach the sample surface.

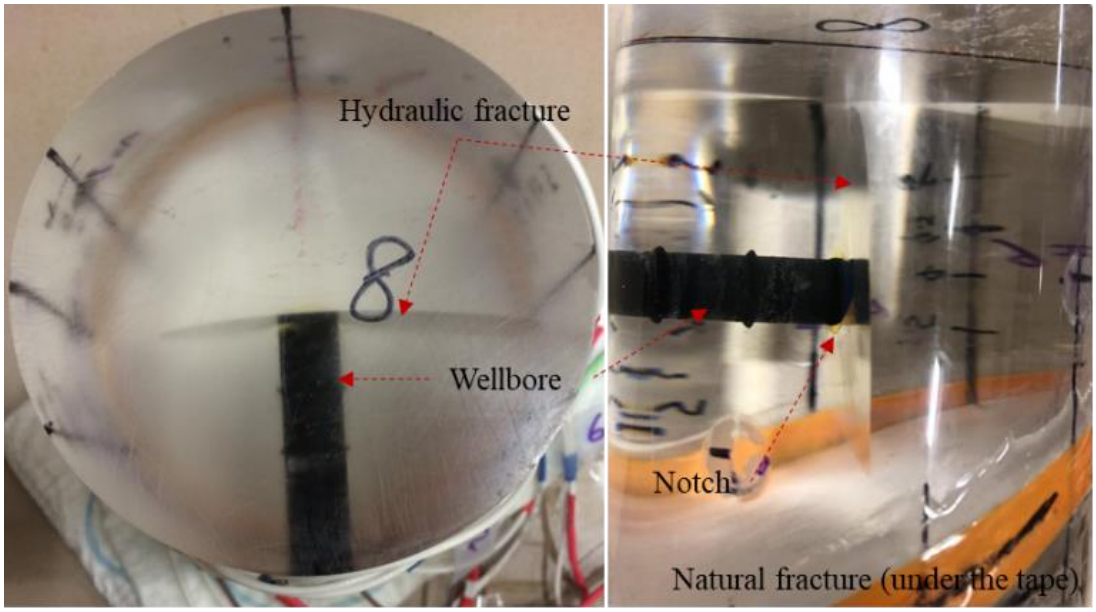


Figure 7-5. Top view and side view of the test sample with hydraulically induced fracture visible.

7.3.2 Test result with Shale Core: Thistle

The Thistle shale cylinder has a 45^{o} smooth saw-cut joint serving as a natural fracture. As mentioned before, two extra strain gauges were glued on the upper part of the cylinder across the potential hydraulic fracture trace on the cylinder surface to detect the deformation caused by the hydraulic fracture. The confining pressure was 3.4 MPa (500 psi) and the deviatoric stress was 2.1 MPa (303 psi), which provide for a near critical condition (the friction angle of the smooth joint is around 14.8 degree). The injection rate was set to a constant 1.5 ml/min. The time variations of the recorded stress, injection pressure, acoustic emission activity, calculated slippage and the fracture opening on the side surface (assuming that the rock matrix deformation is negligible due to its high elastic modulus- the dynamic elastic modulus of the shale is as high as 63.5 GPa) are plotted in Figure 7-6 and Figure 7-7. Based on the record of the deviatoric stress, slippage on the joint and the injection condition, the

whole test period can be divided into six phases as marked in Figure 7-6 and Figure 7-7. During Phase #1 (before fracturing), the deviator stress and the calculated displacement are nearly constant. This is because the shale sample has a much higher elastic modulus than the PMMA, so no apparent stress relaxation is observed. During Phase #2 (fracture initiation and a slight/stable propagation), the hydraulic fracture initiated and propagated a small distance away from the notch. Displacements increased with a larger value for the displacement across the joint (slippage). This is because the hydraulic fracture did not reach the cylinder surface and the joint surface, so the deformation on the cylinder surface remained small while some slippage on the joint was detected. The stress drop is about 0.14 MPa (20 psi) which is similar to that for the PMMA case at breakdown when the hydraulic fracture still is contained in the intact part of the sample. During Phase #3, the hydraulic fracture propagated to reach the joint while still contained in the sample's top piece. Both displacements show a great increase. The displacement increase across the joint indicates more slippage on the joint while the displacement increase across the potential fracture trace on the cylinder surface indicates the fracture opening in the rock matrix. Then, joint sliding stopped during Phase #4 as the stress dropped to a stable level at the end of Phase #3. It is likely that half way through Phase #4, the hydraulic fracture attained its maximum aperture as it reached the cylinder surface. It is reasonable that the fracture would reach the joint first before reaching the cylinder surface because the distance between the joint and the notch tip is about 11.0 mm shorter than that between the cylinder surface and the notch tip. After the pore pressure inside the joint increased to a certain level due to the inflow of the injected oil, the effective stress on the joint was lowered (the lubrication effect of the oil on the joint may also make some contribution), and further slippage was triggered. Thus, in Phase #5, more

slippage was observed while the displacement across the fracture slightly decreased due to the decreasing pore pressure in the induced fracture. The slippage reaches its peak before the injection is ceased. During Phase #6 (injection termination), no further stress drop was recorded as the joint stress condition dropped to a stable condition during the previous phase. Since the pore pressure inside the hydraulic fracture decreased by the loss of fluid from the fracture, the fracture aperture decreased. So, the displacement across the fracture dropped slightly. During this test, before hydraulic fracturing reached the joint (close to the end of Phase #3), the slippage on the joint surface was about 0.11 mm with a stress drop of about 0.6 MPa. Both of these two values are much higher than the values obtained from the PMMA test. This is due to the fact that the applied stress condition was close to the critical condition and the hydraulic fracture initiated from a closer distance to the joint.

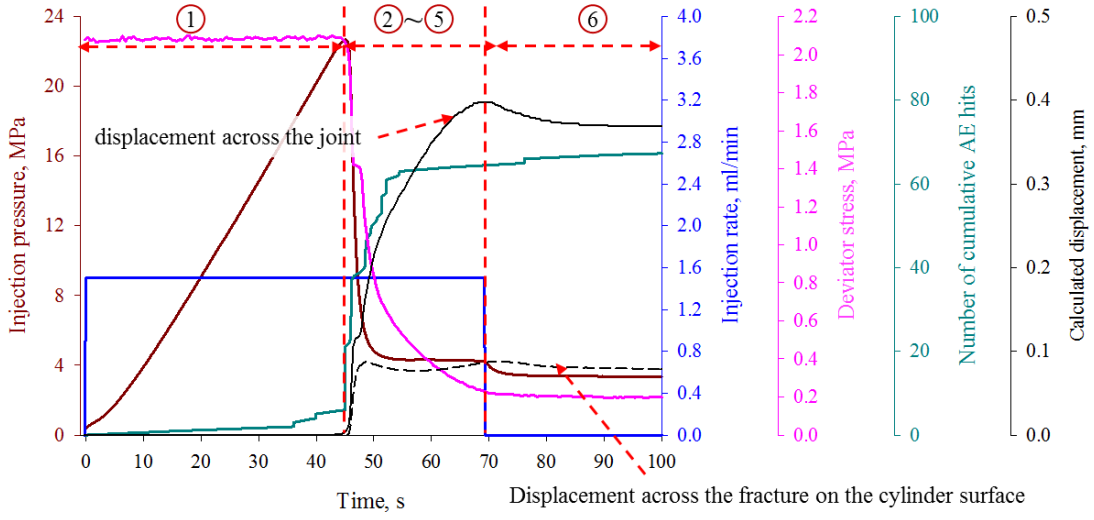


Figure 7-6. Recorded data during the test: AE activity jump and displacement jump was observed (Thistle).

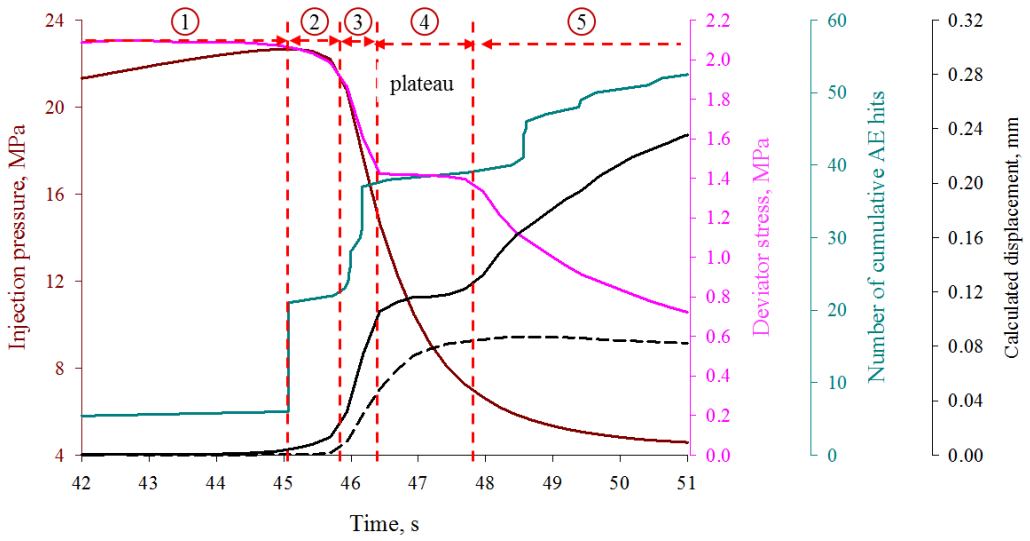


Figure 7-7. Recorded data near the pressure breakdown (Thistle).

Since the test was conducted with a well-polished joint and the applied confining pressure was relatively small, only one high energy acoustic emission event was localized near the natural fracture surface with amplitude of 80 dB. The average polarity of the received hits associated with this event shows that this is a shear/mix-mode event (Stoeckhert et al, 2015). It should be emphasized that many hits were recorded that which could not be located and/or where determined to be associated with fracture initiation from the notch and local de-bonding of the epoxy in the wellbore.

Post-mortem inspection of the sample revealed the fracture trace on both sides of the upper piece, i.e., on the cylinder's top surface and the joint surface as shown in Figure 7-8. This shows that the hydraulic fracture eventually cut the upper part of the cylinder into two pieces. In Figure 7-8, some natural fractures are visible, and the hydraulic fracture is seen to have cut through two planar features right before it reached the saw-cut joint. The HF/NF interaction resulted in a complicated hydraulic fracture geometry near the joint. One interesting observation is the offset of the HF marked by the red ellipse in the right picture:

when the hydraulic fracture reached the near horizontal bedding marked by a red dashed line, it did cross it via a small jog and continued to propagated along its original direction before being arrested again by the joint.

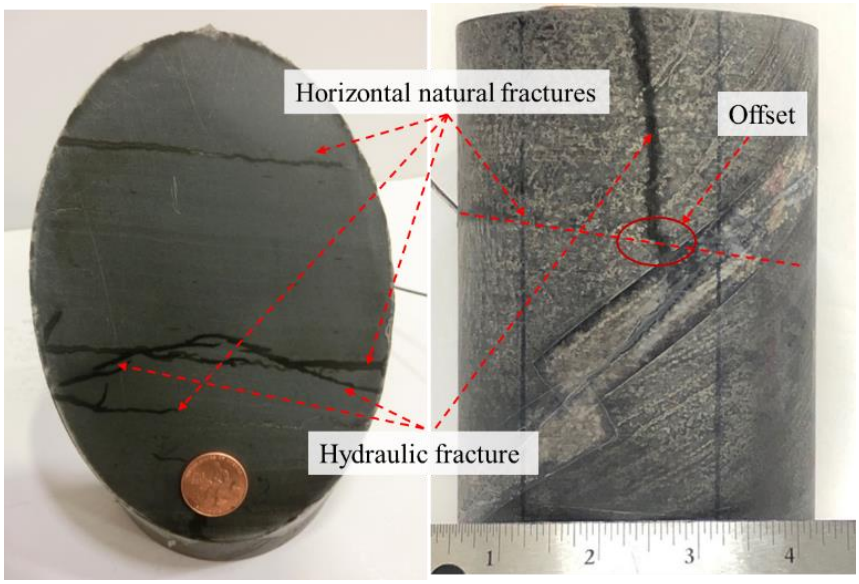


Figure 7-8. Observation of the fracture trace on the cylinder surface (Thistle).

7.3.3 Test result with Shale Core: Janis

The Janis shale cylinder had a 32° smooth saw-cut joint serving as a natural fracture. The confining pressure was 10.34 MPa and the deviatoric stress was 20.08 MPa, which provides the natural fracture for a near critical loading condition (the friction angle of the smooth joint is around 20.8 degree). The injection rate was set to a constant 0.2 ml/min. As in Thistle shale case, the recorded data are plotted in Figure 7-9 and Figure 7-10. Since the side surface of the shale sample had a dents from coring, vacuum grease was applied on the rock sample after the surface was polished to help transmit the acoustic emission from the rock sample to the AE sensors attached on the sample jacket. Unexpectedly, the vacuum grease had

impact on the reading of the strain gauge especially after the induced hydraulic fracture reached the sample surface. Based on the record of the deviatoric stress, slippage on the joint and the injection condition, the whole test period can be divided into three phases as marked in figures. During Phase #1 (before fracturing), the calculated displacements were nearly constant while the deviator stress dropped about 0.15 MPa due to the stress relaxation under high stress condition and/or slight sliding. During Phase #2 (fracture initiation and propagation), the hydraulic fracture initiated and propagated reaching the side surface and near the natural fracture. Displacements increased, with a larger value for the displacement across the joint (slippage). The injection rate was reduced 99 percent after the breakdown was observed (maintaining the fracture within the rock sample was not achieved). The stress drop is about 0.24 MPa which is similar than the previous test (during Phase #2) at breakdown when the hydraulic fracture still is contained in the sample. During Phase #3, the injection rate was increased step by step to extend the fracture to the joint. However, no further fracture propagation was observed. Since more fluid flowed outside the sample (but still inside the jacket), the strain reading across the natural fracture was no longer meaningful. No considerable stress drop was observed in this time period.

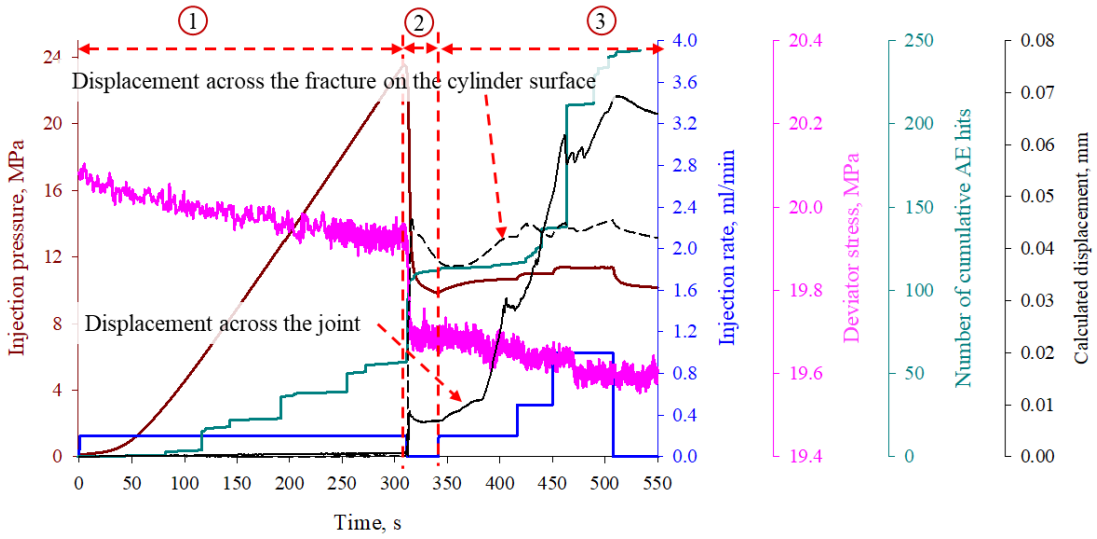


Figure 7-9. Recorded data during the test: stress drop, AE activity jump and displacement jump was observed (Janis shale).

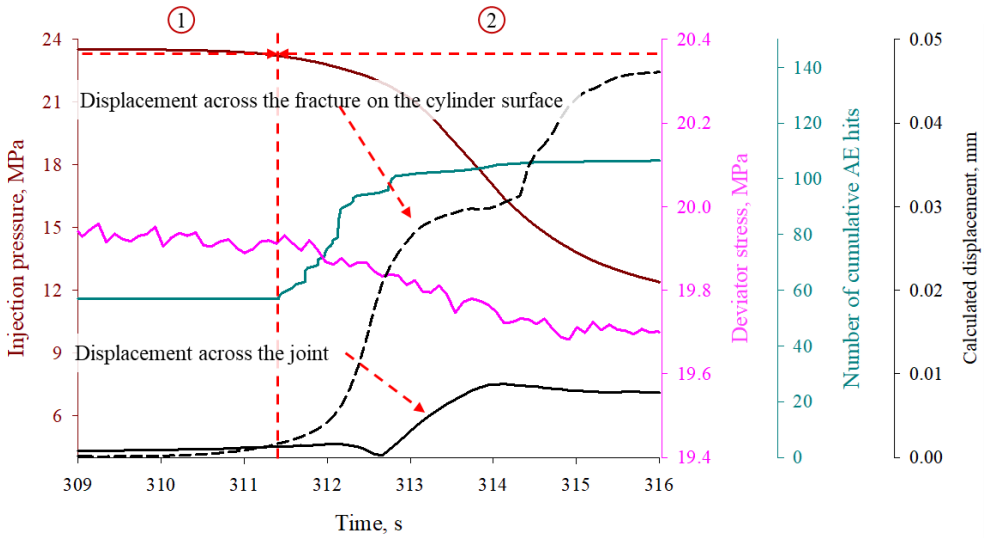


Figure 7-10. Recorded data near the pressure breakdown (Janis shale).

During the whole test, only a few acoustic emission events were localized as shown in Figure 7-11. The relative location of the AE event and the natural fracture indicates that three of these located events were due to the fracture initiation and propagation while one event was generated from the slippage of the natural fracture. It should be emphasized that many hits were recorded that which could not be located.

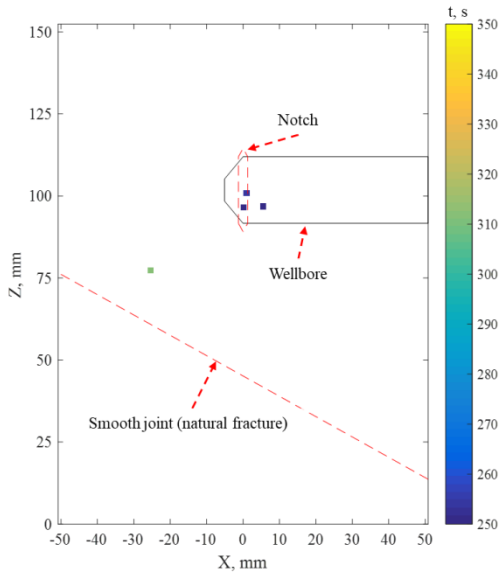


Figure 7-11. The location of the AE events with time evolution: the later occurrence of the near natural fracture event after the fracturing indicates the slippage of the natural fracture (Janis shale).

Post-test inspection of the sample shows that the induced fracture reached the top end of the sample and both sides of the upper piece while it did not reach the joint as shown in Figure 7-12. Some natural fractures are observed in the sample, but they were well-cemented and thus had less impact on the geometry of the induced fracture. The induced fracture is near vertical while its trajectory was influenced (turning) by the presence of the natural fracture (smooth saw-cut joint) as shown in right picture in Figure 7-12.

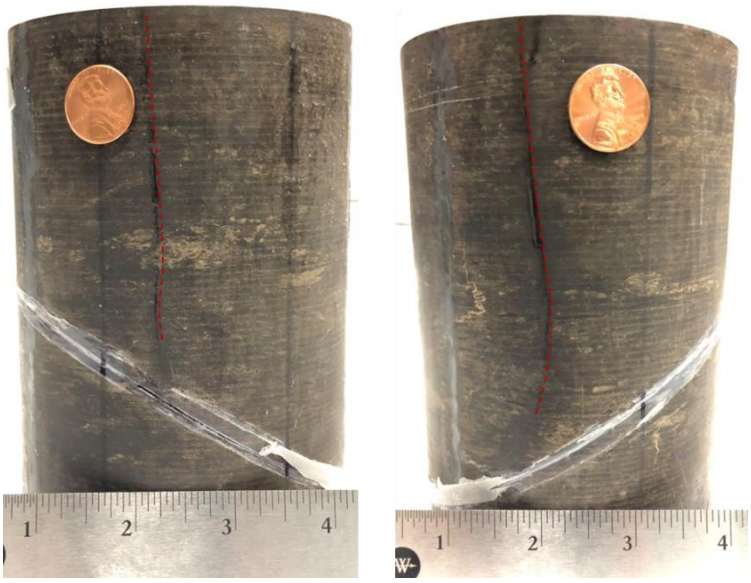


Figure 7-12. Observation of the fracture trace on the cylinder surface: the red dash line shows the hydraulic fracture trace; it turns as it approaches the natural fracture (Janis).

7.3.4 Test result with Sierra White granite

The Sierra White granite cylinder has a 45.4^{o} smooth saw-cut joint serving as a natural fracture. The confining pressure was 6.89 MPa (1000 psi) and the axis stress was 13.9 MPa (2017 psi, deviator stress, 7.01 MPa) at the start of injection. Same as previous tests, mineral oil was employed as fracturing fluid. In this case, the injection rate was 1.5 ml/min. A breakdown pressure of 18.0 MPa (2611 psi) was observed after 42.25 s of injection. Based on the record of the deviatoric stress, slippage on the joint and the injection condition, the whole test period can be divided into five phases as marked in Figure 7-13 and Figure 7-14. During Phase #1 (before fracturing), there was no apparent increase of the calculated displacements and so did the deviator stress. There were few AE activities recorded right before breakdown, which should be associated with the micro fracture creation. During Phase #2 (fracture initiation and propagation), the hydraulic fracture initiated and propagated

reaching the side surface and near the natural fracture. Displacements increased, with a larger value for the displacement across the joint (slippage). The stress drop is about 0.56 MPa with slippage on the natural fracture of 0.028 mm. The induced fracture was intersected the natural fracture at the end of Phase #2 while it did not reach the side surface yet. And it is likely that the induced fracture reached the side surface of the cylinder at early time during Phase #3 with the peak value of 0.0367 mm. During Phase #3, the injection pressure was dropping due to fluid flowing into the natural fracture and outside of the cylinder. In this time period, two large slippages on the natural fracture were observed with considerable decrease of deviator stress (2.53 MPa in total) and increase of displacement (0.089 mm in total) on the natural fracture. These two large slippages were due to the reduction of the effective normal stress resulting from increased pore pressure by the fluid flowing into the natural fracture. During Phase #4, continuous slippage was observed with continuous injection. After the ceasing of injection, the slippage continued for a very short time (1.5 second) and then stopped with the stress status reaching a stable condition. It is clear from the test result that the slippage of natural fracture could occur caused by an approaching hydraulic fracture. However, the magnitude of slippage resulting from the pore pressure increasing on the natural fracture is larger than that from the approaching hydraulic fracture.

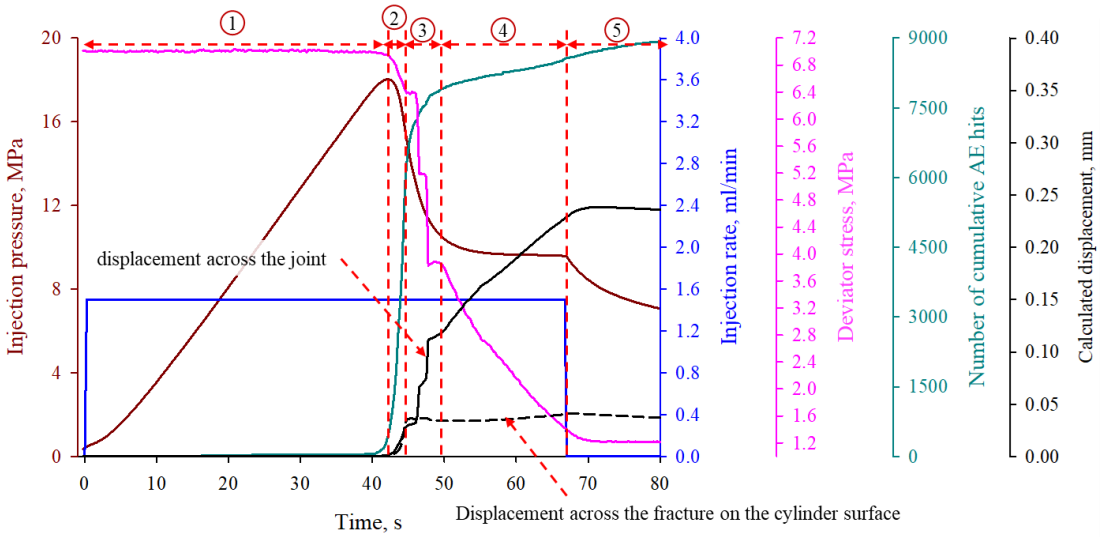


Figure 7-13. Recorded data during the test: AE activity jump and displacement jump was observed (Granite).

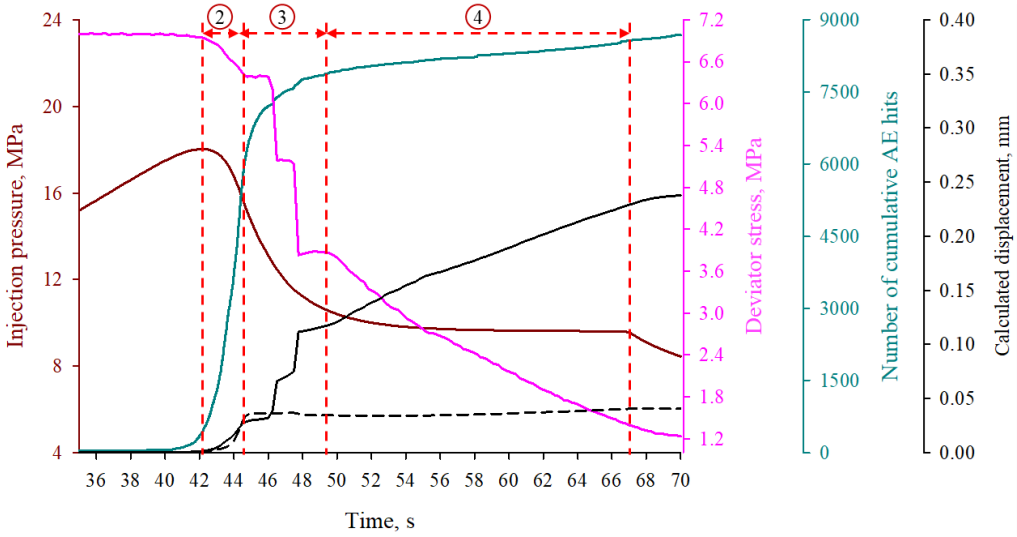


Figure 7-14. Recorded data near the pressure breakdown (Granite).

The located AE events was shown in Figure 7-15 with color indicating the event time and the red dash line indicating the natural fracture. It is clearly that there were some AE events

occurring on the natural fracture suggesting the sliding of the natural fracture. It is also observed that the slippage happened after the generation of the hydraulic fracture.

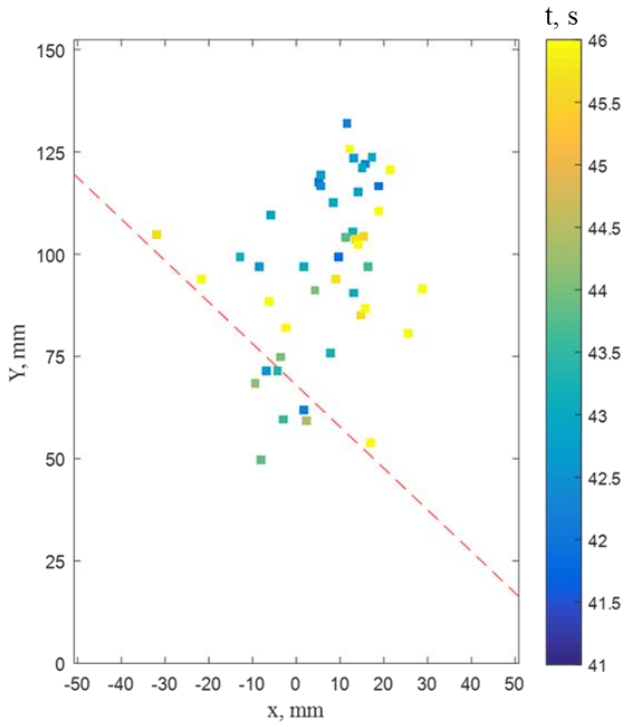


Figure 7-15. Recorded data near the pressure breakdown (Granite).

The post-test observation of the fracture geometry reveals that the induced hydraulic fracture reached one slide of the cylinder and also the natural fracture as shown in Figure 7-16. Due to the heterogeneousness of the notch and the impact of larger grain size compared with the shale samples, the geometry of the fracture was complicated and it only propagated mainly towards one side of the cylinder forming one wing fracture geometry.

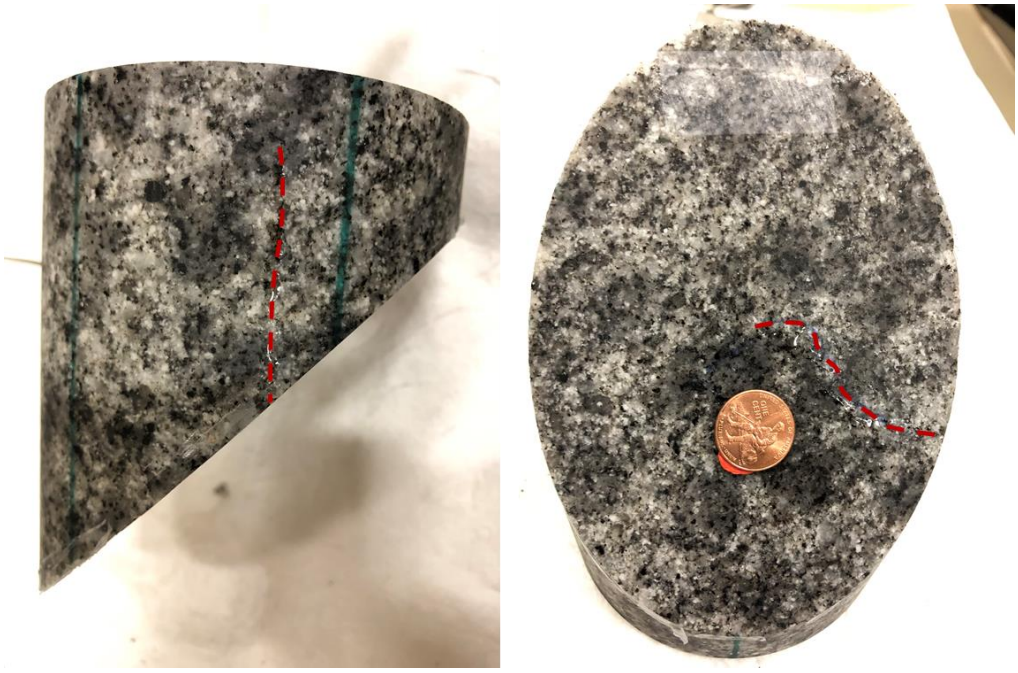


Figure 7-16. The fracture trace marked with red dash lines on the cylinder surface and natural fracture (Granite).

7.4 Summery and Conclusion

Analog experiments were conducted to investigate the interaction between a natural fracture and a hydraulic fracture with focus on slippage on a natural fracture or a bedding plane discontinuity due to an approaching hydraulic fracture. The tests were conducted on 101.6 mm diameter cylinder samples with a horizontal wellbore. The test materials included PMMA, shales, and Sierra White granite. Injection pressure, deviator stress, acoustic emission and the sample deformation are monitored during the test. In all the reported tests, the displacement calculated from the measured strain across the joint clearly shows a jump subsequent to pressure breakdown, and is accompanied by increased AE activity and decreased deviator stress. The displacement jump (slippage) across the joint with decreased deviatoric stress and AE activities on the joint show that the hydraulic fracture caused slip

of the saw-cut fractures even before reaching them. Analysis of the data clearly shows the occurrence of slippage on the joint in response to an approaching hydraulic fracture. The slippage due to the increased pore pressure on the natural fracture was also observed. Before the induced fracture reached the natural fracture, different degree of slippage (0.085mm ~ 0.11 mm) was obtained from these tests with various amount of deviator stress drop (0.14 MPa~ 0.6 MPa). Expectedly, the degree of shear slip varies with natural fracture dip, and friction angle and the differential stress. It is also observed that the pore pressure increase on the natural fracture by the encroaching hydraulic fracturing triggered larger slip on the natural fracture.

8. Summary and Conclusion

In this work, important issues in EGS development related to reservoir creation in different type of rocks and stress conditions, reservoir monitoring during reservoir creation and consequent production, fluid/heat flow in the induced fracture, and the interaction between the hydraulic fracture and natural fracture were investigated with lab-scale experiments. A novel lab-scale EGS test system was developed which allows the performance of EGS simulation experiments on rock blocks under high pore pressure/elevated temperature and representative in-situ stress regimes with simultaneously recording Acoustic Emission, self-potential, temperature/pressure and tracers. The concepts of reservoir stimulation by hydraulic fracturing, heating mining by cold water circulation, reservoir characterization by tracer injection were performed on the 330 mm × 330 mm ×330 mm cubic igneous blocks. Two kinds of igneous rocks with different textures were tested with one injection hole and four production/monitoring wells. Moreover, analog experiments were conducted to investigate the interaction between a natural fracture and an approaching hydraulic fracture with focus on slippage on a natural fracture or a bedding plane discontinuity due to the mechanical stress induced by the hydraulic fracture. The tests were conducted on 101.6 mm diameter cylinder samples with a horizontal wellbore. Different materials including PMMA, shales, and Sierra White granite were tested and similar phenomenon was observed.

The major finds from the experimental investigation of EGS simulation tests and the HF/NF interaction tests are:

1) The AE cloud and its evolution during reservoir creation correctly reflects the fracture propagation path as ascertained by wellbore pressure monitoring and post-

mortem observation. The hydraulically induced fracture propagates very fast due to the low viscosity fluid used (water) as the fracturing fluid. Failure mechanism analysis of the AE Events from the Sierra White granite test indicates that the percentage of compressional failure events was 10 percent more in the stepped constant flowrate (SCF) test than in the hydraulic fracturing test. Also, the percentage of tensile failure and shear failure decreases during the SCF test compared with the hydraulic fracturing phase due to the reopening of the fracture. The flow impedance of the intact block improved about 72 times after simulation. The tested blocks were cut into slabs and the fracture trace revealed on the cutting surface was used to reconstruct the geometry of the induced fracture in 3D. The reconstructed 3D fracture geometry shows a good agreement with the AE monitoring result, which proves the feasibility of MEQ (field scale of acoustic emission) application in EGS. Analysis of the fracture surface profile from laser scanning shows that the hydraulically induced fracture has a rough surface with a roughness coefficient (JRC) of 12.98 and tortuosity of 1.10, both of which are similar to fractures from the Brazilian test. The thin section and SEM observations show that the fracture follows the weak boundary between the quartz and albite grains.

2) SP monitoring during fracturing, circulation and tracer tests indicates that the SP response is mainly controlled by electrokinetic coupling, and the thermoelectric coupling has a negligible impact on the SP. This observation is in agreement with field records and numerical modeling by other investigators. The reason is the relatively small thermoelectric coupling coefficient under field salinity conditions. Unlike the temperature gradient, fluid concentration (salinity) has a great influence

on the SP response when the concentration contrast between the injection fluid and the pore fluid is large. However, the considerable impact of the liquid concentration difference is manifested by the reduction of the streaming potential coefficient in high solute concentration liquid. The experimental data also shows that the main direction of liquid flow could be identified using the SP response. With an SP array, the fluid flow in an EGS reservoir could be mapped during both the fracturing and production stages. However, the liquid saturation influences the recorded SP response so that rock at a lower saturation would yield a smaller apparent coupling coefficient as there is less movable fluid under pressure. Under the test conditions, the measured streaming potential coefficient is -130.5 mV/MPa for an intact Sierra White granite block saturated with 0.002 Mole/L NaCl. The obtained values in this research are similar to those reported by Moore (-200 mV/MPa) for the same rock using a 0.001 Mole/L NaCl solution in a smaller cylindrical sample. Due to its extremely low porosity, the amplitude of SP and the streaming potential coefficient are both much smaller, which suggest that sufficient liquid saturation and rock porosity are needed to obtain a strong signal.

3) Due to the heterogeneity of the rock and the initial notch used to lower the breakdown pressure, the induced hydraulic fracture in Sierra White granite (SWG) did not propagate uniformly in every direction. On the other hand, in the more homogeneous Raven Noir gabbro (RNG), the fracture extended more uniformly and all production wells were connected by the induced fracture during stimulation. Therefore, circulation tests with different number of the production wells connected were obtained in this project, providing us with the opportunity to investigate heat mining

under different scenarios. About 50W of power, which is high enough to light a home lamp, was produced in each circulation test from a fracture with 9 cm (3.5-inch) pathway in a 330.2 mm cubic rock block with temperature less than 80^{o}C, and thus it clearly demonstrates the great potential of energy supply of EGS. The percent heat extracted after injection of 2000 ml of water is about 6.24 %~ 7.85% of the heat stored in the heated rock blocks by fluid flowing through the fracture. It was found that heat extraction rate is a function of the effective heat exchange area (the actual flow path between the injection and production well) rather than the total fracture surface area. This suggests that the distance between injection/production wells or the location of the producer(s) and flow path tortuosity need be optimized to increase the effective heat exchange area in reservoir stimulation practice. The results of the circulation tests highlight the importance of reservoir creation and field management, i.e., controlling the injection and production rates to obtain a higher thermal production rate. The impact of fracture geometry/tortuosity on the preferential flow path development is evident in tests results. In the case where multiple wells were connected by the induced hydraulic fracture, the fluid tends to flow into the direction with less tortuosity and thus lower flow impedance. The test results indicate that rock texture impacts the fracture geometry and profile and thus influences the fluid flow/ heat transfer in the fracture. Excessive fracture propagation and high injection pressure was avoided during circulation tests by increasing the injection rate step by step.

The cooling effect of the rock matrix i.e., increased fracture conductivity and lowering of the injection pressure is clearly demonstrated in the circulation

experiments by the fact that lower injection pressure was obtained with high flow rate. The test result confirmed that the thermal, mechanical, and hydraulic effects must be considered when modeling the behavior of an EGS reservoir. The test results have provided insight for performing similar tests at larger scales e.g., in the COLLAB and FORGE projects.

4) As the first tracer test in lab-scale experimental EGS, the results are promising. The existence of two linear tracer tail observed in Sierra White granite test show a good correlation between hydraulic conductivity and the tracer concentration response. The flow geometry analysis using F-Φ curves from the tracer response shows that the fracture flow geometry to be relatively homogeneous in the measured directions. This can be attributed to the relatively simple fracture geometry with small tortuosity: a nearly horizontal fracture connecting the wells. However, the impact of fracture roughness on the fluid flow geometry still is evident. The fracture with a lower roughness experienced more homogeneous flow (lower Lorenz coefficient). However, the fracture aperture and fluid velocity calculated from tracer test results vary much with those estimated from cubic law. This highlights the difficulty of tracer test in lab-scale compared with the field scale applications. In the field, the fracture aperture, fracture volume, and the tracer travel time are much larger than their values in lab-scale tests. In addition, the flow rate in the lab-scale is much small than in the field, which introduces considerable difficulty in taking production samples. What's more, the test results provide some useful guide for future lab-scale tracer test deign. Low permeability rock is recommended for tracer tests to minimize leakage of the traced fluid into the rock matrix and also to improve the fluid recovery.

Low injection rate will increase the tracer time the in the fracture while a tracer candidate with low-concentration detectability is required.

5) The displacement calculated from the measured strain across the joint clearly shows a jump subsequent to breakdown, and is accompanied by increased AE activity and decreased deviator stress during the HF/NF interaction tests which clearly demonstrated that hydraulic fracture could cause the slip of the saw-cut fractures even before reaching them. The slippage due to the increased pore pressure on the natural fracture was also observed. Before the induced fracture reached the natural fracture, different levels of slippage (0.085mm ~ 0.11 mm) were obtained from these tests with various amount of deviator stress drop (0.14 MPa~ 0.6 MPa). Expectedly, the degree of shear slip varies with natural fracture dip, and friction angle and the differential stress. It is also observed that the pore pressure increase on the natural fracture by the encroaching hydraulic fracturing triggered larger slip on the natural fracture.

Biography

Adams, M.C., Beall, J.J., Enedy, S.L., Hirtz, P.N., Kilbourn, P., Koenig, B.A., Kunzman, R. and Smith, J.B (2001) Hydrofluorocarbons as geothermal vapor-phase tracers. Geothermics, 30(6), pp.747-775.

Ahmed AS, Revil A, Steck B, Vergniault C, Jardani A, Vinceslas G (2019) Self-potential signals associated with localized leaks in embankment dams and dikes. Eng Geol 253:229–239.

Alameda-Hernández, P., Jiménez-Perálvarez, J., Palenzuela, J.A., El Hamdouni, R., Irigaray, C., Cabrerizo, M.A. and Chacón, J (2014) Improvement of the JRC calculation using different parameters obtained through a new survey method applied to rock discontinuities. Rock mechanics and rock engineering, 47(6), pp.2047-2060.

Akaike, H (1974) A new look at the statistical model identification. IEEE transactions on automatic control 19(6): 716-723.

Akin, S. and A. Gulgor (2018) Comprehensive Tracer Testing in the Germencik Field. Proc., The 43rd Workshop on Geothermal Reservoir Engineering, Stanford University, Stanford, CA.

Anderson LA and Johnson GR (1976) Application of the self ‐ potential method to geothermal exploration in Long Valley, California. Journal of Geophysical Research, 81(8), pp.1527-1532.

Anderson, A. and Rezaie, B (2019) Geothermal technology: Trends and potential role in a sustainable future. Applied Energy, 248, pp.18-34.

Ames, MF (2016) Temperature-sensitive Tracers for Fractured Geothermal Reservoir Characterization. Proc., The 41st Workshop on Geothermal Reservoir Engineering, Stanford University, Stanford, CA, Stanford University.

Axelsson, G., Björnsson, G. and Montalvo, F (2005) Quantitative interpretation of tracer test data. In Proceedings world geothermal Congress (pp. 24-29).

Axelsson, G., Flovenz, O.G., Hauksdottir, S., Hjartarson, A. and Liu, J (2001) Analysis of tracer test data, and injection-induced cooling, in the Laugaland geothermal field, N-Iceland. Geothermics, 30(6), pp.697-725.

Axelsson, G., Björnsson, G. and Montalvo, F (2005) Quantitative interpretation of tracer test data. In Proceedings world geothermal Congress (pp. 24-29).

Aydin, H., Akin, S. and Salar, M (2018) Application of Fluorescent Micro Particles as Geothermal Tracers. Proc., The 43rd Workshop on Geothermal Reservoir Engineering, Stanford University, Stanford, CA.

Bai, B., He, Y., Li, X., Hu, S., Huang, X., Li, J. and Zhu, J., (2016). Local heat transfer characteristics of water flowing through a single fracture within a cylindrical granite specimen. Environmental Earth Sciences 75(22): 1460.

Bai, B., He, Y., Li, X., Li, J., Huang, X. and Zhu, J., (2017). Experimental and analytical study of the overall heat transfer coefficient of water flowing through a single fracture in a granite core. Applied Thermal Engineering 116: 79-90.

Bear, J (2013) Dynamics of fluids in porous media. Courier Corporation.

Becker, M.W., Remmen, K., Reimus, P.W. and Tsoflias, G.P (2013) Investigating well connectivity using ionic tracers. Thirty-Eighth Workshop on Geothermal Reservoir Engineering, Stanford, California.

Becker, M.W. and Shapiro, A.M (2003) Interpreting tracer breakthrough tailing from different forced ‐ gradient tracer experiment configurations in fractured bedrock. Water Resources Research, 39(1).

Blanton, T. L (1982) An experimental study of interaction between hydraulically induced and pre-existing fractures. SPE unconventional gas recovery symposium, Society of Petroleum Engineers.

Blanton TL (1986) Propagation of hydraulically and dynamically induced fractures in naturally fractured reservoirs. In: Society of petroleum engineers unconventional gas technology symposium, Louisville, May 18–21, SPE Paper 15261, p 15

Bunger, A.P., Kear, J., Jeffrey, R.G., Prioul, R. and Chuprakov, D (2015) Laboratory investigation of hydraulic fracture growth through weak discontinuities with active ultrasound monitoring. In 13th ISRM International Congress of Rock Mechanics. International Society for Rock Mechanics and Rock Engineering.

Butler DK, Llopis JL, Dobecki TL, Wilt MJ, Corwin RF and Olhoeft G (1990) Comprehensive geophysics investigation of an existing dam foundation: Engineering geophysics research and development, Part 2. The Leading Edge, 9(9), pp.44-53.

Cheng, A.H.-D., Ghassemi, A., and Detournay, E (2001) Integral Equation Solution of Heat Extraction from a Fracture in Hot Dry Rock. International Journal for Numerical and Analytical Methods in Geomechanics 25 (13): 1327–1338.

Cheng, Q., Wang, XN. and Ghassemi, A (2019) Numerical simulation of reservoir stimulation with reference to the Newberry EGS. Geothermics, 77, pp.327-343.

Christensen, J., Hawkins, A., Brown1c, S., Sonnenthal, E., Sturchio, N., and DePaolo, D (2018) The use of 222Rn to Constrain Fracture Characteristics: Experiments Conducted at the MesoScale Model Geothermal Reservoir Site at Altona, New York. Proc., The 43rd Workshop on Geothermal Reservoir Engineering, Stanford University, Stanford, CA.

Corwin, R.F. and Hoover, D.B (1979) The self-potential method in geothermal exploration. Geophysics, 44(2), pp.226-245.

Corwin RF, Morrison HF (1977) Self-potential variations preceding earthquakes in central California. Geophys Res Lett 4(4):171–174

Corwin RF, DeMoully GT, Harding R. and Morrison HF (1981) Interpretation of self‐potential survey results from the East Mesa Geothermal Field, California. Journal of Geophysical Research: Solid Earth, 86(B3), pp.1841-1848.

Craig, S.L., Udell, K.S., McLennan, J. and Moore, J (2014) An experimental study of thermal and hydraulic geothermal reservoir stimulation of brittle impermeable material. In Thirty-Ninth workshop on geothermal reservoir engineering, Stanford University, Stanford (pp. 50-55).

Danckwerts, P (1953) Continuous Flow Systems, Distribution of Residence Times. Chemical Engineering Science, Vol. 2, No. 1, pp. 1–18.

Darnet M, Maineult A and Marquis, G (2004) On the origins of self‐potential (SP) anomalies induced by water injections into geothermal reservoirs. Geophysical Research Letters, 31(19).

Deeds, N.E., Pope, GA. and McKinney, DC (1999) Vadose zone characterization at a contaminated field site using partitioning interwell tracer technology. Environ Sci Technol 33(16): 2745-2751.

Dean, C., Reimus, P., Oates, J., Rose, P., Newell, D. and Petty, S., 2015. Laboratory experiments to characterize cation-exchanging tracer behavior for fracture surface area estimation at Newberry Crater, OR. Geothermics, 53, pp.213-224.

Dehghan, A.N., Goshtasbi, K., Ahangari, K. and Jin, Y (2015) Experimental investigation of hydraulic fracture propagation in fractured blocks. Bulletin of Engineering Geology and the Environment, 74(3), pp.887-895.

De Pater, C.J. and Beugelsdijk, L.J.L (2005) Experiments and numerical simulation of hydraulic fracturing in naturally fractured rock. In Alaska Rocks 2005, The 40th US Symposium on Rock Mechanics (USRMS). American Rock Mechanics Association.

Dobroskok, A. and Ghassemi, A (2004) Crack propagation, coalescence and re-initiation in naturally fractured rocks. GRC Trans, 28, pp.285-288.

Dukhin SS and Deriaguine BV (1974) Surface and Colloid Science: Electrokinetic Phenomena: Translated from the Russian by A. Mistetsky and M. Zimmerman. Plenum Press.

Eccles D, Sammonds PR and Clint OC (2005) Laboratory studies of electrical potential during rock failure. International Journal of Rock Mechanics and Mining Sciences, 42(7-8), pp.933-949.

Fagerlund F and Heinson G (2003) Detecting subsurface groundwater flow in fractured rock using self-potential (SP) methods. Environmental Geology, 43(7), pp.782-794.

Fenoglio MA, Johnston MJ and Byerlee JD (1995) Magnetic and electric fields associated with changes in high pore pressure in fault zones: Application to the Loma Prieta ULF emissions. Journal of Geophysical Research: Solid Earth, 100(B7), pp.12951-12958.

Finizola A, Sortino F, Lénat JF and Valenza M (2002) Fluid circulation at Stromboli volcano (Aeolian Islands, Italy) from self-potential and CO2 surveys. Journal of Volcanology and Geothermal Research, 116(1-2), pp.1-18.

Fitterman DV (1978) Electrokinetic and magnetic anomalies associated with dilatant regions in a layered earth. Journal of Geophysical Research: Solid Earth, 83(B12), pp.5923-5928.

Fitterman DV and Corwin RF (1982) Inversion of self-potential data from the Cerro Prieto geothermal field, Mexico. Geophysics, 47(6), pp.938-945.

Foulger, G.R., Julian, B.R., Hill, D.P., Pitt, A.M., Malin, P.E. and Shalev, E (2004) Non-double-couple microearthquakes at Long Valley caldera, California, provide evidence for hydraulic fracturing. Journal of Volcanology and Geothermal Research, 132(1), pp.45-71.

Foxboro, C (1999) Conductivity ordering guide. Oct, 3, p.2.

Frash, L.P., Gutierrez, M., Hampton, J. and Hood, J (2015) Laboratory simulation of binary and triple well EGS in large granite blocks using AE events for drilling guidance. Geothermics 55: 1-15.

Frash, L.P., Arora, K., Gan, Y., Lu, M., Gutierrez, M., Fu, P., Morris, J. and Hampton, J., (2018). Laboratory validation of fracture caging for hydraulic fracture control. In 52nd US Rock Mechanics/Geomechanics Symposium. American Rock Mechanics Association.

Gao, Q. and Ghassemi, A (2016) 3D Thermo-poromechanical analysis of reservoir stimulation using damage mechanics with application to the Fenton Hill HDR Experiment. In 50th US Rock Mechanics/Geomechanics Symposium, American Rock Mechanics Association.

Gao, Q. and Ghassemi, A (2019) Height Growth in Layered Unconventional Reservoirs: The Impact of Formation Moduli, Interfaces and In-situ Stress. Paper presented at the Unconventional Resources Technology Conference, Denver, CO, USA, 22-24 July.

Garg SK, Pritchett J, Wannamaker PE and Combs J (2007) Characterization of geothermal reservoirs with electrical surveys: Beowawe geothermal field. Geothermics, 36(6), pp.487-517.

Ghassemi, A (2012) A review of some rock mechanics issues in geothermal reservoir development. Geotechnical and Geological Engineering 30(3): 647-664.

Ghassemi, A., Nygren, A., and Cheng, A (2008) Effects of Heat Extraction on Fracture Aperture: A Poro–Thermoelastic Analysis. Geothermics 37 (5): 525–539.

Ghassemi, A. and Suarez-Rivera, R (2012) Sustaining fracture area and conductivity of gas shale reservoirs for enhancing long-term production and recovery. RPESEA Report 08112-08148. Final.

Ghassemi, A., and Tao, Q (2016) Thermo-poroelastic effects on reservoir seismicity and permeability change. Geothermics Special Issue on EGS.

Ghassemi, A., Tarasovs, S., and Cheng, A.H.-D (2007) A 3-D Study of the Effects of Thermomechanical Loads on Fracture Slip in Enhanced Geothermal Reservoirs. International Journal of Rock Mechanics and Mining Sciences 44 (8): 1132–1148.

Ghassemi, A., Zhang, Q (2006) Poro-thermoelastic response of a stationary crack using the displacement discontinuity method. ASCE J. Engineering Mechanics, 132(1), 26-33.

Ghassemi, A., and Zhou, X (2011) A three-dimensional thermo-poroelastic model for fracture response to injection/extraction in enhanced geothermal systems. Geothermics,40 (1), 39-49.

Giulia Di Giuseppe M, Troiano A, Somma R, Carlino S, Troise C and De Natale G (2016) A Self Potential study of the summit geothermal system of the Krafla volcano (Iceland). In EGU General Assembly Conference Abstracts, Vol 18.

Gokhberg MB, Morgounov VA, Yoshino T, Tomizawa I (1982) Experimental measurement of electromagnetic emissions possibly related to earthquakes in Japan. J Geophys Res Solid Earth 87(B9):7824–7828.

Gonzalez, F (1994) Study of fracturing process in reservoir rocks. Master thesis, The University of Oklahoma.

Goodman, R.E (1976) Methods of Geological Engineering in Discontinuous Rocks. West Publishing Company.

Graham MT, MacAllister DJ, Vinogradov J, Jackson MD, Butler AP (2018) Self-Potential as a Predictor of Seawater Intrusion in Coastal Groundwater Boreholes. Water Resources Research 54(9):6055–6071

Grosse, C. U., and Ohtsu, M (2008) Acoustic Emission Testing. Basic for Research—Applications in Civil Engineering. Leipzig, Germany, Springer.

Gu, H. and Weng, X (2010). Criterion for fractures crossing frictional interfaces at non-orthogonal angles. In 44th US rock mechanics symposium and 5th US-Canada rock mechanics symposium. American Rock Mechanics Association.

Guo, B., Fu, P., Hao, Y. and Carrigan, C.R (2016) Investigating the possibility of using tracer tests for early identification of EGS reservoirs prone to flow channeling (No. LLNL-CONF-682357). Lawrence Livermore National Lab.(LLNL), Livermore, CA (United States).

Guglielmi, Y., Cappa, F., Avouac, J.P., Henry, P. and Elsworth, D (2015) Seismicity triggered by fluid injection–induced aseismic slip. Science, 348(6240), pp.1224-1226.

Gunter, G.W., Finneran, J.M., Hartmann, D.J. and Miller, J.D (1997) Early determination of reservoir flow units using an integrated petrophysical method. In SPE Annual Technical Conference and Exhibition. Society of Petroleum Engineers.

Haimson, B.C. and Zhao, Z (1991) January. Effect of borehole size and pressurization rate on hydraulic fracturing breakdown pressure. In 32nd US Symposium on Rock Mechanics (USRMS). American Rock Mechanics Association.

Hampton, J., Frash, L., Matzar, L. and Gutierrez, M (2018). Extended-Term Monitoring of Acoustic Emissions Post-Laboratory Hydraulic Fracturing. In 52nd US Rock Mechanics/Geomechanics Symposium. American Rock Mechanics Association.

Hawkins, A. J (2017) Reactive tracers for characterizing fractured geothermal reservoirs, Cornell University. Ph.D.

Hawkins, A.J., Fox, D.B., Becker, M.W. and Tester, J.W (2017) Measurement and simulation of heat exchange in fractured bedrock using inert and thermally degrading tracers. Water Resources Research 53(2): 1210-1230.

Hawkins, A., Fox, D., Zhao, R., Tester, J., Cathles, L., Koch, D. and Becker, M (2015) Predicting thermal breakthrough from tracer tests: Simulations and observations in a low temperature field laboratory. Proceedings of the Fortieth Workshop on Geothermal Reservoir Engineering, Stanford University.

Himmelblau, D.M. and K.B. Bischoff (1968) Process Analysis and Simulation: Deterministic Systems, John Wiley & Sons, Inc. New York

Hoversten GM and Gasperikova E (2004) Non-seismic geophysical approaches to monitoring (No. LBNL-58326). Lawrence Berkeley National Lab.(LBNL), Berkeley, CA (United States).

Hu, LB, Ghassemi, A., Pritchett, J. and Garg, S., (2016). Laboratory Scale Investigation of Enhanced Geothermal Reservoir Stimulation. In 50th US Rock Mechanics/Geomechanics Symposium. American Rock Mechanics Association.

Hu LB, Ghassemi A, Pritchett J and Garg SK (2017a) Experimental Investigation of Hydraulically Induced Fracture Properties in Enhanced Geothermal Reservoir Stimulation. In Proceeding of 42nd Stanford Geothermal Workshop held in Stanford University, Stanford, California, USA.

Hu, LB, Ghassemi, A., Pritchett, J. and Garg, S., (2017b). Characterization of Hydraulically Induced Fracture in Labscale Enhanced Geothermal Reservoir. In Proceedings, 41st GRC Annual Meeting held in Salt Lake City, Utah, USA.

Hu, LB, Ghassemi A (2018a) Lab-scale investigation of a multi well enhanced geothermal reservoir. In Proceeding 43rd Stanford Geothermal Workshop held in Stanford University, Stanford, California, USA

Hu, LB and Ghassemi, A., (2018b). Heat and Fluid Flow Characterization of Hydraulically Induced Fracture in Lab-Scale. In 52nd US Rock Mechanics/Geomechanics Symposium. American Rock Mechanics Association.

Hu, LB, Ghassemi, A., Pritchett, J. and Garg, S., (2019a). Characterization of laboratory-scale hydraulic fracturing for EGS. Geothermics.

Hu, LB, Ghassemi, A., Pritchett, J., Garg, S. and Ishido, T., (2019b). Self-Potential Response in Laboratory Scale EGS Stimulation. Rock Mechanics and Rock Engineering, pp.1-13.

Hu, LB and Ghassemi, A., 2019c. Heat Production from Lab-scale Enhanced Geothermal Systems in Granite and Gabbro. International Journal of Rock Mechanics and Mining Sciences. (under review)

Ishida, T., Chen, Q., Mizuta, Y. and Roegiers, J.C (2004) Influence of fluid viscosity on the hydraulic fracturing mechanism. Journal of energy resources technology, 126(3), pp.190-200.

Ishida, T., Aoyagi, K., Niwa, T., Chen, Y., Murata, S., Chen, Q. and Nakayama, Y (2012) Acoustic emission monitoring of hydraulic fracturing laboratory experiment with supercritical and liquid CO2. Geophysical Research Letters, 39(16). doi:10.1029/2012GL052788

Ishido T and Mizutani H (1981) Experimental and theoretical basis of electrokinetic phenomena in rock‐water systems and its applications to geophysics. Journal of Geophysical Research: Solid Earth, 86(B3), pp.1763-1775.

Ishido, T. and Pritchett, J., (1999) Numerical simulation of electrokinetic potentials associated with subsurface fluid flow. Journal of Geophysical Research: Solid Earth, 104(B7), pp.15247-15259.

Ishido T and Pritchett J (2011) Effects of diffusion potential on self-potential distribution in geothermal areas, Geothermal Resources Council Transactions, 35, 1687-1691.

Ishido T, Tosha T, Akasaka C, Nishi Y, Sugihara M, Kano Y and Nakanishi S (2011) Changes in geophysical observables caused by CO2 injection into saline aquifers. Energy Procedia, 4, pp.3276-3283.

Ishido T, Pritchett J, Nishi Y, Sugihara M, Kano Y, Matsushima N, Kikuchi T, Tosha T and Ariki K (2018) Self-Potential Monitoring at the Sumikawa Geothermal Field, Akita, Japan, In Proceeding of 43rd Stanford Geothermal Workshop held in Stanford University, Stanford, California, USA.

Jardani A, Revil A, Bolève A. and Dupont JP (2008) Three‐dimensional inversion of self‐potential data used to constrain the pattern of groundwater flow in geothermal fields. Journal of Geophysical Research: Solid Earth, 113(B9).

Jin, M., Delshad, M., Dwarakanath, V., McKinney, D.C., Pope, G.A., Sepehrnoori, K., Tilburg, C.E. and Jackson, R.E (1995) Partitioning tracer test for detection, estimation, and remediation performance assessment of subsurface nonaqueous phase liquids. Water Resources Research, 31(5), pp.1201-1211.

Jouniaux L and Ishido T (2012) Electrokinetics in earth sciences: a tutorial. International Journal of Geophysics.

Jouniaux L and Pozzi JP (1995) Streaming potential and permeability of saturated sandstones under triaxial stress: Consequences for electrotelluric anomalies prior to earthquakes. Journal of Geophysical Research: Solid Earth, 100(B6), pp.10197-10209.

Jung, R (2013) EGS—Goodbye or Back to the Future. ISRM International Conference for Effective and Sustainable Hydraulic Fracturing, International Society for Rock Mechanics.

Kahn, D., Roberts, J. and Rich, J (2017) Integrating Microseismic and Geomechanics to Interpret Hydraulic Fracture Growth. In Unconventional Resources Technology Conference, Austin, Texas, 24-26 July 2017 (pp. 3282-3288). Society of Exploration Geophysicists, American Association of Petroleum Geologists, Society of Petroleum Engineers.

Kamali, A. and Ghassemi, A (2017) Reservoir Stimulation in Naturally Fractured Poroelastic Rocks. In proceeeding of 51st US Rock Mechanics / Geomechanics Symposium, San Francisco, California, USA.

Keranen, K.M., Weingarten, M., Abers, G.A., Bekins, B.A. and Ge, S (2014) Sharp increase in central Oklahoma seismicity since 2008 induced by massive wastewater injection. Science, 345(6195), pp.448-451.

Kim, K., Rutqvist, J., Nakagawa, S. and Birkholzer, J (2017) TOUGH–RBSN simulator for hydraulic fracture propagation within fractured media: Model validations against laboratory experiments. Computers & Geosciences, 108, pp.72-85.

Kohl, T., Evans, K.F., Hopkirk, R.J., and Rybach, L (1995a) Coupled Hydraulic, Thermal and Mechanical Considerations for the Simulation of Hot Dry Rock Reservoirs. Geothermics, 24 (3): 345–359.

Kohl T., Evans, K.F., Hopkirk, R.J., Jung, R., Rybach, L (1995b) Modelling of turbulent flow transients within Hot Dry Rock fracture systems: Preliminary Results. Proc. World Geothermal Congress, Florence, Italy, pp. 2597-2600.

Kong, X.Z., Deuber, C.A., Kittilä, A., Somogyvári, M., Mikutis, G., Bayer, P., Stark, W.J. and Saar, M.O (2018) Tomographic reservoir imaging with DNA-labeled silica nanotracers: The first field validation. Environmental science & technology, 52(23), pp.13681-13689.

Koshelev, V. and Ghassemi, A (2003a) Numerical modeling of stress distribution and crack trajectory near a fault or a natural fracture. Soil-Rock America Symp., Boston, MA

Koshelev, V. and Ghassemi, A (2003b) Hydraulic fracture propagation near a natural discontinuity. Proceeding of the 28th Workshop on Geothermal Reservoir Engineering Stanford University, Stanford, CA.

Kristjánsson, B.R., Axelsson, G., Gunnarsson, G., Gunnarsson, I. and Óskarsson, F (2016) Comprehensive tracer testing in the Hellisheidi Geothermal Field in SW-Iceland. Proceedings, 41st Workshop on Geothermal Reservoir Engineering.

Kuo, C., Song, S., Rose, P. and Liu, C (2018) Reactive tracer experiments in a low temperature geothermal field, Yilan, Taiwan. Geothermics 74: 298-304.

Kumar, D. and Ghassemi, A (2015) 3D simulation of mixed-mode poroelastic fracture propagation for reservoir stimulation. In 39th GRC Annual Meeting, Reno, Nevada (pp. 1-11).

Lake, L.W (1989) Enhanced Oil Recovery. Prentice Hall

Lamont, N. and Jessen, F.W (1963) The effects of existing fractures in rocks on the extension of hydraulic fractures. Journal of Petroleum Technology, 15(02), pp.203-209.

Leinov, E., Vinogradov, J. and Jackson, M.D (2010) Salinity dependence of the thermoelectric coupling coefficient in brine-saturated sandstones Geophysical Research Letters, 37(23).

Leong, Y., de Iongh, J.E., Bähring, S., Tuxen, A.K. and Nielsen, T.B (2015) Estimation of fracture volume between well pairs using deuterium tracer. SPE Annual Technical Conference and Exhibition, Society of Petroleum Engineers.

Levenspiel, O (1972) Chemical Reaction Engineering, 2nd edition, New York: John Wiley and Sons, Chapter 9.

Li, N., Zhang, S., Zou, Y., Ma, X., Wu, S, Zhang, YN (2018) Experimental analysis of hydraulic fracture growth and acoustic emission response in a layered formation. Rock Mechanics and Rock Engineering 51(4):1047–1062

Li, YW (2017) New and Improved Techniques for Characterizing Brittle Rock Response. The University of Oklahoma. Ph.D dissertation.

Lockner DA, Johnston MJS and Byerlee JD (1983) A mechanism to explain the generation of earthquake lights. Nature, 302(5903), p.28.

Lorne B, Perrier F and Avouac JP (1999) Streaming potential measurements: 1. Properties of the electrical double layer from crushed rock samples. Journal of Geophysical Research: Solid Earth, 104(B8), pp.17857-17877.

Maineult, A., Darnet, M. and Marquis, G., (2006a). Correction to "On the origins of self‐potential (SP) anomalies induced by water injections into geothermal reservoirs". Geophysical Research Letters, 33(20).

Maineult A, Bernabé Y, Ackerer P (2006b) Detection of advected,reacting redox fronts from self-potential measurements. J Contam Hydrol 86(1–2):32–52.

Maloszewski, P. and A. Zuber (1993) Tracer experiments in fractured rocks: matrix diffusion and the validity of models. Water Resources Research 29(8): 2723-2735.

Marine, IW (1967) The use of a tracer test to verify an estimate of the groundwater velocity in fractured crystalline rock at the Savannah River plant near Aiken, South Carolina. Isotope Techniques in the Hydrologic Cycle 11: 171-179.

Marquis, G., Darnet, M., Sailhac, P., Singh, A.K. and Gérard, A., (2002). Surface electric variations induced by deep hydraulic stimulation: An example from the Soultz HDR site. Geophysical Research Letters, 29(14), pp.7-1.

Mattson, E.D., Zhang, Y., Hawkins, A., Johnson, T., Ajo-Franklin, J., Neupane, G.H. and Plummer, M.A (2019) Preliminary Collab Fracture Characterization Results from Flow and Tracer Testing Efforts (No. INL/CON-18-51813-Rev000). Idaho National Lab.(INL), Idaho Falls, ID (United States).

Minsley BJ, Sogade J, Morgan FD (2007) Three-dimensional source inversion of self-potential data. J Geophys Res Solid Earth.

Mitchell JK (1976) Fundamentals of Soil Behavior. John Wiley and Sons, New York

Miyakoshi JI (1986) Anomalous time variation of the self-potential in the fractured zone of an active fault preceding the earthquake occurrence. Journal of geomagnetism and geoelectricity, 38(10), pp.1015-1030.

Mizutani H, Ishido T, Yokokura T and Ohnishi S (1976) Electrokinetic phenomena associated with earthquakes. Geophysical Research Letters, 3(7), pp.365-368.

Moore, J.R (2007a) Application of the self -potential method in hydrogeology, University of California, Berkeley. Ph.D.

Moore, J.R. and Glaser, SD (2005) Self-Potential Observations During Hydraulic Fracturing in the Laboratory. In Alaska Rocks 2005, The 40th US Symposium on Rock Mechanics (USRMS). American Rock Mechanics Association.

Moore, J.R. and Glaser, SD (2006) The Self-potential Response during Hydraulic Fracturing of Sierra Granite, In proceeding of the Thirty-First Workshop on Geothermal Reservoir Engineering Stanford University, Stanford, California.

Moore, J.R. and Glaser, SD (2007b) Self-potential observations during hydraulic fracturing, Journal of Geophysical Research: Solid Earth, 112(B2.

Moore JR, Glaser SD, Morrison HF and Hoversten GM (2004) The streaming potential of liquid carbon dioxide in Berea sandstone. Geophysical research letters, 31(17).

Morgan FD, Williams ER and Madden TR (1989) Streaming potential properties of westerly granite with applications. Journal of Geophysical Research: Solid Earth, 94(B9), pp.12449-12461. doi:10.1029/JB094iB09p12449

Naudet V, Revil A (2005) A sandbox experiment to investigate bacteria-mediated redox processes on self-potential signals. Geophys Res Lett.

Naudet V, Revil A, Rizzo E, Bottero JY, Bégassat P (2004) Groundwater redox conditions and conductivity in a contaminant plume from geoelectrical investigations. Hydrol Earth Syst Sci 8:8–22.

Nelson, E.J., Chipperfield, S.T., Hillis, R.R., Gilbert, J. and McGowen, J (2007) Using geological information to optimize fracture stimulation practices in the Cooper Basin, Australia. Petroleum Geoscience, 13(1), pp.3-16.

Ng, K.W., Poudel, R., Kyle, W., Tan, G. and Podgorney, R (2017) A Laboratory Experimental Study of Enhanced Geothermal Systems. In 51st US Rock Mechanics/Geomechanics Symposium. American Rock Mechanics Association.

Niibori, Y., Ogura, H. and Chida, T (1995) Identification of geothermal reservoir structure analyzing tracer responses using the Two-Fractured-Layer model. Geothermics 24(1): 49-60.

Nottebohm, M., Licha, T., Ghergut, I., Nödler, K. and Sauter, M (2010) Development of thermosensitive tracers for push-pull experiments in geothermal reservoir characterization. Proceedings of the World Geothermal Congress, Bali, Indonesia.

Nottebohm, M., Licha, T. and Sauter, M (2012) Tracer design for tracking thermal fronts in geothermal reservoirs. Geothermics 43: 37-44.

Nyquist JE and Corry CE (2002) Self-potential: The ugly duckling of environmental geophysics. The Leading Edge, 21(5), pp.446-451.

Olson, J.E., Bahorich, B. and Holder, J (2012) Examining hydraulic fracture: natural fracture interaction in hydrostone block experiments. In SPE hydraulic fracturing technology conference. Society of Petroleum Engineers.

Ong, S. H (1994) Borehole stability. Ph.D. dissertation, The University of Oklahoma.

Onsager L (1931) Reciprocal relations in irreversible processes I&II, Phys. Rev. 37, 405; 38, 2265.

Pine, R.J. and Batchelor, A.S (1984) Downward migration of shearing in jointed rock during hydraulic injections. In International Journal of Rock Mechanics and Mining Sciences & Geomechanics Abstracts (Vol. 21, No. 5, pp. 249-263). Pergamon.

Pritchett J and Ishido T (2005) Hydrofracture characterization using downhole electrical monitoring. In Proceedings of World Geothermal Congress, Turkey.

Pruess, K (2002) Numerical simulation ofmultiphase tracer transport in fractured geothermal reservoirs. Geothermics 31(4): 475-499.

Rawal, A., and Ghassemi, A (2014) A Reactive poro-thermoealstic analysis of cold water injection in enhanced geothermal reservoir. Geothermics, 50, 10-23.

Reimus, P.W., Caporuscio, F.A., Marina, O.C. and Janney, D (2018) Field Demonstration of the Combined Use of Thermally-Degrading and Cation-Exchanging Tracers to Predict Thermal Drawdown in a Geothermal Reservoir, Los Alamos National Lab.(LANL), Los Alamos, NM (United States).

Renshaw CE, Pollard DD (1995) An experimentally verified criterion for propagation across unbounded frictional interfaces in brittle, linear elastic materials. Int J Rock Mech Min Sci Geomech 32:237–249

Revil A, Cary L, Fan Q, Finizola A and Trolard F (2005) Self‐potential signals associated with preferential ground water flow pathways in a buried pale‐channel. Geophysical Research Letters, 32(7).

Revil A, Mao D, Haas AK, Karaoulis M and Frash L (2015) Passive electrical monitoring and localization of fluid leakages from wells. Journal of Hydrology, 521, pp.286-301.

Reimus, P.W., Caporuscio, F.A., Marina, O.C. and Janney, D (2018) Field Demonstration of the Combined Use of Thermally-Degrading and Cation-Exchanging Tracers to Predict Thermal Drawdown in a Geothermal Reservoir, Los Alamos National Lab.(LANL), Los Alamos, NM (United States).

Robinson, B. A., and Tester, J. W (1984) Dispersed Fluid Flow in Fractured Reservoirs: An Analysis of Tracer-Determined Residence Time Distributions. Journal of Geophysical Research, Vol. 89, No. B12, pp. 10374–10384.

Rose, P.E., Benoit, W.R. and Kilbourn, P.M (2001) The application of the polyaromatic sulfonates as tracers in geothermal reservoirs. Geothermics 30(6): 617-640.

Rutqvist, J. and Stephansson, O (2003) The role of hydromechanical coupling in fractured rock engineering. Hydrogeology Journal, 11(1), pp.7-40.

Rutqvist, J., Wu, Y.S., Tsang, C.F. and Bodvarsson, G (2002) A modeling approach for analysis of coupled multiphase fluid flow, heat transfer, and deformation in fractured porous rock. International Journal of Rock Mechanics and Mining Sciences, 39(4), pp.429-442.

Safari, R., Ghassemi, A (2015) Three-dimensional thermo-poroelastic analysis of fracture network deformation and induced micro-seismicity in enhanced geothermal systems. Geothermics, 58, 1-14.

Sanjuan, B., Pinault, J.L., Rose, P., Gérard, A., Brach, M., Braibant, G., Crouzet, C., Foucher, J.C., Gautier, A. and Touzelet, S (2006) Tracer testing of the geothermal heat exchanger at Soultz-sous-Forêts (France) between 2000 and 2005. Geothermics 35(5-6): 622-653.

Sarmadivaleh M, Rasouli V (2013) Modified Renshaw and Pollard criteria for a non-orthogonal cohesive natural interface intersected by an induced fracture. Rock Mech Rock Eng 47(6):2107–2115.

Sesetty, V. and Ghassemi, A (2012) Simulation of hydraulic fractures and their interactions with natural fractures. In 46th US Rock Mechanics/Geomechanics Symposium. American Rock Mechanics Association.

Schaffer, M., Idzik, K.R., Wilke, M. and Licha, T (2016) Amides as thermo-sensitive tracers for investigating the thermal state of geothermal reservoirs. Geothermics 64: 180-186.

Schmalz, J.P. and Rahme, H.D (1950) The variation of waterflood performance with variation in permeability profile. Prod. Monthly, 15(9), pp.9-12.

Schön, J.H., (2015). Physical properties of rocks: Fundamentals and principles of petrophysics (Vol. 65), Elsevier.

Serres-Piole, C., Preud'Homme, H., Moradi-Tehrani, N., Allanic, C., Jullia, H. and Lobinski, R (2012) Water tracers in oilfield applications: guidelines. Journal of Petroleum Science and Engineering 98: 22-39.

Shapiro, S. A., Rothert, E., Rath, V., and Rindschwentner, J (2002) Characterization of fluid transport properties of reservoirs using induced microseismicity, Geophysics, 67, 212–220.

Sheffer MR and Oldenburg DW (2007) Three-dimensional modelling of streaming potential. Geophysical Journal International, 169(3), pp.839-848.

Shook, GM (2001) Predicting thermal breakthrough in heterogeneous media from tracer tests. Geothermics 30(6): 573-589.

Shook, GM (2003). A simple, fast method of estimating fractured reservoir geometry from tracer tests. Geothermal Resources Council Transactions, 27, pp.407-411.

Shook, GM and Forsmann, J.H (2005) Tracer interpretation using temporal moments on a spreadsheet (No. INL/EXT-05-00400). Idaho National Laboratory (INL).

Shook, GM and Mitchell, K.M (2009). A robust measure of heterogeneity for ranking earth models: The F PHI curve and dynamic Lorenz coefficient. In SPE annual technical conference and exhibition. Society of Petroleum Engineers.

Shook, GM and Suzuki, A., (2017). Use of tracers and temperature to estimate fracture surface area for EGS reservoirs. Geothermics, 67, pp.40-47.

Sill WR (1983) Self-potential modeling from primary flows, Geophysics, 48(1), pp.76-86.

Solberg, P., Lockner, D. and Byerlee, J.D (1980) Hydraulic fracturing in granite under geothermal conditions. In International Journal of Rock Mechanics and Mining Sciences & Geomechanics Abstracts (Vol. 17, No. 1, pp. 25-33). Pergamon.

Stiles, W.E (1949) Use of permeability distribution in waterflood calculations. J. Petrol. Technol. 1.01, 9–13.

Stoeckhert, F., Molenda, M., Brenne, S. and Alber, M., (2015). Fracture propagation in sandstone and slate–Laboratory experiments, acoustic emissions and fracture mechanics. Journal of Rock Mechanics and Geotechnical Engineering, 7(3), pp.237-249.

Stoeckhert, F., Molenda, M., Brenne, S. and Alber, M (2015) Fracture propagation in sandstone and slate–Laboratory experiments, acoustic emissions and fracture mechanics. Journal of Rock Mechanics and Geotechnical Engineering, 7(3), pp.237-249.

Suzuki, A., Cui, J., Zhang, Y., Li, K. and Horne, R.N (2018) Nano-/Microparticle Tracers for Evaluating Structures in Fractured Porous Media. In Proceedings of the 43rd Workshop on Geothermal Reservoir Engineering, Stanford University, Stanford, California

Tarasovs, S. and Ghassemi, A (2014) Self-similarity and scaling of thermal shock fractures. Physical Review E 90 (1), 012403-1-6.

Tester, J.W., Potter, R.M. and Bivins, RL (1982) Interwell tracer analyses of a hydraulically fractured granitic geothermal reservoir. Society of Petroleum Engineers Journal 22(04): 537-554.

Tester, J.W., Anderson, B.J., Batchelor, A.S., Blackwell, D.D., DiPippo, R., Drake, E.M., Garnish, J., Livesay, B., Moore, M.C., Nichols, K. and Petty, S (2006) The future of geothermal energy. Impact of Enhanced Geothermal Systems (EGS) on the United States in the 21st Century, Massachusetts Institute of Technology, Cambridge, MA, 372.

Tian, W., Wu, X., Shen, T. and Kalra, S. (2016). Estimation of hydraulic fracture volume utilizing partitioning chemical tracer in shale gas formation. Journal of Natural Gas Science and Engineering 33: 1069-1077.

Triantis D, Stavrakas I, Kyriazopoulos A, Hloupis G and Agioutantis Z (2012) Pressure stimulated electrical emissions from cement mortar used as failure predictors. International Journal of Fracture, 175(1), pp.53-61.

Trique M, Perrier F, Froidefond T, Avouac JP and Hautot S (2002) Fluid flow near reservoir lakes inferred from the spatial and temporal analysis of the electric potential. Journal of Geophysical Research: Solid Earth, 107(B10), pp.EPM-5.

Tse, R. and Cruden, D.M (1979) Estimating joint roughness coefficients. International journal of rock mechanics and mining sciences & geomechanics abstracts, vol. 16, no. 5, pp. 303-307. Pergamon.

Varotsos P, Sarlis N, Eftaxias K, Lazaridou M, Bogris N, Makris J, Abdulla A and Kapiris P (1999) Prediction of the 6.6 Grevena-Kozani earthquake of May 13, 1995. Physics and Chemistry of the Earth, Part A: Solid Earth and Geodesy, 24(2), pp.115-121.

Wagner, OR (1977) The use of tracers in diagnosing interwell reservoir heterogeneities-Field results. Journal of Petroleum Technology, 29(11), pp.1-410.

Warpinski, N.R. and Teufel, L.W (1987) Influence of geologic discontinuities on hydraulic fracture propagation (includes associated papers 17011 and 17074). Journal of Petroleum Technology, 39(02), pp.209-220.

Warpinski, N.R., Wright, T.B., Uhl, J.E., Engler, B.P., Drozda, P.M., and Pearson, R.E (1996) Micro-seismic monitoring of the B-sand hydraulic fracture experiment at DOE/GRI multi-site projects, SPE 36450.

Warpinski, N.R., Wolhart, S.L. and Wright, C.A (2001) Analysis and prediction of microseismicity induced by hydraulic fracturing. In SPE Annual Technical Conference and Exhibition. Society of Petroleum Engineers.

Watanabe, N., Egawa, M., Sakaguchi, K., Ishibashi, T. and Tsuchiya, N (2017) Hydraulic fracturing and permeability enhancement in granite from subcritical/brittle to supercritical/ductile conditions. Geophysical Research Letters, 44(11), pp.5468-5475.

Watanabe, N., Sakaguchi, K., Goto, R., Miura, T., Yamane, K., Ishibashi, T., Chen, Y., Komai, T. and Tsuchiya, N (2019) Cloud-fracture networks as a means of accessing superhot geothermal energy. Scientific reports, 9(1), p.939.

Willis‐Richards, J., Watanabe, K. and Takahashi, H (1996) Progress toward a stochastic rock mechanics model of engineered geothermal systems. Journal of Geophysical Research: Solid Earth 101(B8): 17481-17496.

Wu, X., Pope, G.A., Shook, G.M. and Srinivasan, S (2002) A method of analyzing tracer data to calculate swept pore volume and thermal breakthrough in fractured geothermal reservoirs under two-phase flow conditions. Proceedings, 30 Workshop on Geothermal Reservoir Engineering, Stanford University, Stanford, CA, USA.

Wu, X (2006) An investigation of partitioning tracers for characterizing geothermal reservoirs and predicting enthalpy production. Doctoral dissertation, The University of Texas at Austin.

Wurmstich B and Morgan FD (1994) Modeling of streaming potential responses caused by oil well pumping. Geophysics, 59(1), pp.46-56.

Xia, Y., Plummer, M., Mattson, E., Podgorney, R., Ghassemi, A (2017) Design, modeling, and evaluation of a doublet heat extraction model in enhanced geothermal systems. Renewable Energy, 105, 232-247.

Xing, P., Yoshioka, K., Adachi, J., El-Fayoumi, A. and Bunger, A.P (2018) Laboratory demonstration of hydraulic fracture height growth across weak discontinuitiesHF height growth with weak interfaces. Geophysics, 83(2), pp.MR93-MR105.

Yasukawa K, Ishido T and Suzuki I (2005) Geothermal reservoir monitoring by continuous self-potential measurements, Mori geothermal field, Japan. Geothermics, 34(5), pp.551-567.

Ye, Z., Janis, M., and Ghassemi, A (2017) Injection-driven Shear Slip and The Coupled Permeability Evolution of Granite Fractures for EGS Stimulation. In 51st US Rock Mechanics / Geomechanics Symposium. San Francisco, California, USA, 25-28 June 2017.

Ye, Z., and Ghassemi, A (2018) Injection-induced shear slip and permeability enhancement in granite fractures. Journal of Geophysical Research: Solid Earth,123, 9009–9032.

Ye, Z., Ghassemi, A (2019). Injection‐Induced Propagation and Coalescence of Preexisting Fractures in Granite Under Triaxial Stress. J. Geoph. Res, Solid Earth, 124, 16 p.

Yeltekin, K. and Akin, S (2005) Analysis of Long Term Tracer Test In Kizildere Geothermal Field Turkey. In Proc., The 31st Workshop on Geothermal Reservoir Engineering, Stanford, California, USA.

Yoshida S (2001) Convection current generated prior to rupture in saturated rocks, Journal of Geophysical Research: Solid Earth, 106(B2), pp.2103-2120.

Yu, X. and Vayssade, B (1991). Joint profiles and their roughness parameters. In International Journal of Rock Mechanics and Mining Sciences & Geomechanics Abstracts, Vol. 28, No. 4, pp. 333-336. Pergamon.

Zang, A., Christian Wagner, F., Stanchits, S., Dresen, G., Andresen, R. and Haidekker, M.A., (1998). Source analysis of acoustic emissions in Aue granite cores under symmetric and asymmetric compressive loads. Geophysical Journal International 135(3): 1113-1130.

Zemel, B. (1995). Tracers in the oil field (Vol. 43). Elsevier.

Zeng, Z. and Roegiers, J.C (2002) Experimental observation of injection rate influence on the hydraulic fracturing behavior of a tight gas sandstone. In SPE/ISRM Rock Mechanics Conference. Society of Petroleum Engineers.

Zhang, Y., Manley, T.S., Li, K. and Horne, R.N., (2015). DNA-Encapsulated Silica Nanoparticle Tracers for Fracture Characterization, Geothermal Resources Council Transactions, 39, (2015), 967-974.

Zhang, Y., Manley, T.S., Li, K. and Horne, R.N., (2016). Uniquely Identifiable DNA-Embedded Silica Nanotracer for Fractured Reservoir Characterization. In Proceedings of the 41st Workshop on Geothermal Reservoir Engineering, Stanford University, Stanford, California.

Zhang, Y., Zeng, Z., Li, K., and Horne, R.N., (2017) DNA Barcoding for fractured reservoir analysis – an initial investigation, Proceedings, 42th Workshop on Geothermal Reservoir Engineering, Stanford University, Stanford, California.

Zhang, H. and S. Han. (1996). Viscosity and density of water+ sodium chloride+ potassium chloride solutions at 298.15 K. Journal of Chemical & Engineering Data, 41(3), pp.516-520.

Zhao, J. and Tso, CP (1993) Heat transfer by water flow in rock fractures and the application to hot dry rock geothermal systems. In Geomechanics Abstracts (Vol. 30, No. 6, pp. 633-641).

Zhao, J. and Brown, E (1992) Hydro-thermo-mechanical properties of joints in the Carnmenellis granite. Quarterly Journal of Engineering Geology and Hydrogeology 25(4): 279-290.

Zhu, H., Deng, J., Jin, X., Hu, L., Luo, B (2015) Hydraulic fracture initiation and propagation from wellbore with oriented perforation. Rock Mechanics and Rock Engineering 48(2): 585-601.

Zhou, C., Wan, Z., Zhang, Y. and Gu, B (2018) Experimental study on hydraulic fracturing of granite under thermal shock. Geothermics, 71, pp.146-155.

Zhou, X.X., Ghassemi, A., and Cheng, A.H.-D (2009) A Three-Dimensional Integral Equation Model for Calculating Poro- and Thermoelastic Stresses Induced by Cold Water Injection into a Geothermal Reservoir. International Journal for Numerical and Analytical Methods in Geomechanics 33 (14): 1613–1640.

Zimmerman, R.W (2012) The history and role of the cubic law for fluid flow in fractured rocks. In AGU Fall Meeting Abstracts.

Zimmermann G, Moeck I, Blöcher G (2010) Cyclic waterfrac stimulation to develop an Enhanced Geothermal System (EGS)—conceptual design and experimental results. Geothermics. 39(1):59–69

Zoback, M.D., Rummel, F., Jung, R. and Raleigh, C.B (1977) Laboratory hydraulic fracturing experiments in intact and pre-fractured rock. In International Journal of Rock Mechanics and Mining Sciences & Geomechanics Abstracts (Vol. 14, No. 2, pp. 49-58).